TOWARD φ_0 PHASE-TUNABLE FERROMAGNETIC JOSEPHSON JUNCTIONS

By

Robert Michael Klaes

A DISSERTATION

Submitted to
Michigan State University
in partial fulfillment of the requirements
for the degree of

Physics—Doctor of Philosophy

2024

ABSTRACT

The interplay between superconductivity and ferromagnetism is a source of rich physics. Spin-triplet supercurrent with long-range propagation through ferromagnetic layers has been well established in theory and experiment and the use of magnetic layers for switching the ground state phase across Josephson junctions between 0 and π has been experimentally demonstrated. Combining the two effects to observe 0-π switching in a Josephson junction containing three noncolinear magnetic layers has also been experimentally demonstrated. Expanding on this idea, with careful control of magnetic layers in a noncoplanar configuration, it has been theoretically proposed that a device can be created which imparts an arbitrary phase difference across the junction. This demonstration of the anomalous Josephson effect, a so-called 'φ_0 junction', however, has yet to be realized in a system of conventional ferromagnets. In this thesis, a battery of notable stepping stones toward this goal are presented in the form of characterization of candidate patterned and unpatterned thin magnetic materials and transport measurements of candidate Josephson junction device structures.

To my father and the lasting legacy of his far too short life.

ACKNOWLEDGEMENTS

I would like to begin by thanking my advisor, Norman Birge. From the moment I started working with him in my undergraduate years, he has been a constant source of guidance, inspiration, support, and intellectual stimulation. He is a seemingly superhuman intellectual powerhouse tempered with self-awareness, humility, and a side of the proverbial 'absent-minded professor' that makes him incredibly approachable and fun to work with. Meeting him was certainly a pivotal moment in my life. I quite simply could not have asked for a better advisor.

I also thank the members of my advisory committee, beginning with Stuart Tessmer. Stuart is the first professor I met in condensed matter physics and helped connect me with Norman in the first place, for which I will be forever grateful. Thank you to Johannes Pollanen, rock-star in the basement and all around great guy, a conversation with him is always fascinating and rewarding. And to Kirsten Tollefson and Remco Zegers, who guided me through my tumultuous first few years of coursework with extraordinary compassion and understanding.

I thank, too, Reza Loloee, facilities coordinator for the physics building and wizard of all laboratory equipment in the basement. I can't count the number of times he fixed something by magic of his proximal aura, not to mention his undying patience and thirst for knowledge. To Baokang Bi, microfabrication expert and clean room manager, whose wisdom and personability were critical to my success. Thank you to Dan Edmunds, electronics genius and encyclopedia of knowledge. I would like to thank our wonderful support staff, in particular the 'Fab Four': Kim Crosslan, Cathy Cords, Jennifer Roberts, and Jessica Dellinger. They have helped me in countless ways– clerically, emotionally, and spiritually. To Vladimir Zelevinsky, Mohammed Maghrebi, Andreas von Manteuffel, Scott Pratt, Luke Roberts, and Steve Hsu for challenging me academically *almost* to the point of breaking. And to the professors I had the great joy of teaching alongside– Chong-Yu Ruan, Saul Beceiro Novo, Joey Huston, Pengpeng Zhang, and Xianglin Ke.

Thank you to the graduate students in the Birge group that proceeded me and helped to mentor me: Joseph Glick and Bethany Niedzielski. And to Victor Aguilar, Alex Madden, and Swapna Sindhu Mishra, who I had the privilege of working with long enough that they also became good

friends. Thanks to visiting researcher Demet Korucu for adding a unique perspective and delightful culinary infusions to the group. Thanks also to our undergraduate students for always adding a dose of levity and for building their own understanding by challenging mine: Anna Osella, Ben Byrd, Thomas Bertus, Jacob Crawford, Jacob Kingsley, Nick Emtage, Fanlin Meng, and Sara Sawford. I would also like to thank all of the extraordinary friends and colleagues I have met at Michigan State: Eric Goodwin, David Greene, Justin Lane, Niyaz Beysengulov, Mark Olson, Eric Macaulay, Danny Paz, Joe Kitzman, Camille Mikolas, Camryn Undershute, Josh Wylie, Mohamed Hassan, Cami Monsalve, Carissa Myers, Kelly Anderson, Heat Uranin, Nick Cariello, Maya Bostock, Alper Korucu, Pranaya Rath, Liz Tuttle, Chris Emery, and Victor Rodriguez-Pereira, just to name a few.

Thanks next to my best friends and stalwart companions. To my guardian angels Hannah Berg and Julia Hinds, who shepherded me through my most challenging times in the program with their unrelenting kindness, compassion, wisdom, humor, and infectious propensity to have fun. Thank you to Michael and Albertina Gottschalk for being extraordinarily good friends and pandemic survival champions. Our time together was among the most cherished of my entire time at MSU. Thank you to Prof. Nathan Satchell, former post-doc extraordinaire, true friend, and beacon of an ideal researcher who was largely responsible for the period of peak productivity and fun in Norman's group. And to Josh 'Jeffrey' Willard, my true best friend and longtime Birge group lab mate. Without you I don't know under which bridge or cemetery I would be aslumber, but I know it's worlds away from where I am now. Your example of a fine human being, scientist, husband, father, and friend is something that will guide me for the rest of my days.

Thank you to the surrogate families of my youth in Seattle: Paul and Dene Napolitan and Clyde and Betty Lince, for stepping up to the plate at a crucial time and helping to make me who I am. Likewise to my local support from The People's Church of East Lansing, graciously led by Rev. Dr. Shawnthea Monroe, for providing unwavering spiritual guidance and a nurturing community. And to my family to be– Debra Whitaker-Volturo and John Volturo and all the lovely Whitaker's and Swift's– of which I am fortunate to officially become a member next summer. The love, warmth and kindness you have shown has meant the world to me and will continue to drive me.

Thanks to my wonderful mother Chris and her exceptional parents, Bill and Luanne, who managed to give me a solid foundation in the face of unenviable circumstances. To my late father Daniel, whose absence was felt stingingly, but whose presence still shaped me. To my brother Ken, his wife Naomi, and their young daughter Ramona who always elicits a smile. To my brother John, his partner Greta, and their incredible daughters Julianne and Emily for their unrestrained passion. To my uncle David, his wife Sheree, and their remarkable son Grayson. And to all of my amazing aunts, uncles, and cousins that make the Klaes side so vibrant, and the late Frank and Patricia, from whom they sprung.

Finally, thank you to my lovely new family unit: my buddy Basilton, you have warmed my heart ever since you came into my life with your indelible curiosity and playfulness. I am so grateful to you for taking care of your mom before I had the privilege of meeting you both. And most especially to my phenomenal fiancée Jena Layne Whitaker (soon to be Klaes). You have made my life so much more meaningful and have opened up a new dimension of happiness that I never thought possible. You keep me grounded; you inspire me; you motivate me; you make me a better man every day. I am so blessed to share my journey with you! I *fully* love you!

TABLE OF CONTENTS

LIST OF TABLES

LIST OF FIGURES

LIST OF ABBREVIATIONS

AF	antiferromagnetic
ALD	atomic layer deposition
CISS	chiral-induced spin selectivity
EBL	electron beam lithography
FTM	film thickness monitor
HUJI	Hebrew University of Jerusalem
IARPA	Intelligence Advanced Research Projects Activity
IEEE	Institute of Electrical and Electronics Engineers
IPA	isopropyl alcohol
I-V	current-voltage
JJ	Josephson junction
JMRAM	Josephson magnetic random-access memory
LOR	lift-off resist
MRAM	magnetoresistive random-access memory
PMA	perpendicular magnetic anisotropy
RCSJ	resistively capacitively shunted junction
RPM	revolutions per minute
SAF	synthetic antiferromagnet
SEM	scanning electron microscope
SQUID	Superconducting QUantum Interference Device
TMAH	tetramethyl ammonium hydroxide
VSM	vibrating-sample magnetometer

CHAPTER 1

INTRODUCTION

Je n'ai fait celle-ci plus longue que parce que je n'ai pas eu le loisir de la faire plus courte.

Blaise Pascal

This thesis focuses on superconductivity and ferromagnetism, and the interplay between these two effects. The early work described has a direct practical application in the form of a proposed superconducting memory cell. The work evolved in search of funding opportunities, resulting in many tangential projects (some of which are outlined in the appendices), and culminates in a project for which there is not an immediately obvious application, but is arguably more interesting from a pure science perspective, the φ_0 junction.

1.1 S/F Background

At the interface of a superconductor and a normal metal, there is some length scale over which the Cooper pairs will 'seep' into the normal metal layer and exhibit some superconducting properties. This *normal metal coherence length* describes the exponential decay of the pair correlation function and is on the order of hundreds of nanometers at cryogenic temperatures. In the 1980's, early theory work predicted how this effect would translate to a superconductor/ferromagnet interface [1]. In short, because of the exchange splitting of the spin bands within the ferromagnet, the electrons comprising the spin-singlet Cooper pairs enter different spins bands within the ferromagnet and acquire a net center-of-mass momentum. This imparts a rapid oscillation and decay of the pair correlation function.

Because this decay occurs over such a short length scale in a ferromagnet (on the order of nanometers), it took quite some time to experimentally observe. In 2001, two groups were able to detect the signature of this oscillation through density of states vs. thickness measurement (Kontos

et al. [2]) and critical current vs. temperature (Ryazanov *et al.* [3]). Shortly after this, oscillations in critical current vs. thickness were also observed [4].

1.2 JMRAM Application

This oscillatory behavior implies that a Josephson junction containing a ferromagnetic interlayer can impart a 0 or π ground state phase difference across its barrier according to the barrier thickness. An ingenious potential application of this property came with the proposal to create a memory device based on control of this phase difference called Josephson magnetic random-access memory (JMRAM) [5]. The design included a two magnetic layer system, one fixed in its magnetization direction, and the other switchable. According to the relative orientations of the magnetizations, this could impart either a 0 or π phase difference, which would form the basis of a binary memory cell. This phase control was demonstrated in 2016 in the Birge group [6], and its operation within a memory array was demonstrated shortly thereafter by Northrop Grumman Corporation [7]. This collaboration toward optimization of this memory device funded the work in this group for many years, resulted in many advancements and publications [8, 9, 10, 11, 12], and forms the basis of the early work in this thesis.

1.3 Spin-Triplet Pair Correlations

An interesting and totally unexpected idea was posited by theorists in the early 2000's whereby magnetic inhomogeneities could impart long-range spin-triplet pair correlations within a ferromagnetic material [13, 14]. If spin-singlet Cooper pairs could be transformed into spin-triplet pairs with like-paired spins, the decay of the pair correlation function within a ferromagnet would be much slower than in the spin-singlet case. In 2010, the first convincing experimental evidence of these long-range spin-triplet pair correlations was observed in a system of strong ferromagnets by the Birge group [15]. The experiment used a geometry proposed by Houzet and Buzdin [16] which includes a system of three ferromagnetic layers with the magnetizations of the outer 'spin-mixing' layers oriented perpendicular to that of the central propagation layer [17]. Subsequently, additional work in the group fleshed out the effect [18, 19, 20]. An alternate method of generating long-range spin-triplet supercurrent using interfacial materials with a large spin-orbit coupling effect

was investigated later in this group [21, 22], and forms the basis of the work outlined in Appendix A.3.

1.4 φ_0 Phase-tunable Josephson Junctions

As the JMRAM project drew to a close, some of the later experiments investigating the use of long-range spin-triplet generating systems [8, 10] led the group to explore similar materials for use in the realization of a so-called 'φ_0-junction'. As discussed in greater detail in Section 2.3.9, this φ_0-junction had been predicted for some time [23, 24] and demonstrated only in some exotic materials, but not using traditional ferromagnets. By design, the device allows for an arbitrary, tunable phase, rather than the binary 0 or π phase drop across its Josephson junction. This provided the motivation for the work in the thesis of Victor Aguilar [25], and the work highlighted in Chapter 5. In many ways, the realization of such a device would be the culmination of over a decade of work in the Birge group.

1.5 Chapters Overview

Chapter 2 will explore the fundamental science behind the research in this thesis. We will begin with ferromagnetism, then move on to superconductivity, then explore the interplay between those phenomena.

Chapter 3 covers the basics of sample fabrication in the Birge group, from wafer dicing to methods of lithography to sputtering deposition and finally, sample measurement.

Chapter 4 describes work on the Intelligence Advanced Research Projects Activity (IARPA) C3 project in collaboration with Northrop Grumman Corporation toward optimization of a JMRAM device [5, 6, 7]. In particular, it explores the use of an antiferromagentic layer used to pin the fixed layer in the proposed device. This work is published in Institute of Electrical and Electronics Engineers (IEEE) Transactions on Applied Superconductivity [26].

Chapter 5 explores progress toward the φ_0 junction – a proposed device with a tunable phase rather than the binary 0 or π phase seen in traditional superconductor/ferromagnet systems. This includes evidence for the optimization of spin-triplet supercurrent generation from the addition of a Nb/Au base layer, patterned and unpatterned candidate thin film characterization, and Josephson

junctions containing a full proposed stack.

Chapter 6 includes a brief summary of the work contained in this dissertation and a bit of perspective.

Appendix A includes data collected on $Ni_{73}Fe_{18}Cr_9$ films as part of a project exploring that material's viability for use in JMRAM, a study optimizing fabrication methods, specifically investigating whether a thin layer of Nb on the top of the bottom lead is necessary, and a summary of work on a collaboration with a research group at Hebrew University in Jerusalem exploring the use of chiral molecules as a generator of spin-triplet supercurrent.

Appendix B provides select laboratory notes including a calculation of the supercurrent through a spin-triplet Josephson junction performed by Prof. Birge, a template for proper documentation of a sputtering run in the logbook for maximum clarity and information density and contains a procedure for dicing patterned magnetic array samples for measurement in the magnetometer.

CHAPTER 2

THEORETICAL BACKGROUND

...en matière scientifique, on a souvent des prédécesseurs beaucoup plus anciens qu'on ne le pense a priori.

Louis Eugène Félix Néel

This chapter will focus on the phenomenological underpinnings of the experimental research in this thesis. We will begin with ferromagnetism, then move on to superconductivity, the proximity effect, ferromagnetic Josephson junctions, Superconducting QUantum Interference Devices (SQUIDs), and finally spin-triplet superconductivity and the φ_0 junction. It is not intended to be comprehensive by any means, but is meant to briefly discuss some of the history and relevant physics needed to understand the projects discussed herein.

2.1 Ferromagnetism

Ferromagnetism was first discovered in lodestone in the 6th century BC [27]. Since then, it has been an endless source of fascination among researchers and the general public alike. While a basic understanding of the atomic origin of the phenomenon has been understood for some time, its nuances continue to be a fertile ground for research. In the atomic case, one can think of the absence or presence of unpaired spins dividing materials into either diamagnetic (where the orbital magnetic moments weakly oppose an applied field) or paramagnetic (where the spin magnetic moments weakly align with an applied field). In atoms with multiple valence electrons in an unfilled orbital, the exchange interaction leads to Hund's second rule [28], which states that the lowest energy state has the spins maximally aligned. The exchange interaction arises from the need of the overall wavefunction of identical fermions to be antisymmetric under exchange. This causes an antisymmetric spatial wavefunction to pair with symmetric spin states and vice versa. With

electrons in an antisymmetric spatial state, they are on average farther apart and therefore yield a lower Coulomb repulsion energy.

When atoms are put together in insulating solids, similar arguments as above explain the appearance of diamagnetism or paramagnetism. Metallic solids all exhibit Pauli paramagnetism, which may or may not exceed the intrinsic atomic diamagnetism in strength. Far more interesting is the case when there are strong exchange interactions between the electron magnetic moments on *neighboring* atoms, which may give rise to ferromagnetism. The complete theory of ferromagnetism is complicated and relies on a detailed understanding of the band structure. Stoner introduced a simplified model where a threshold referred to as the Stoner criterion [29] determines which materials exhibit this property. For a more complete picture, one should consult a magnetism reference material such as [30, 31]. Typical ferromagnetic materials include cobalt, iron, nickel, or their alloys. Some other types of magnetism include: antiferromagnetism (where the spins will compensate each other) and ferrimagnetism, which is akin to a special case of antiferromagnetism where the moments of the unpaired spins are compensated in their direction, but not in their magnitude, so there is an overall moment.

2.1.1 Domains

While the local effect of the exchange interaction between neighboring atoms in a ferromagnet will result in its spins aligning in a uniform direction, macroscopically, minimizing the magnetostatic energy dictates that regions of spins form whose overall moments will cancel each other. This formation of domains is the reason that magnetic materials in nature are often found in a demagnetized state.

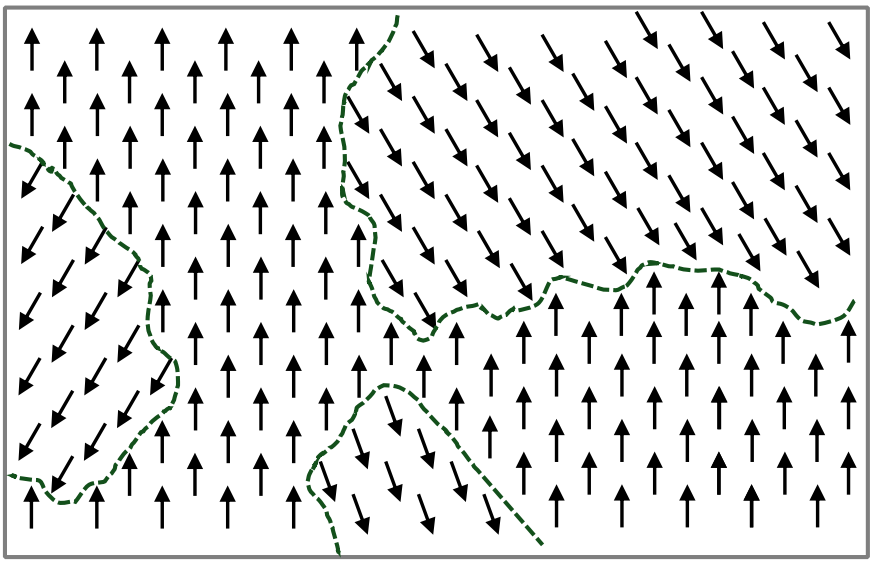

Figure 2.1 **Ferromagnetic domains.** A representation of ferromagnetic domains where there are sub-regions of uniform spin within a macroscopic shape.

Figure 2.1 shows a representation of this. It is only after application of a sufficient magnetic field that the spins will align together on a macroscopic scale. Depending upon the material, this effect will even impact devices on the sub-micron scale of those studied in this thesis. In particular, Ni magnetic layers in our Josephson junctions will often break into domains and not switch uniformly, wreaking havoc on the neat and tidy electron transport picture described later in this chapter.

2.1.2 Anisotropy

Magnetic anisotropy in general refers to the preference of a magnetic system to align in a particular direction. Magnetocrystalline anisotropy is a special case of this effect where this anisotropy is induced by the atomic structure of the crystal lattice due to the spin-orbit interaction. By clever design, a preferred switching axis can be imparted to a magnetic system. In particular in our research, while $Ni_{81}Fe_{19}$ (permalloy) is chosen for its low intrinsic magnetocrystalline anisotropy, we can engineer this directional preference into the material by application of a magnetic field during its growth. In a small enough system, the macroscopic shape of a magnetic structure can also impart a preferred axis. For example, in an elliptical shape, the spins will preferentially align along the long axis. Another useful anisotropy is perpendicular magnetic anisotropy (PMA), where the spins of certain multilayers such as $[Ni(0.4)/Co(0.2)]_n$ will prefer to point perpendicular

to the plane of the interfaces of the materials, as explored in Chapter 5.

Figure 2.2 shows the ideal case of a single domain magnetic system with uniaxial anisotropy, where its response to a magnetic field H along one axis (the easy axis) behaves perfectly ferromagnetically, i.e. it exhibits sharp switching at a coercive field H_C, and 100% remnance of the saturation magnetization M_{sat} at zero field. Along the other axis (the hard axis), the behavior appears similar to an antiferromagnet, i.e. the spins will be slowly pulled out of alignment with the easy axis up to their M_{sat}, and there is zero remnance of the magnetization at zero field.

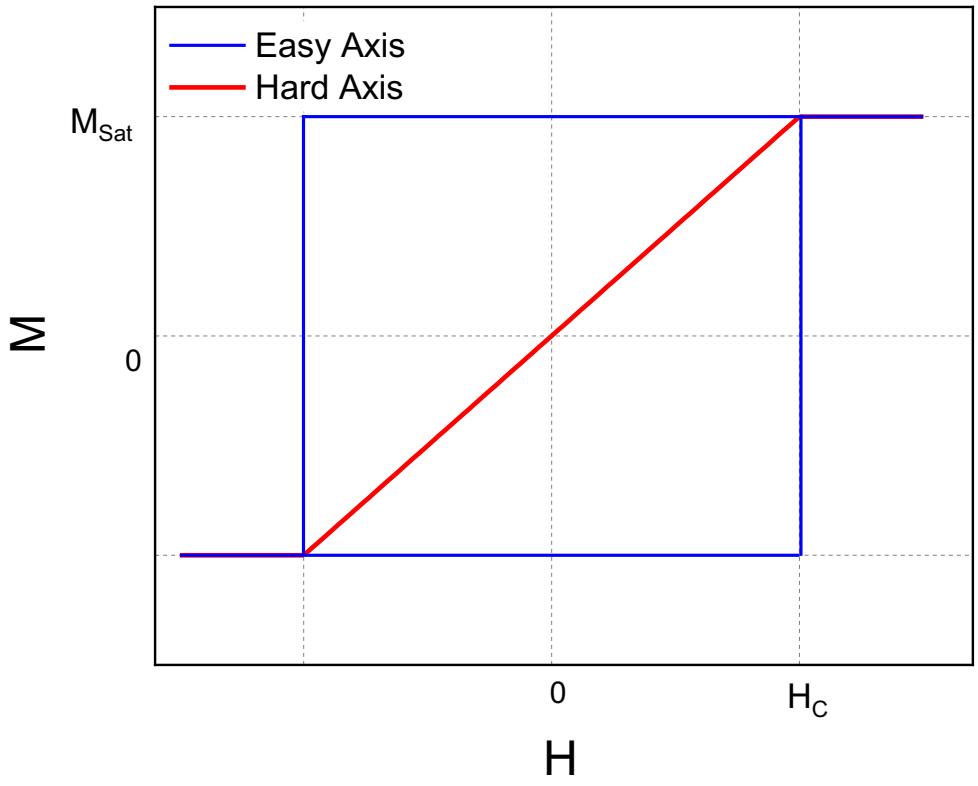

Figure 2.2 **Anisotropy.** A representation of idealized easy and hard axis magnetization, M, vs. applied field, H, measurements. The easy axis exhibits idealized ferromagnetic behavior, switching its magnetization abruptly and completely at its coercive field, H_C.

Figure 2.3 shows how these anisotropies can be 'stacked' together to create an even stronger preferred switching axis. In the case of this graphic, the growth field and the shape of the ellipse both impart a preferred axis along the long axis of the ellipse. This encourages uniform switching.

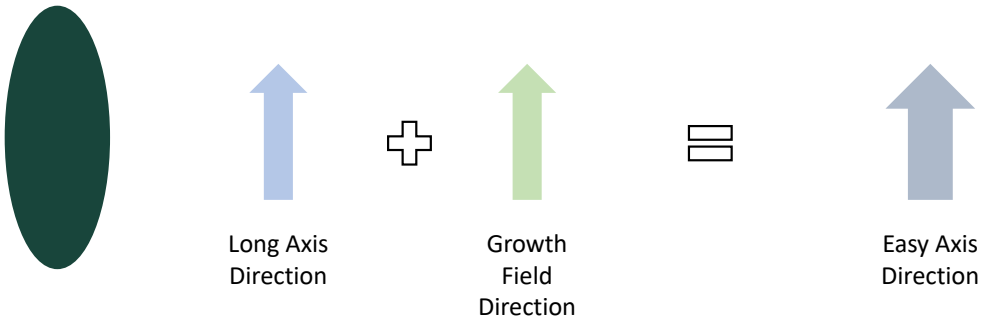

Figure 2.3 **Addition of anisotropies.** A graphic showing how anisotropies can be aligned to create a dominant switching axis.

2.2 Superconductivity

Superconductivity is a phenomenon that is found at low temperatures in many materials and was first discovered by Heike Kamerlingh Onnes in 1911 [32]. On the shoulders of pioneering work by Meissner [33], the Londons [34], Ginzburg–Landau [35], and others, a microscopic theory of superconductivity was posited by John Bardeen, Leon Cooper, and John Robert Schrieffer in 1957 [36, 37], which is now referred to as 'BCS theory'. A full treatment of these theories could not possibly be conquered in this humble thesis, but we will explore some key implications in the following sections.

2.2.1 Meissner Effect

German physicists Walther Meissner and Robert Ochsenfeld performed an experiment in 1933 [33] by cooling tin and lead samples through their transition temperature in a magnetic field and observed that the samples expelled all magnetic fields from the bulk of the materials. This expulsion of magnetic field is referred to as *the Meissner effect* and was the first evidence that distinguished superconductors from idealized perfect conductors. This effect is the basis of some of the flashiest demonstrations of superconductivity such as passive magnetic levitation.

2.2.2 London Equations

In 1935, brothers Fritz and Heinz London devised a theory that was able to explain the Meissner effect [34]. The London equations relate superconducting current density, J, to the electric (E) and

magnetic (B) fields within a superconductor, and can be expressed as follows:

$$\frac{\partial J}{\partial t} = \frac{n_s e^2}{m} E \tag{2.1}$$

and

$$\Delta \times J = -\frac{n_s e^2}{m} B \tag{2.2}$$

where e is the electron charge, m is the electron mass, and n_s is the number density of superconducting electrons. If the Maxwell relation $\Delta \times B = \mu_0 J$ is applied to Eq. 2.2, the result can be manipulated into the form:

$$\Delta^2 B = \frac{1}{\lambda_L^2} B \tag{2.3}$$

which results in the definition of the phenomenological parameter:

$$\lambda_L \equiv \sqrt{\frac{m}{\mu_0 n_s e^2}} \tag{2.4}$$

the *London penetration depth*, which represents the characteristic length scale over which external magnetic fields are suppressed exponentially within the superconductor.

2.2.3 Ginzburg–Landau theory

In 1950, Vitaly Ginzburg and Lev Landau posited a theory [35] to describe superconductivity from a phenomenological perspective without a microscopic treatment. Their most salient inclusion was the introduction of the complex psuedo-wavefunction ψ which folded a quantum mechanical understanding into superconducting theory. By treating the transition from resistive state to superconducting state as a second-order phase transition, and minimizing the total free energy, they derived the first Ginzburg–Landau equation:

$$\alpha\psi + \beta|\psi|^2\psi + \frac{1}{2m^*}\left(-i\hbar\Delta - \frac{e^*}{c}A\right)^2 \psi = 0 \tag{2.5}$$

which is analogous to the time-independent Schrödinger equation. From this, they also derived an equation for the current density, J_s:

$$J_s = \frac{i\hbar}{2m^*}\left(\psi^*\Delta\psi - \psi\Delta\psi^*\right) - \frac{e^{*2}}{m^*}|\psi|^2 A \tag{2.6}$$

which comprises the second Ginzburg–Landau equation. The theory also introduces another important characteristic length scale in superconductivity, the *coherence length*:

$$\xi_S = \sqrt{\frac{\hbar^2}{2m^*|\alpha|}} \tag{2.7}$$

which can be thought of as the Cooper pair size and, together with the London penetration depth, λ_L, determine the parameter κ:

$$\kappa = \lambda_L / \xi_S \tag{2.8}$$

whose value determines whether a superconductor is *Type I*, where superconductivity is abruptly destroyed above a critical field H_c, or *Type II*, where an intermediate *vortex state* is created between critical fields H_{c1} and H_{c2}.

2.2.4 BCS Theory

The key insight leading to the groundbreaking work of John Bardeen, Leon Cooper, and John Robert Schrieffer in 1957 [36, 37] was that electrons in a superconductor form so-called *Cooper pairs* that condense into a single coherent quantum state. The resulting theory was the first microscopic understanding of superconductivity. At its core, BCS theory describes the interaction between electrons and quantized lattice vibrations called phonons. Below a certain temperature, T_c, the weakly attractive electron-phonon interaction compensates the repulsive Coloumb interaction of the electrons and an energy gap, Δ, opens up, where 2Δ represents the energy required to break up a Cooper pair into two quasiparticle excitations:

$$\Delta(T = 0) = 1.764 k_B T_c \tag{2.9}$$

where T_c is the critical temperature. The theory describes the aforementioned coherence length in a more useful way:

$$\xi_S^{\text{ballistic}} = \frac{\hbar v_F}{\pi \Delta} \tag{2.10}$$

in the ballistic limit. In the diffusive limit, where the mean free path, ℓ, is smaller than the coherence length, then:

$$\xi_S^{\text{diffusive}} = \sqrt{\frac{\hbar D_S}{\Delta}} \tag{2.11}$$

BCS theory also helped shed light on many mysteries, such as the basis for what determines the London penetration depth λ_L, critical temperature T_c, and critical field H_c for a particular material.

2.3 Josephson Junctions

2.3.1 The Josephson Effect

In 1962, Brian Josephson theorized what would happen when a superconductor was interrupted by a thin insulating layer [38], now referred to as a *Josephson junction (JJ)*. The insights from this theory are at the heart of all of the research contained within this thesis. The theory builds on the work of Ginzburg and Landau and was the first prediction of the tunneling of Cooper pairs through such a barrier. It describes the current flowing across an insulating barrier as:

$$I_s = I_c \sin \phi \tag{2.12}$$

where I_c is the *critical current*, the maximum allowable supercurrent through the junction, and ϕ is the phase difference from one side of the junction to the other. The phase evolution is described by:

$$\frac{d\phi}{dt} = \frac{2eV}{\hbar} = \frac{2\pi V}{\Phi_0} \tag{2.13}$$

with $\Phi_0 = \frac{2\pi\hbar}{2e}$ representing the *magnetic flux quantum*, discussed further in Section 2.3.7. Equations 2.12 and 2.13 are referred to as the *Josephson relations*.

2.3.2 RCSJ Model

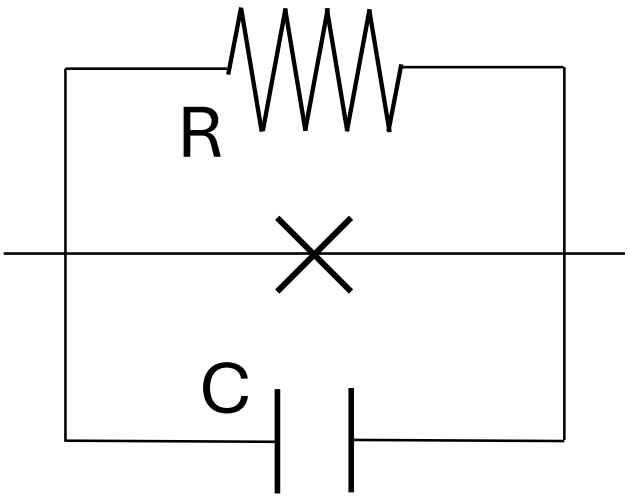

Figure 2.4 **RCSJ Model.** A diagram of the RCSJ model circuit showing the ideal Josephson junction in the middle in parallel with a resistor and a capacitor.

As a way of understanding the behavior of a real Josephson junction, the *resistively capacitively shunted junction (RCSJ)* model was developed. In this treatment, the junction is modeled as an ideal Josephson junction in parallel with a resistor and a capacitor, as shown in Figure 2.4. This accounts for the AC impedance of an actual junction. From this, we get an expression for the current through the circuit:

$$I = I_c \sin\phi + \frac{V}{R} + C\frac{dV}{dt} \tag{2.14}$$

combining this with 2.13 and defining the Josephson energy $E_J = \hbar I_{c0}/2e$, we arrive at:

$$\left(\frac{\hbar}{2e}\right)^2 C\frac{d^2\phi}{dt^2} + \left(\frac{\hbar}{2e}\right)^2 \frac{1}{R}\frac{d\phi}{dt} = E_J\left(\frac{I}{I_{c0}} - \sin\phi\right) \tag{2.15}$$

which gives us a second-order differential equation for the time dependence of the phase. This has a classical analog to a particle of mass $\left(\frac{\hbar}{2e}\right)^2 C$ moving in a potential:

$$U = -E_J\left(\frac{I}{I_{c0}}\phi - \cos\phi\right) \tag{2.16}$$

with a linear drag force $\left(\frac{\hbar}{2e}\right)^2 \frac{1}{R}\frac{d\phi}{dt}$. This implies a Stewart-McCumber damping parameter [39, 40]:

$$\beta_c = \frac{(I_{c0}R)^2 C}{E_J} \tag{2.17}$$

When β_c is small, this is the case of the *overdamped junction*, which simplifies equation 2.15 to a first-order differential equation of the form:

$$\frac{d\phi}{dt} = \frac{I_{c0}^2 R}{E_J}\left(\frac{I}{I_{c0}} - \sin\phi\right) \tag{2.18}$$

In this overdamped case, the time-averaged voltage becomes

$$|V| = R\sqrt{I^2 - I_{c0}^2}. \tag{2.19}$$

All of the Josephson junctions studied in this thesis were in the overdamped limit as shown in Figure 2.5, so Equation 2.19 was used to fit their current-voltage (I-V) curves.

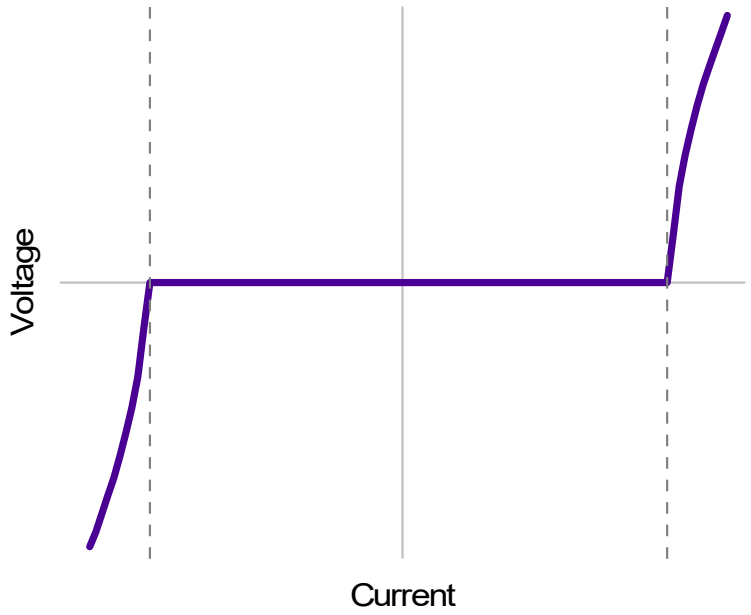

Figure 2.5 **Overdamped I-V Curve.** Voltage vs. current (I-V) plot of an overdamped Josephson junction, with the dashed line indicating the critical current, I_c.

2.3.3 Magnetic Field Effects in Josephson Junctions

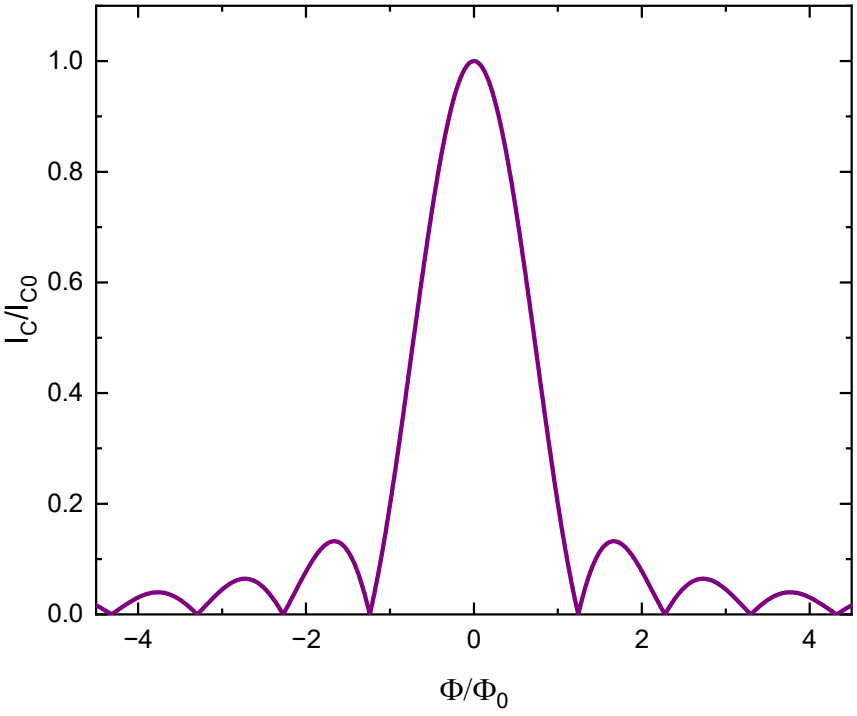

Figure 2.6 **Airy interference pattern.** A representation of the magnetic field response of the critical current of a circular Josephson junction.

An informative method of probing a Josephson junction is by application of an in-plane magnetic field. The junctions discussed in this thesis are in the so-called small junction limit, such that the *Josephson penetration depth*:

$$\lambda_J = \sqrt{\frac{\Phi_0}{2\pi d \mu_0 J_c}} \gg w \tag{2.20}$$

where w is the width of the junction. In this regime, the critical current density can be treated as uniform. Because of the gradient of the vector potential, the magnetic response function takes a form analogous to that of optical interference, resulting in a Fraunhofer interference pattern for rectangular junctions [41]. In circular junctions, or elliptical junctions with the field applied along the symmetry axis, the form is that of an Airy function, as shown in Figure 2.6, and described by:

$$I_c = 2I_{c0}\left|\frac{J_1\left(\frac{\pi\Phi}{\Phi_0}\right)}{\frac{\pi\Phi}{\Phi_0}}\right| \tag{2.21}$$

with $\Phi = B_y 2R(\lambda_L + \lambda_R + t)$ assuming $\lambda_L, \lambda_R \gg t$ where λ_L and λ_R are the London penetration depths of the materials on each side of the barrier, t is the barrier thickness, and J_1 is a Bessel function of the first kind. (This also assumes that the superconducting electrodes are much thicker than their λ's.)

Together, these Airy patterns and Fraunhofer patterns are often colloquially referred to as Fraunhofer patterns. In a junction of known geometry, a fit using Equation 2.21 can give us an estimate of λ_L. In very small junctions, where junction geometry may vary due to process variations, we can use known values of λ_L and λ_R to determine the junction width. Also, in such cases where the central peak is shifted from zero field due to magnetization, an extrapolation of the peak critical current and magnitude of the shift can also be made. Such analysis was performed on the data in Chapter 5 and Appendix A.

2.3.4 S/N Proximity Effect

The Josephson junctions envisioned by Brian Josephson consisted of a very thin tunnel barrier between the superconducting (S) electrodes. But one can imagine replacing the insulating barrier with a normal (i.e. non-superconducting) metal (N) in which case this 'barrier' can be much thicker. Later, we'll see that the barrier can even be a ferromagnetic metal, but with only an intermediate

thickness. To begin to understand these situations, we must look at how electrons pass through an S/N interface.

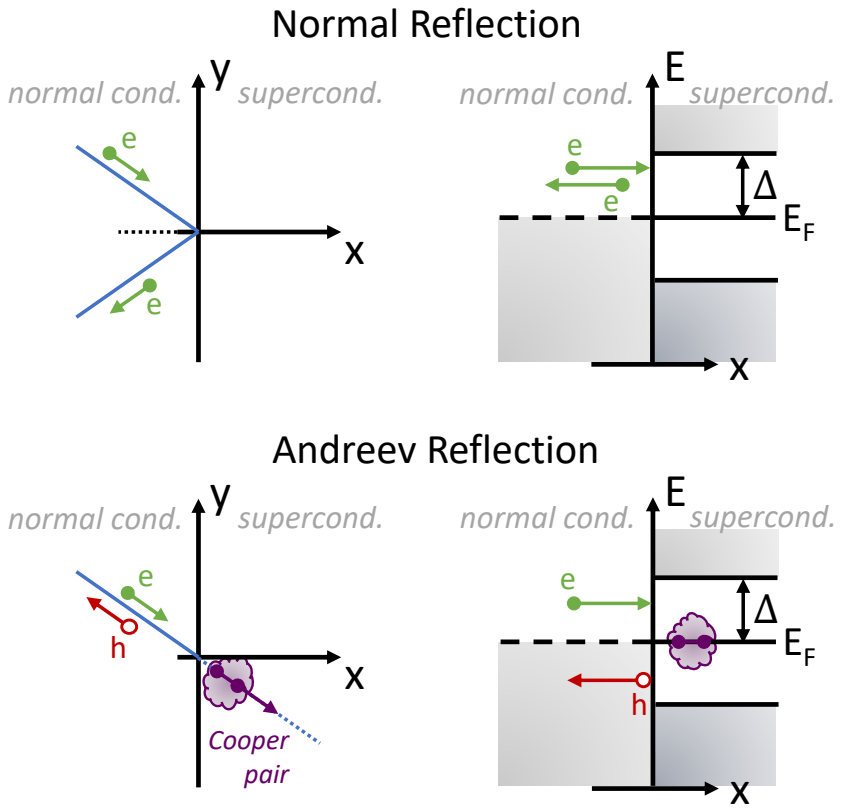

Figure 2.7 **Andreev reflection.** A depiction of Andreev reflection showing Cooper pair generation at the N/S interface, adapted from [42].

Andreev reflection [43] describes the scattering of electrons at the interface of a superconductor and a normal metal. An incident electron from the normal metal may form a Cooper pair in the superconductor while a hole is retroreflected back into the normal metal with opposite spin and velocity, but equal momentum. Figure 2.7 shows a depiction of Andreev reflection compared to normal reflection of an electron at the N/S interface. The inverse effect of a Cooper pair incident on an S/N interface from the S side is also described in a symmetrical way. This process gives rise to electron pair correlations in the normal metal near the S/N interface. Crucially, the phase coherence of the electrons is preserved in this process. The length scale over which these correlations persist is called the *normal metal coherence length,* ξ_N and can again be calculated in either the ballistic

'clean' limit (where the mean free path is larger than the coherence length) or the diffusive 'dirty' limit (where the mean free path is smaller than the coherence length). In the ballistic limit, the normal metal coherence length is described by:

$$\xi_N^{\text{ballistic}} = \frac{\hbar v_F}{2\pi k_B T} \tag{2.22}$$

where v_F is the Fermi velocity. In the diffusive limit, we have

$$\xi_N^{\text{diffusive}} = \sqrt{\frac{\hbar D_N}{2\pi k_B T}} \tag{2.23}$$

where D_N is the electron diffusion constant, k_B is the Boltzmann constant, and T is the temperature. The value of ξ_N is typically on the order of tens to hundreds of nm at cryogenic temperatures.

2.3.5 S/F Proximity Effect

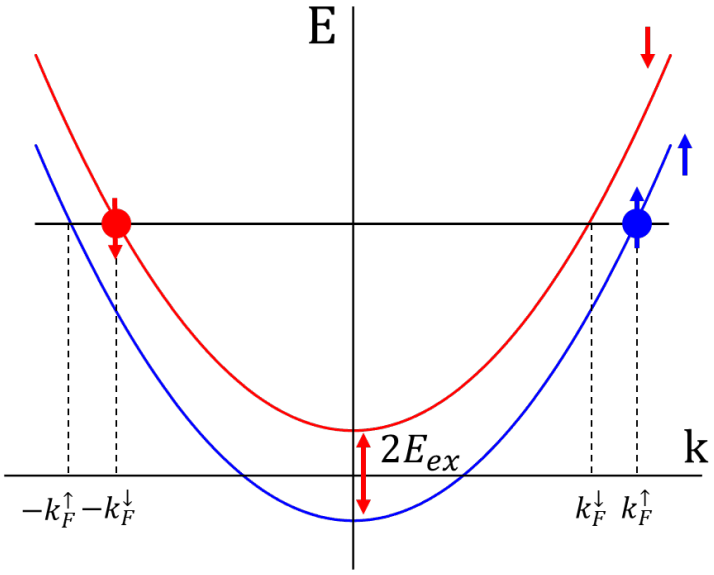

Figure 2.8 **Spin bands.** A toy model of spin bands within a ferromagnetic material, with the down spin electron (in red) and the up spin electron (in blue) shown entering the different bands.

In proximity with a ferromagnet, the situation becomes more interesting. Whereas the spin bands are degenerate within a normal metal, the spin bands in a ferromagnetic material are split by twice the exchange energy, E_{ex}. As depicted in Figure 2.8, when the two electrons from a spin-singlet Cooper pair enter the ferromagnet, they must enter opposite spin bands, which results in the

pair acquiring a net center of mass momentum $\hbar Q = \left(k_F^{\uparrow} - k_F^{\downarrow}\right) = \frac{2E_{ex}}{v_F}$, assuming parabolic bands. This, in turn, transforms the singlet wavefunction from the superconductor $\Psi_S = \frac{1}{\sqrt{2}}\left(|\uparrow\downarrow\rangle - |\downarrow\uparrow\rangle\right)$ into

$$\Psi_F = \frac{1}{\sqrt{2}}\left(|\uparrow\downarrow\rangle e^{iQx} - |\downarrow\uparrow\rangle e^{-iQx}\right) \tag{2.24}$$

which can be rewritten as

$$\Psi_F = \frac{1}{\sqrt{2}}\left[\left(|\uparrow\downarrow\rangle - |\downarrow\uparrow\rangle\right)\cos Qx + i\left(|\uparrow\downarrow\rangle + |\downarrow\uparrow\rangle\right)\sin Qx\right] \tag{2.25}$$

where x is the center of mass coordinate of the pair measured from the S/F interface. This imparts a spatial oscillation of the pair correlation function, which contains both a spin-singlet state (cosine term) and the $m = 0$ spin-triplet state (sine term).

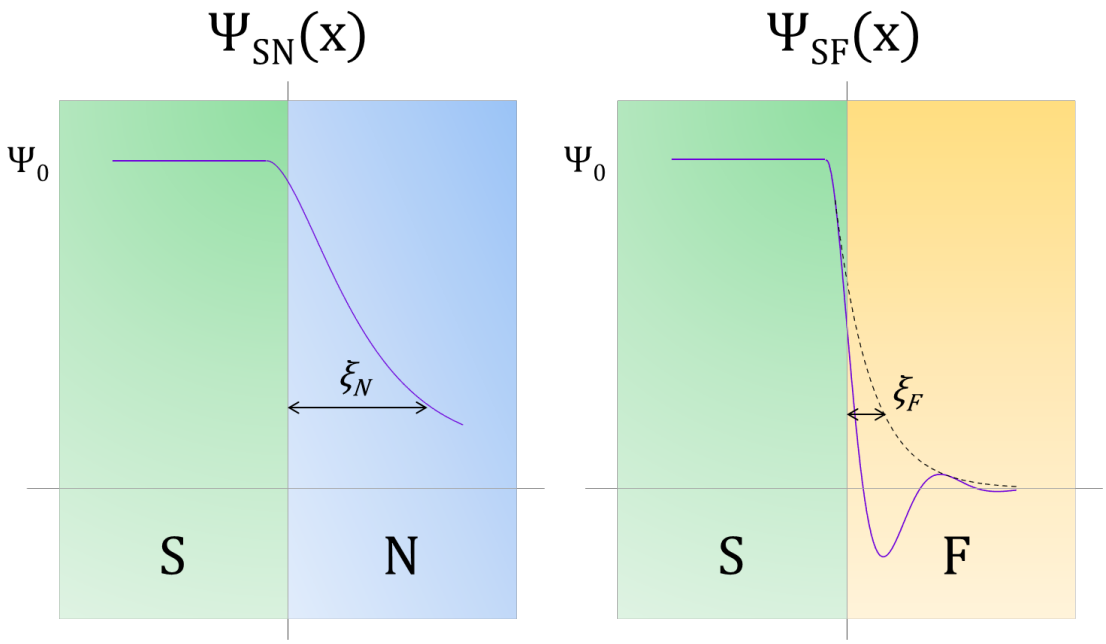

Figure 2.9 **Pair correlation graphic.** A depiction of the pair correlation functions at S/N (left) and S/F (right) interfaces indicating the steeper decay and oscillation within the ferromagnetic layer. Note that $\xi_N \gg \xi_F$.

The characteristic length scale governing the oscillations of the pair correlations is sometimes called the *ferromagnetic coherence length* or the 'exchange length', and is given by

$$\xi_F^{\text{ballistic}} = Q^{-1} = \frac{\hbar v_F}{2E_{ex}} \tag{2.26}$$

In the ballistic limit, pair correlations decay algebraically due to angular averaging. In the diffusive limit, in contrast, pair correlations decay exponentially, with both the oscillations and decay characterized by

$$\xi_F^{\text{diffusive}} = \sqrt{\frac{\hbar D_F}{E_{ex}}} \tag{2.27}$$

where D_F is the diffusion constant in the ferromagnet. Figure 2.9 compares the pair correlation function at the S/N interface to that at the S/F interface, where there is the oscillation and a much steeper decay.

2.3.6 π Josephson Junctions

The oscillations in the S/F case of Figure 2.9 where the correlation function dips below zero represent a situation where, if the width of a Josephson barrier is chosen to be in this region, the energy is minimized when the phase drop across the junction is π rather than 0. These are referred to as π *junctions*, and were first theorized by Bulaevskii et al. [44] in 1978, and observed experimentally by Ryazanov et al. [3] and Kontos et al. [2] in 2001. A large amount of materials work has been done exploring π junctions in this group and others since then [45].

2.3.7 SQUIDs

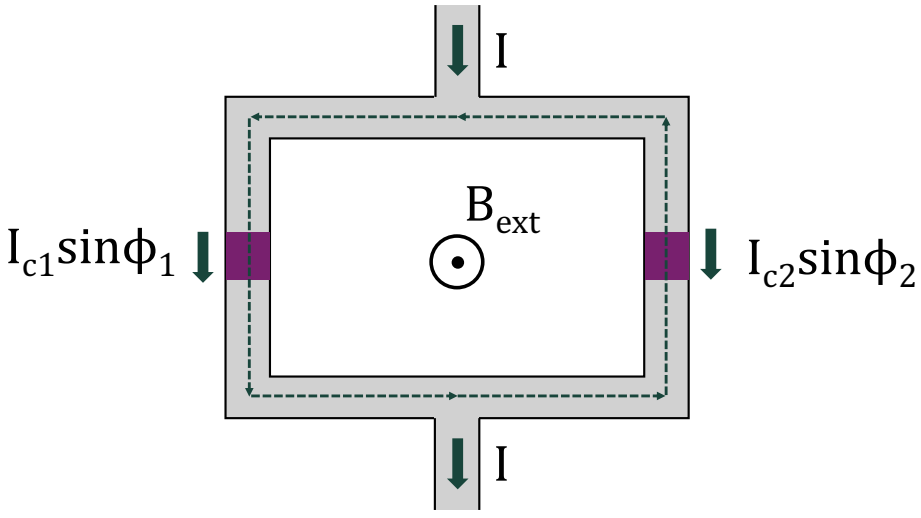

Figure 2.10 **SQUID.** Diagram of a SQUID containing two Josephson junctions. Adapted from [46].

First demonstrated in 1964, [47] *Superconducting QUantum Interference Devices (SQUIDs)* comprise one or more Josephson junctions in a superconducting loop. A solid loop (without such junctions), is subject to *flux quantization*, experimentally discovered in 1961 [48, 49]. This is a result of the need for the superconducting wavefunction to be single-valued around a loop, and it implies that the magnetic flux threading through a loop is quantized in multiples of the magnetic flux quantum, $\Phi_0 = \frac{h}{2e} \approx 2.068$ x 10^{-15} Wb:

$$\Phi = \iint B \cdot d\sigma = n\Phi_0 \tag{2.28}$$

A representation of a DC SQUID is shown in Figure 2.10 comprised of two Josephson junctions in a superconducting loop. The current is clearly:

$$I = I_{c1} \sin \phi_1 + I_{c2} \sin \phi_2 \tag{2.29}$$

If an external flux Φ_{ext} is applied to the loop (and the self-inductance of the loop is negligibly small), the need for single-valuedness of the wavefunction (think of traveling around the SQUID in Fig. 2.10 clockwise from the top) implies:

$$\phi_2 - \phi_1 - 2\pi \frac{\Phi_{ext}}{\Phi_0} + = 2\pi n \tag{2.30}$$

where n is an integer. Plugging Eq. 2.30 into Eq. 2.29 gives:

$$I(\Phi_{ext}, \phi_1) = I_{c1} \sin \phi_1 + I_{c2} \sin \left(\phi_1 - 2\pi \frac{\Phi_{ext}}{\Phi_0} \right) \tag{2.31}$$

If we consider a simple case of a symmetric SQUID and $I_{c1} = I_{c2}$, we can find an expression for I_c by maximizing Equation 2.31 with respect to ϕ_1 and get:

$$I_c(\Phi_{ext}) = 2I_{c1} \left| \cos \left(\pi \frac{\Phi_{ext}}{\Phi_0} \right) \right| \tag{2.32}$$

from which we see that the critical current of the SQUID oscillates periodically as a function of the flux. Figure 2.11 shows this relation. Note that in the case where $I_{c1} \neq I_{c2}$, this plot would be vertically offset by the difference in critical current.

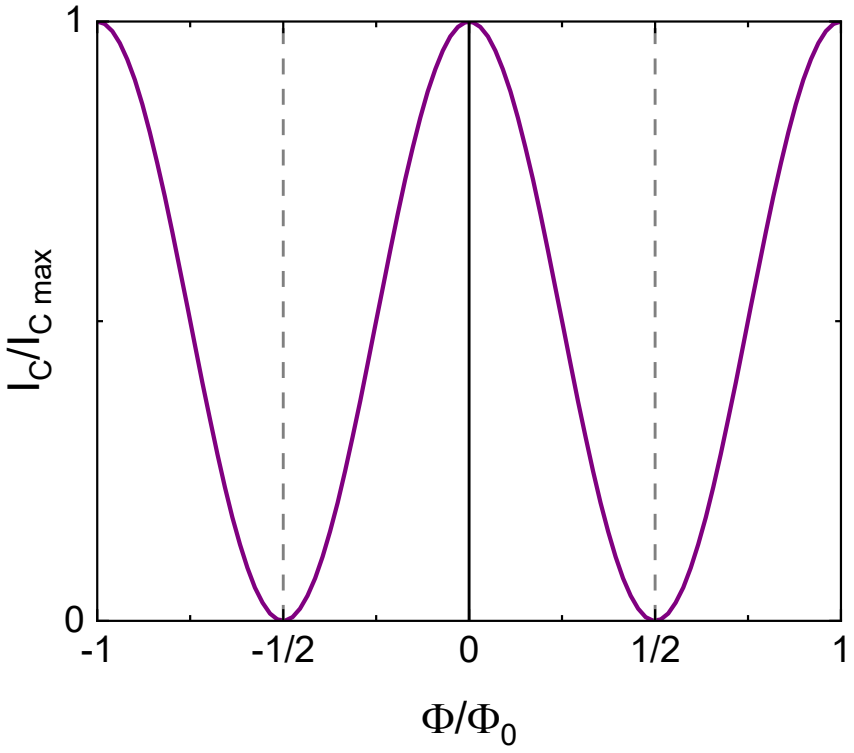

Figure 2.11 **SQUID I_C vs. flux.** Plot of critical current versus flux for a symmetric SQUID with negligible self-inductance, showing sinusoidal oscillation.

2.3.8 Spin-Triplet Superconductivity

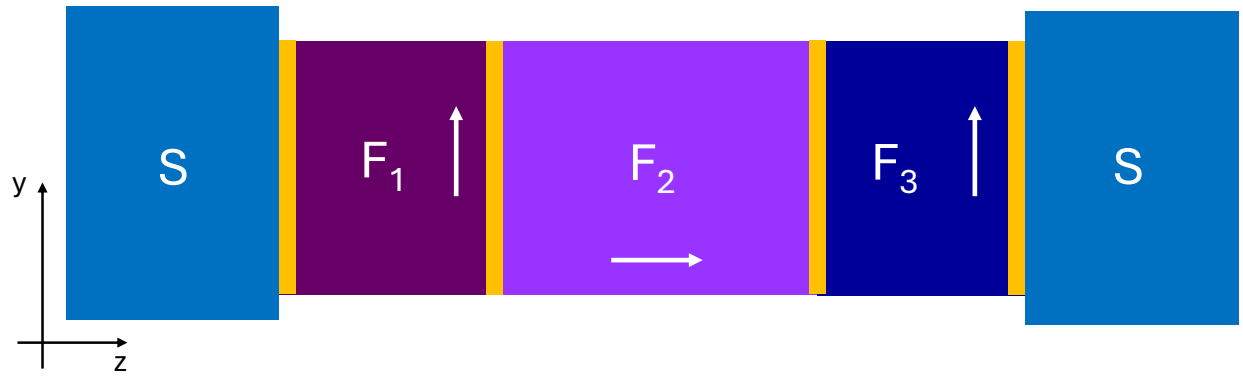

Figure 2.12 **Triplet JJ design.** Diagram of a trilayer spin-triplet Josephson junction with the outer (F_1, F_3) spin-mixing layers having magnetizations perpendicular to the central propagation layer (F_2).

Beginning with the wavefunction of the supercurrent in a ferromagnetic Josephson junction described earlier,

$$\Psi_F = \frac{1}{\sqrt{2}} \left[(|\uparrow\downarrow\rangle - |\downarrow\uparrow\rangle) \cos Qx - i\,(|\uparrow\downarrow\rangle + |\downarrow\uparrow\rangle) \sin Qx \right], \tag{2.33}$$

proper engineering can induce *long-range spin-triplet* superconducting pair correlations. As predicted by Bergeret et al. in 2001 [50], if a ferromagnetic propagation layer with a magnetization (which sets the quantization axis) perpendicular to that of the first layer is introduced, as shown if Figure 2.12, the short-range spin-triplet component is converted into long-range spin-triplet as demonstrated in the basis transformation:

$$\frac{1}{\sqrt{2}} (|\uparrow\downarrow\rangle + |\downarrow\uparrow\rangle)_y = \frac{i}{\sqrt{2}} (|\uparrow\uparrow\rangle + |\downarrow\downarrow\rangle)_z \tag{2.34}$$

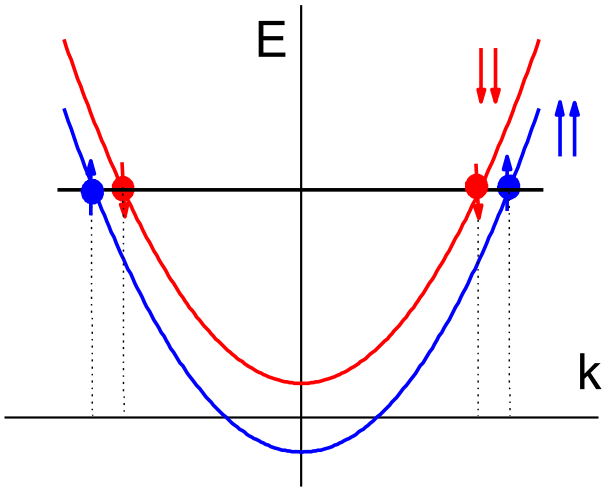

Figure 2.13 **Triplet spin bands.** Cartoon depiction of long-range triplet (like-paired) spins entering the same spin bands within a ferromagnetic material.

The like-paired spins now enter the same spin bands within the propagation layer, as shown in Figure 2.13. As a result, there is no longer a center-of-mass momentum, nor the spacial oscillation.

This means there is a much longer coherence length analogous to the decay within a normal metal:

$$\xi_{F,\text{ long-range spin-triplet}} = \sqrt{\frac{\hbar D_F}{2\pi k_B T}} \tag{2.35}$$

in the diffusive limit. This generation of long-range spin-triplet supercurrent in ferromagnetic layers was shown in the Birge group in 2010 [15], sparking even more experimental and theoretical work since [51].

2.3.9 φ_0 Junction

From the physics discussed in the previous sections, one might assume that a superconductor/ferromagnet system can only impart a phase drop of 0 or π across a Josephson junction, but this is not necessarily true. A JJ with a single ferromagnetic layer of varying thickness, where some regions prefer the 0 state and some the π state, can form ground states at $\pm\varphi$, where φ can take any value between 0 and π. These so-called 'φ-junctions' [52, 53, 54, 55, 56] still notably obey the time-reversal symmetry relation $I_c(-\phi) = -I_c(\phi)$.

Alternatively, it has been theorized that a Josephson device could be created that imparts a tunable, arbitrary phase drop of φ_0, which can take any value between 0 and 2π, in an effect referred to as the *anomolous Josephson effect (AJE)* [57, 58, 59, 60, 23, 61, 62, 63, 64, 65, 66, 67, 68, 69, 24, 70, 71, 72]. Crucially, such a device breaks the time-reversal symmetry relation $I_c(-\phi) = -I_c(\phi)$. This so-called φ_0-*junction* has been demonstrated in junctions containing exotic materials with very strong spin-orbit coupling [73, 74, 75, 76, 77, 78, 79, 80]. A design realizing this in traditional ferromagnetic materials using non-coplanar magnetizations was progressed toward perviously in this research group by Victor Aguilar [25], but has yet to be fully demonstrated.

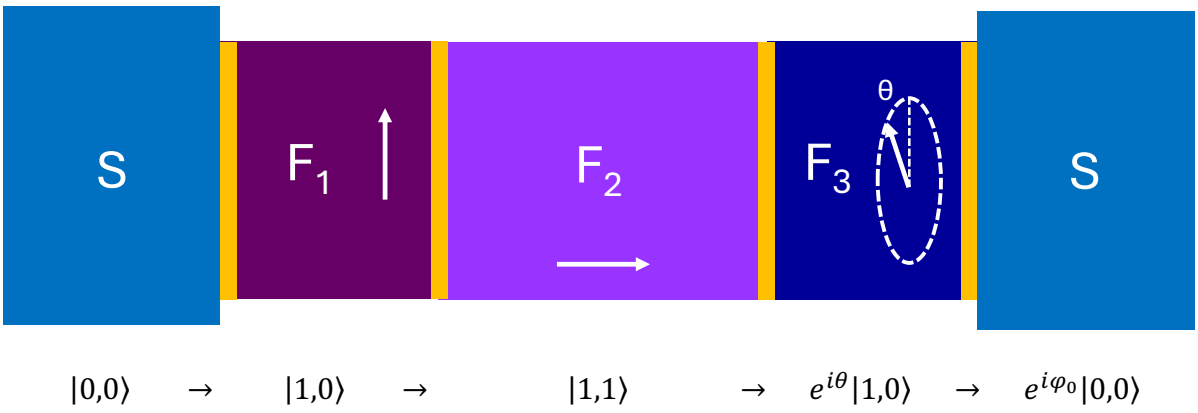

Figure 2.14 φ_0 **JJ design.** Diagram of a φ_0 junction design with one fixed-magnetization spin-mixing layer on the left, one variable-magnetization spin-mixing layer on the right, and a central PMA propagation layer, along with a representation of the progression of the dominant spin pairing within each layer (below), with $\varphi_0 = \pi + \theta$.

In this ferromagnetic system, the proposed design is shown in Figure 2.14, with a fixed magnetization spin-mixing layer on the left (F_1), a central perpendicular magnetic anisotropy (PMA) propagation layer (F_2), and a tunable magnetization mixing layer on the right (F_3). The progression of the wavefunction through the junction is similar to that described in Section 2.3.8, only, as it moves from F_2 to F_3, it picks up a phase based on the relative orientation, θ, of the magnetizations of F_1 and F_3[1]. The work shared in Chapter 5 is motivated by the hope of realizing this goal.

[1]While the hand-waving explanation is given above, the calculation for supercurrent propagation through such a system is quite involved and is given in truncated form in Appendix B.1.

CHAPTER 3

SAMPLE FABRICATION AND MEASUREMENT

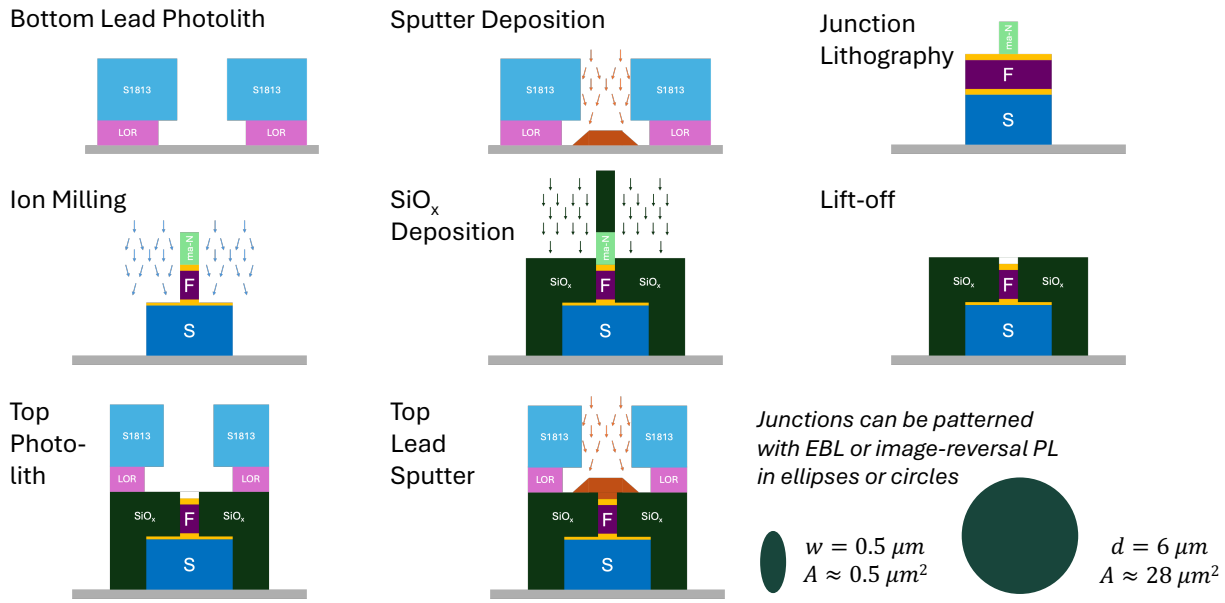

Figure 3.1 **Fabrication overview.** An overview of the sample fabrication process in a not-representative-of-scale side view showing bottom lead patterning, sputtering deposition, junction patterning, ion milling, SiO_x deposition, lift-off, and top lead patterning and deposition.

So, you'd like to make a Josephson junction. This chapter will show you how to do it, and a graphical overview of the process is shown in Figure 3.1. Let's start with the substrate. We choose a 3" silicon (100 orientation) prime wafer from PureWafer because it has been shown to be exceptionally smooth and has proven itself through countless fabrication runs. A 3" diameter size is chosen because it can be subdivided into approximately 18 square chips of side length 0.495" that fit within the existing sample holders used for deposition and measurement, and there is room for 16 samples within the sputtering deposition system, leaving a couple chips for spares.

3.1 Wafer Dicing

To precisely dice the wafer, the Advanced Dicing Technologies 7122 automatic dicing saw is used. Because it is housed outside of the clean room, and to protect the smooth silicon surface from debris from the dicing saw, the wafer is first covered in photoresist. This mimics the later process as a part of photolithography but is much more forgiving. The fresh wafer is unboxed within the clean

room and is immediately placed on the large diameter spinner chuck. Because the resist used for photolithography (Microposit S1813 G2) must be freshly poured every 3 months, there is typically some disused resist that is suitable only for protecting the wafers. To form a thick protective layer, a spin rotation of 3,000 revolutions per minute (RPM) for a time of 50 seconds is used but care is taken to begin the rotation at a minimum speed to first ensure the wafer is aligned correctly so it does not wobble and shatter at the high rotation speed. Once the spin speed is ramped up safely to 3,000 RPM, the spinner can be stopped and a generous (nickel-sized) drop of resist can be placed on the center of the wafer to spin for the 50 second recipe. Four wafers will fit on the 'cookie sheet' for the resist oven at a time, so the wafers can be easily baked in sets of four. The wafers are baked at 90° C for 45 minutes. The protected wafers can then be transported outside the clean room to the wafer dicer. The wafer dicing program is fully automated, so the main concern is aligning the dicing grid pattern to maximize the number of useable pieces out of each wafer. The flat side of the wafer is aligned with the first array of cut angles, then the first cut positions are indicated as a part of the automatic alignment program. Note: for the nickel blade, a side length of 0.495" is used, and for the resin blade, a side length of 0.485" is used to ensure that the chips will fit within the holders due to the rougher cut edge of the resin blade. The cutting blade diameter is automatically measured and calibrated every few cuts so the correct depth can be precisely made. The wafers are 15 mils thick, and an appropriate depth of cut is 8 mils to balance ease of dissecting yet transport durability. Once the wafers are diced, they can be taken back in the clean room for separation and cleaning.

3.2 Chip Cleaning

Within the protection of the class 100 portion of the clean room, the wafers can be separated and immediately placed in individual test tubes containing acetone, which dissolves the photoresist. Eight test tubes easily fit within a 250 mL beaker of water, which is heated for 5 minutes at 60° C to facilitate the dissolution of the resist. This containing beaker is then placed in an ultrasonic bath for an additional 5 minutes. Then, each test tube has the acetone replaced with isopropyl alcohol (IPA) and is sonicated for another 5 minutes. The chip will stick to the sides of the test tube, so it can

be inverted over a waste beaker and irrigated with the IPA to ensure all acetone is removed. After sonication in IPA, the IPA is replaced with deionized (DI) water and again sonicated for 5 minutes. Then each chip is removed from the test tube with tweezers and laid flat upon a dust-free clean room cloth and immediately blown dry from directly above with the wall-sourced compressed nitrogen gas. The moisture on the backside of the chip will adhere it to the cloth and prevent it from blowing away provided the airflow is from directly above and within $\sim$ 2 inches of the surface. To ensure good adhesion of the photoresist and eventually the bottom lead material, the chips are then plasma etched in an O_2 plasma etcher. The etcher is first run empty at the maximum power of 300W for a duration of 300 seconds, then the holder plate is cleaned with acetone and IPA to ensure there is not contamination from previous users. After loading and pumping to a base pressure of 50 mTorr, the substrates are etched at 300W for 300 seconds. After plasma etching, photoresist can be applied.

3.3 Photolithography

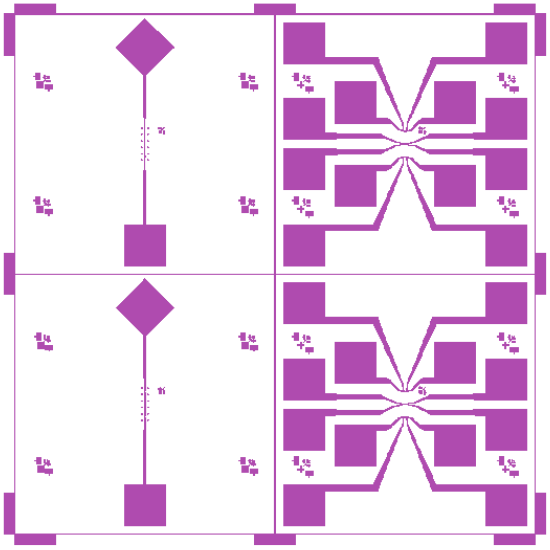

Figure 3.2 **Photomask pattern.** Center of pattern for single junction photomask showing the cut-outs for bottom lead exposure on the left and top lead exposure on the right, and alignment marks in the corners of each section.

Photoresist is a chemical that is reactive to ultraviolet (UV) light and can either harden (negative photoresist) or soften (positive photoresist) in reaction to a UV lamp shone through a chrome pattern (mask) and be washed away with a specific chemical (developer) to create a precise pattern that can

be either deposited through or etched away before being removed itself. An example mask pattern is shown in Figure 3.2. To create a pattern for sputter deposition of the bottom leads of our devices, a positive photoresist from Microposit called S1813 G2 is used. In contrast to its use merely as a protective layer (as discussed in the wafer dicing section above), spinning the resist for this purpose is an extremely delicate process. By virtue of the nature of the exposure of positive photoresist to a light source above the substrate, a very slight taper can form along the edges of the resist once the softened resist washes away in the developer. This can make it difficult to lift-off the resist after the deposition of material. To combat this effect, a layer of lift-off resist (LOR) can be spun on the chips before the photoresist. Because this underlayer reacts differently to the UV exposure, using a bilayer process creates a so-called 'undercut' whereby the bottom LOR layer is recessed from the top photoresist layer which mitigates this lift-off issue dramatically.

In this bilayer process, the first step is spinning the LOR, in particular LOR 5B. Because of how important this layer is, it is imperative to start with fresh LOR that has been manufactured in the last 2 years and properly stored at refrigerator temperatures. A small amount is poured out for use 3 months at a time. **FOR ALL RESISTS:** The large, refrigerated bottle must be **warmed to room temperature for approximately 3 hours before opening** to ensure there is no condensation of water within the large resist bottle as this can ruin an entire batch of resist.

To begin spinning, the smallest spinner chuck should be used so there is no adhesion of resist to the back of the chip. A clean substrate is then placed on the chuck and the spinner is calibrated to the appropriate settings of 3,000 RPM and 45 seconds and blown with wall-sourced compressed nitrogen gas. With the chuck stopped, a generous [~5 drops] of LOR are placed in the center of the chip and the spin is immediately started. Once completed, the chip can be moved to the baking 'cookie sheet'. A full run (16 chips) can be spun in this fashion before being placed in the (preheated) baking oven for 45 minutes at 180° C. As a reference and sanity check, it is encouraged to continually confirm the recipe with the resist guide document on the clean room computer at each step.

Once the LOR baking is complete, the baking oven should be left off with the door wide open

whilst spinning the top layer of photoresist in order to cool to the appropriate temperature. The chips, too, should be left to cool for a couple of minutes before spinning. The S1813 G2 photoresist is dropped and spun in a similar fashion as the LOR only with a speed of 5,000 RPM and a time of 50 seconds. These settings are crucial for a consistent thickness and UV response of the resist (which is why it is good practice to double check them every time). Again, a full set can be accumulated on the 'cookie sheet' before placing in the preheated oven for 45 minutes at 90° C.

Once the S1813 bake is complete, the chips are ready for exposure from the UV lamp. An ABM mask aligner is used to allow for precise (X/Y-axis) alignment, (θ) rotation and (Z-axis) contact with the chrome mask pattern. If proper care is taken to **NEVER move the X/Y/θ positioning while under contact**, the mask will stay clean for quite some time. But over time, some resist and LOR will accumulate on the mask, and it should be delicately cleaned by warm PG remover and gentle scrubbing with a cotton Q-tip or ideally professionally cleaned by the manufacturer.

The UV lamp should be switched on for 20 minutes to warm up before exposure to ensure a consistent intensity. The intensity of UVA and UVB is measured after warming up and compared to previous uses and the exposure time can be modified if it differs considerably. The small sample holder stage is used, and the suction holes that extend beyond the 0.495" chip must be covered with blue clean room tape so the substrate vacuum holds the chip securely in place. For the 5" masks, the appropriate mask frame is installed, and the mask is secured by vacuum as well. For the bottom lead pattern, precise (X/Y/θ) alignment is not crucial, but the pattern should be reasonably aligned with the substrate below. *What is crucial is the Z-axis contact.* Good practice aligns the chip reasonably well with the Z-axis set with a visible gap between the substrate and the mask. Then, the substrate stage is raised until ideal contact is made. With the 5" masks, this requires a keen eye because it is possible to force the substrate too far and bow the mask outward which results in poorer contact for some distance before the mask pops off. As a result, one must rely on the interference fringes— they will appear at some level of Z-axis adjustment and will move around as contact is minimized until a point where they appear to stop moving. There should be some resistance in the Z-axis adjustment knob, as well. This is the position of ideal contact.

Once the ideal alignment and contact have been dialed in, the UV lamp is brought over for automatic exposure of 3.5 seconds. After exposure, the chips are immediately developed in Microposit MF 319 tetramethyl ammonium hydroxide (TMAH)-based solution. The chips are submerged in a small beaker of the developer while being held with tweezers and agitated for 45 seconds. The resist will visibly clear in the exposed regions in approximately half that time. Then the chips are immediately rinsed similarly in a beaker of DI water for about 30 seconds. It is good practice to let go of the chip and reposition the hold of the tweezers a few times to ensure all the developer is rinsed off. Then the chips are dried again by laying flat upon a clean room cloth and blown with compressed nitrogen. The small beaker of developer and the slightly larger beaker of DI water should be refreshed every 4-5 uses. After each development, the chips are inspected and photographed with the optical microscope for quality assurance. Finally, the chips undergo a low-power plasma etch at 100W for 90 seconds to 'descum' the patterned photoresist before loading into sample holders. Sample holders are prepped in the chemical room by soaking stainless steel (shutter) parts in a 3:1 ratio solution of nitric acid and water followed by an intense scrubbing with a wire brush. Afterward, both stainless steel shutters and aluminum holders are sonicated sequentially in acetone, ethanol, and DI water for 5 minutes each and dried by heat gun. Samples are placed at the bottom of the holders and secured by copper heatsinks and stainless-steel bridges. Care should be taken particularly when tightening the bridge screws to not break the chips.

3.4 Sputtering Deposition

Bottom Nb leads, normal metal spacer layers, magnetic interlayers, and (in a separate run) top Nb leads are deposited in a 7-gun DC high-vacuum sputtering chamber custom designed by Prof. Bill Pratt and Prof. Jack Bass and maintained by Dr. Reza Loloee. Samples are placed face-down on a precision motor-controlled plate that sits atop a two-position foil-wrapped shutter plate that separates the sputtering targets from the samples and can be alternated between 'open to large guns' and 'open to small guns and ion mill' positions. There are 4 large (2.25" target) DC triode guns and 3 small (1" target) DC magnetron guns and an ion mill for cleanup and adhesion before top lead deposition. The large guns are ramped up slowly to operating voltage, which can be quite

high (~500 V). The small guns are turned on and off as needed throughout the process. *The entire process of sputtering deposition is quite involved, and care should be taken to follow the procedure in the instruction manual step by step as though an aeronautical pre-flight checklist in order to neither damage the irreplaceable equipment nor deposit material other than intended.* For this reason, I will not reduplicate those instructions, but provide an overview of the process.

For loading, the top of the chamber is removed by chain hoist. This provides access to the gun assemblies to install the appropriate targets and inspect and change the filaments as needed. The targets must be electrically isolated from the housing when installed and this can be checked first by visual inspection, then by use of a multimeter. A foil-wrapped chimney is placed atop each assembly to direct the plasma up toward the samples and a shroud is placed around this to encourage a smooth, consistent flow of argon gas. Once the samples are loaded into the top plate, all the targets are installed and checked, and the two-position shutter plate is installed, the chamber can be closed. A mechanical roughing pump is used to take the pressure from atmosphere (~750 Torr) to about 5 x 10^{-2} Torr before switching over to a cryogenic pump, and it is advised to flush the chamber with nitrogen gas and repump with the roughing pump 1 or 2 times before this as an extra attempt to mitigate contamination from water vapor. Once switching to the cryopump **(it is imperative that the roughing pump and cryopump not be open to the chamber simultaneously**), and a suitable test pressure (~5 x 10^{-6} Torr) is reached by reading of the ion gauge, the argon gas and cooling water are switched on and the guns are tested by slowly ramping to an intermediate voltage and checking for stable plasma. The guns are then ramped back down and turned off along with the argon. From this point, the chamber is warmed by heating strips overnight (with the gate valve partially open to protect the cryopump from warming). The cooling water is left on to protect the gun assemblies.

The following day, when the heater is off and the chamber has cooled to room temperature, the cryopump is fully opened to the chamber and it is pumped for an additional day to reach a base pressure of ~4 x 10^{-8} Torr. Once this pressure is reached, the deposition process can begin. First, liquid nitrogen is flowed through the cold trap in the top of the chamber to condense any remaining

water and to cool the chamber to ~ -30° C to facilitate smooth deposition. This will cause the base pressure to approach 3 x 10^{-8} Torr. The flow of liquid nitrogen is regulated by opening and closing a supply of compressed nitrogen gas to maintain a stable temperature range. The initial cooling takes approximately 1 hour, during which time the computer-controlled sputtering sequences can be written and the shutter and sample plates are aligned. Once at temperature, a supply of argon gas (purified by a gas purifier) is directed into each of the sputtering guns. Argon is used because it is an inert gas. For the triode guns, current is run through each filament which creates free electrons and ionizes the argon gas. The ionized argon is then directed toward each target by a large voltage, which then frees and propels atoms of the target materials up toward the samples. During this process, cooling water is run through the gun assemblies to keep them from overheating. The large guns are ramped up to their appropriate voltages then pre-sputtered for some time to remove oxidation and contamination from the surface.

Once the target voltages are achieved and the plasmas are stable, the deposition rates are checked by film thickness monitor (FTM). The FTM is calibrated for each material by input of reference parameters (such as density and Z-factor) and has been further verified by low angle X-ray diffraction each time a new material is used. For normal deposition rates on the order of angstroms per second, the rates are stable within 0.1 angstrom per second and can be read from the FTM directly. However, for very thin layers where a slow deposition is desired, it is necessary to average over a longer time to reduce the uncertainty. These rates are then entered into the Labview computer program, which then can interpret a desired layer thickness and convert it to a deposition time. The deposition sequence is manually generated, and care must be taken to avoid unwanted deposition as the sample plate moves from position to position over the active plasma streams. This often involves a delicate symphony of opening and closing the two-position shutter plate and turning on and off the small guns. **All information from the sputtering run must be dutifully recorded in the logbook as outlined in Appendix B.2.**

Each sample holder houses two samples, protected by a small rotating shutter designed to be opened and closed by wobble stick while under vacuum. This means that only one sample is exposed

at a time. This allows for a unique recipe, if desired, for each of the 16 samples in a run. Once all of this is orchestrated, the samples are deposited by running each recipe sequentially, with the user manually opening and closing the sample shutters in between each deposition and remeasuring the deposition rates every 2-4 samples. A typical stack (thicknesses in nm) for Josephson junctions includes a bottom superconducting electrode of $[Nb(25)/Al(2.4)]_3/Nb(20)$, which has been found to encourage smoother ferromagnetic growth. A normal metal spacer layer of fcc Cu(2) is used for lattice matching between the bcc Nb and the fcc ferromagnet(s) and possibly better band matching for supercurrent propagation. Then the ferromagnetic material(s) to be studied are deposited. A symmetric Cu(2) spacer is added atop this, then a capping layer of Au(10) to protect the interlayers from oxidation. A typical deposition recipe takes 5-10 minutes, so a full run of 16 chips will take about 2 hours.

When the last deposition is finished, the target voltages and filament currents are gently ramped down and turned off, the chamber is heated by heating strips to slightly above room temperature to discourage condensation upon opening, and the chamber is filled with nitrogen gas back to atmospheric pressure. The chamber can then be opened and samples retrieved. After transport into the clean room, and removal from the holders, samples are soaked in individual beakers of PG remover heated to 80° C to dissolve the photoresist and LOR and lift-off the excess metal deposited atop unwanted areas. The metal will begin to visibly peel from these areas after 5-10 minutes. This is followed by sonication for 30 seconds, then replacing the PG remover for IPA with another brief sonication, then rinsing in DI water and blowing dry with nitrogen gas.

3.5 Electron Beam Lithography

The samples then must be patterned with lithography to define the junction areas (lovingly referred to as 'pillars') with ion milling. Commonly, this is done by electron beam lithography (EBL) for very small ($\sim 0.5 \mu m^2$ area) junctions, although photolithography can be used for larger areas. Here I will only describe EBL for brevity. The Keck Microfabrication laboratory clean room houses a Hitachi SU5000 field emission scanning electron microscope (SEM) for this use. First, the samples are coated in EBL-responsive resist called Ma-N 2401 from Micro Resist Technology.

This is done by a similar process as described above for the photoresist, only with a spin speed of 3,000 RPM and a time of 40 seconds. The samples are then heated on a hotplate set to 90° C for 60 seconds. To make lift-off easier, in a process developed by Dr. Reza Loloee and Dr. Demet Korucu, the samples are then coated, spun, and baked once more to form a thicker layer. The samples are spun in batches of 5 to correspond to the number of sample slots in the ion mill chamber.

Once spun and baked, the samples are placed on a sample holder designed for the SU5000 along with a patterned chip used for stigmation and loaded into the SEM. The SEM chamber is pumped out with an integrated vacuum system controlled by the software. The SEM software is very intuitive and guides the user through the process of turning on and calibrating the electron beam. Since the EBL patterning is carried out at 1000x magnification, the stigmation should be done at many multiples of that (~30-40k). Care is taken that the working distance is set to 15 mm and the beam current is measured by use of a small hole in the sample holder that acts as a Faraday cup. This current measurement is used to calibrate the dwell time of the beam to deliver a consistent exposure dosage. An alignment protocol is used to bring the beam writer directly over the intended spot on the bottom lead. Then a computer-aided design (CAD)-drafted pattern is used to direct the beam to expose only the small areas that will define the pillars and pinwheel designs that give an impression of proper stigmation after development. The standard design incorporates elliptical pillars of $0.5\mu m^2$ area, but can be easily modified for different shapes or sizes.

After exposure in the SEM, the samples are removed and developed by agitating in AZ 300 MIF TMAH-based developer for 10 seconds, immediately rinsed in DI water (repositioning tweezers to prevent streaking from residual developer) and blown dry with nitrogen gas. Since the e-beam resist is a negative resist, the exposed portion is hardened and the unexposed portion washes away in the developer. The samples are then imaged in the optical microscope to verify size, shape, positioning, stigmation, and focusing before being loaded in holders for the ion mill chamber.

3.6 Ion Milling

Ion milling can be thought of as reverse sputtering. A filament is heated in a chamber of argon gas, which ionizes the gas, then an accelerating voltage is applied which propels the ions

up toward a sample where their kinetic energy knocks off atoms of material layer by layer. In this fabrication process, it is used to define the pillar of material that will become the Josephson junction by removing all excess material. The samples are loaded into individual holders using a mask to restrict the milling to the central area of the chip. Then a small amount of silver paste is used to adhere the sample to the copper heatsink, which is then attached to a magnet for manipulation in the load lock of the chamber and clearly labeled by sample number with a permanent marker. Heatsinking is very important because the build-up of heat from the ion beam can be deleterious to the E-beam resist. Loading of the sample holders is done in the clean room, then the samples are transported out to the ion mill chamber.

The ion mill chamber is like a smaller version of the sputtering chamber described in the earlier section, except it has only 4 locations for deposition and milling (ion mill, Au sputtering, SiO_x thermal evaporation, and *null*) and 5 sample holder slots plus an FTM. The Au sputtering gun is used the deposit upon the FTM for calibration of the ion mill rate. The SiO_x boat is used to electrically insulate the top and bottom leads from each other after ion milling, and the 'null' position is used as a safe position for the shutter opening during preparation for deposition and milling. There is a rotating shutter plate and a rotating sample holder plate, both of which are manually controlled. The chamber also incorporates a magnetic load lock which allows the main chamber to remain under high vacuum except during maintenance and repair. As with the sputtering deposition chamber, the instruction manual should be followed step by step to ensure protection of the apparatus and samples, so this section will only provide an overview of the process and the instructions will not be exhaustive.

The load lock incorporates a small loading chamber, a magnetic transport arm, a mechanical roughing pump, a nitrogen gas port, a swinging access door, and a gate valve which separates the main chamber. The loading chamber is first isolated by closing the gate valve (ensure the loading arm is clear) then brought to atmospheric pressure by opening the nitrogen port. Then the access door is opened whilst the nitrogen is flowing, and the first sample holder is attached to the magnetic loading arm. The access door is held closed, while the nitrogen flow is shut off and the roughing

pump is immediately opened to the loading chamber. To keep the main chamber very clean, a so-called 'pump and flush' routine is used where, upon reaching a pressure below 1 x 10^{-1} Torr as read by the convection gauge, the roughing pump is closed, and the nitrogen port is opened until a pressure of 1 x 10^{+2} Torr is reached. This can be repeated 2-3 times depending on the humidity to minimize water vapor in the main chamber. The roughing pump is then again used to achieve a pressure below 7 x 10^{-3} Torr which is suitable to hand-off to the turbo pump of the main chamber. *As with any vacuum system, only one pump should be open to a chamber at a time, so the load lock gate valve is only opened after the roughing pump valve is closed.* It should be opened slowly at a rate that keeps the main chamber pressure (as read by the ion gauge) below 1 x 10^{-6} Torr at all times to protect the turbo pump. Once the gate valve is opened fully, the loading arm is lowered into the chamber and the sample plate is rotated to accept the sample holder. Once the holder is seated, in a feat of coordination suitable for Cirque du Soleil, the sample plate is deftly twisted whilst the magnetic arm is briefly held steady then abruptly removed to avoid reattaching to the sample holder. The arm can then be fully extracted back into the load lock, which can then be isolated again. This process is repeated for each sample until the chamber is fully loaded. The chamber is left to pump for about 4 hours after loading to recover a base pressure of ~3 x 10^{-8} Torr.

Upon reaching a suitable base pressure, argon is flowed into the chamber, the gate valve to the turbo pump is closed to reach an Au sputtering pressure of 7 x 10^{-4} Torr, and the cooling water is verified to be running. The Au gun is then turned on with the FTM positioned over it, and the shutter plate is opened. The FTM display is zeroed, and Au is deposited upon the FTM until a thickness of 2000 angstroms is reached (400 angstroms for each sample). The Au gun is then shut off, and the FTM is positioned over the ion mill, and the pressure is reduced to 2.3 x 10^{-4} Torr by opening the turbo pump valve. With the shutter plate closed, the ion mill beam is switched on and warmed up and all posted parameters are verified to be within range (it will take about 10 minutes for the beam to become stable). At this point, the ion mill rate is checked by opening the shutter to mill away the some of Au deposited on the FTM. For the most reliable rate, a stopwatch is used to determine how long it takes to mill 100 angstroms as read by the FTM display, and an Au mill rate

is then calculated in angstroms per second and should be about 5.5.

Since the nominal mill depth penetrates the top cap of Au, the top Cu spacer, all of the magnetic layers, and halfway through the bottom Cu spacer, the thickness of each layer is multiplied by a k-factor, *which is the ratio of the mill rate through Au to the mill rate through each material*, and added together giving an overall 'equivalent thickness' to aid in calculating the mill time. These k-factors have been experimentally determined by surface profiling before and after milling. To keep these calculations straight by sample, a spreadsheet is made which can be quickly edited as the mill rate is measured to calculate a mill time in seconds.

With the mill time calculated, the sample is moved over the ion mill, the shutter is opened, and a stopwatch is used to precisely time the milling. The mill rate is verified between each sample but should remain relatively stable throughout. Once all samples have been milled, the ion beam is switched off, the FTM is moved over the SiO_x boat (with the shutter closed), the argon is turned off, and the SiO_x boat is slowly warmed by increasing the voltage applied across it until reaching the target setting. The deposition voltage will vary slightly as the Si is depleted from the boat, but should be tuned for a deposition rate of about 7 angstroms per second as measured on the FTM (ensure the display is set to the proper program). Then, similar to how the samples are exposed for ion milling, each sample is held over the SiO_x boat for the appropriate time to deposit 50 nm of insulating SiO_x. Then, the SiO_x voltage is turned down slowly and the samples are unloaded via the load lock.

3.7 Side Ion Milling and Lift-off

For such small features as the $0.5\mu m^2$ pillars, lift-off of the E-beam resist can be problematic. To aid in lift-off, the samples are taken out of the ion mill holders (being careful to remove the silver paste from the back with cotton-tipped swabs) and placed in holders that orient the chips at an 87° angle (with the ion beam parallel to the bottom lead) to break through any redeposited layers of metal from the top-down mill or stray SiOx creeping up the sides of the pillars. The process from loading to milling is identical as above, only the milling is done for 2 minutes, 2 times for each sample in each orientation (top up and top down).

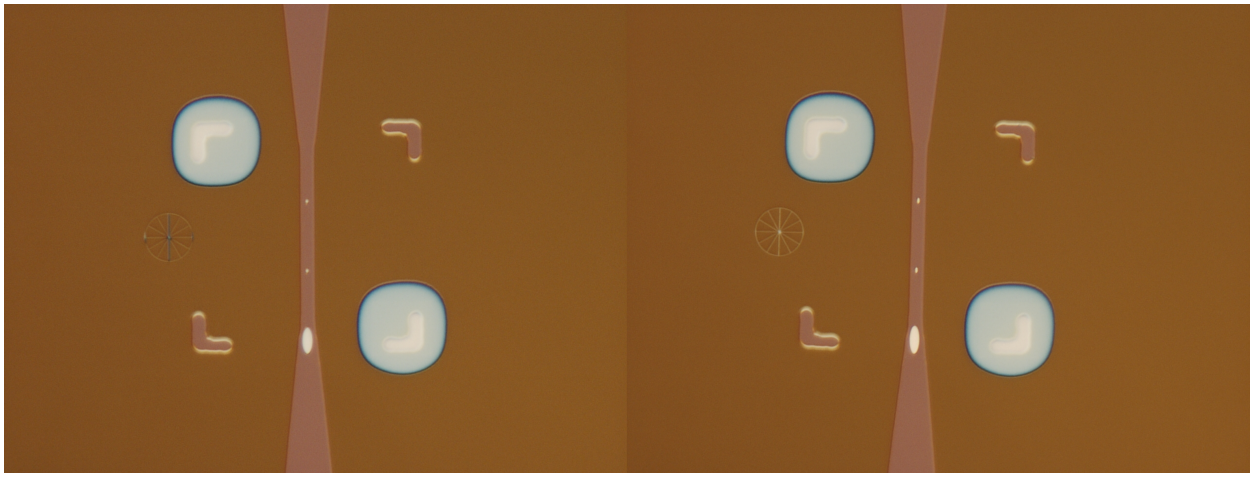

Figure 3.3 **EBL lift-off.** Before (left) and after (right) pictures of the lift-off process. The small ellipses in the center and the pinwheel design have lifted off and appear brighter while the outer L-shaped alignment marks have not.

After side milling, the samples are removed from the holders, imaged with the optical microscope, and immediately placed in PG remover lift-off solution in individual beakers of a hot plate set to 80° C for 10 minutes. They are then scrubbed (in the junction region) very gently with cotton-tipped swabs and heated for an additional 20 minutes before being capped with aluminum foil and left to soak overnight. Then the samples are swished in a beaker of IPA, a beaker of DI water, and blown dry with nitrogen gas. The samples are imaged again, and the images are compared before and after lift-off. As shown in Figure 3.3, properly lifted-off junctions will appear noticeably brighter and larger than those capped in resist.

3.8 Top Lead Photolithography and Sputtering

After lift-off, the samples can be patterned for the final deposition of top leads. The recipe for the bilayer resist spinning, baking, exposure, and development is identical as for the bottom leads, with the crucial difference being that the X/Y/θ alignment is now critical. The top lead pattern of the photomask includes alignment marks that correspond to the alignment marks on the bottom lead pattern which are now deposited material. There are four sets of alignment marks on the four corners of the chip, and they each must be used to ensure that the top leads will overlap the junction pillars. Again, the X/Y/θ movements must be made when the mask is out of contact with the resist to keep the mask clean. Once the exposure and development is complete and the samples

are again imaged on the optical microscope to verify the alignment, they undergo another 100W for 90 second descum in the plasma etcher before being loaded in the sputtering sample holders.

The sputtering process for top leads is the same as above except for a few tweaks. First, the base pressure does not need to be as low since the top leads need only to be superconducting and not a base for ferromagnetic structures, so the additional day of pumping to reach 4 x 10^{-8} Torr can be skipped if needed. And, to promote good adhesion of the top lead, 5 nm of the Au(10) top cap is ion milled away *in situ* immediately before the Nb is deposited. Additionally, the smoothing interlayers of Al used in the bottom lead are not needed, so simply 150 nm of Nb is deposited then a final cap of Au(10). After top lead deposition, the resist is lifted off just as with the bottom leads, and the samples are ready to measure.

3.9 Josephson Junction Measurement

Once completed, samples are measured by mounting on one of two dip probes designed by Prof. Bill Pratt, then dipping in a dewar of liquid helium. Both probes employ flying leads attached to the sample by pressed indium and drive current through a junction and measure the voltage across it in a 4-probe setup to collect I-V curves. The first probe, referred to as 'quick dipper I' or QDI, includes a SQUID comparator circuit that amplifies the voltage measurement for low-noise data collection [81] on samples with a very small critical current. QDI also includes an integrated superconducting solenoid for application of a magnetic field. The second probe, QDVI, has all of its electronics at room temperature, so it is not suitable for such a sensitive measurement. And it must be dipped with a separate solenoid-containing sheath (which consumes addition He through boil-off) in order to apply a magnetic field. However, it can connect up to 5 junctions at once to allow for multiple measurements for each dip. Both systems can deliver a set of I-V curves across a range of magnetic field steps for characterization of the junctions by their magnetic response.

3.10 SQUID Magnetometer Measurement

Samples deposited without patterning, thin films, are measured for magnetic characterization in a Quantum Design MPMS3 SQUID-vibrating-sample magnetometer (VSM). As our deposition equipment is set up for 12.7 x 12.7 mm samples (0.5" squares), this begins with careful scoring

and quartering (an alternate method is described in Appendix B.3). This results in ~ 6.4 x 6.4 mm squares, which slide into measurement straws and secure with a friction fit. The measurement straws are designed to slide onto the loading stick which places the sample in a vacuum chamber. Once pumped out, the closed loop cryogenic system can be set to any desired measurement temperature, down to about 2 K. S/F samples are typically measured above the T_C of Nb at 10 K. Once cooled to the desired temperature, the sample is aligned with a manual DC scan (to account for thermal variations), then a custom sequence can be run to measure, for instance, moment vs. field or moment vs. temperature. Geometrical measurements are taken with an optical microscope once removed to normalize for area.

CHAPTER 4

NI-MN PROJECT

One potential application of ferromagnetic Josephson junctions is within a superconducting computer in the form of the switching part of a memory cell, in Josephson magnetic random-access memory (JMRAM). The design, proposed by Anna Herr and colleagues [5] and implemented by Northrop Grumman [7] involves a two-layer ferromagnetic junction within a SQUID loop whereby the phase difference across the junction is switchable by changing the relative orientation of the magnetizations of the two layers. One layer remains fixed in its magnetization, and one layer is switchable (free) under a small magnetic field. The phase accumulation through the ferromagnetic layers, in some sense, adds when the magnetizations are parallel and subtracts when they are antiparallel. This effect was first demonstrated in the Birge group by Bethany Niedzielski and Eric Gingrich [6] as a part of the collaboration with Northrop through the IARPA C3 program. Two key requirements toward the scalability of this design were optimizing both the softness and coherent rotation of the free layer and the robustness of the fixed layer. The original design used $Ni_{81}Fe_{19}$ (a.k.a. permalloy) as the free layer and pure Ni as the fixed layer. Appendix A will briefly discuss the study of NiFeCr for use as the free layer, and this chapter will discuss the exploration of antiferromagnetic (AF) Ni-Mn used to pin the fixed layer through an effect called exchange bias. The text in this chapter is adapted from work published in IEEE Transactions on Applied Superconductivity [26]

4.1 Exchange Bias

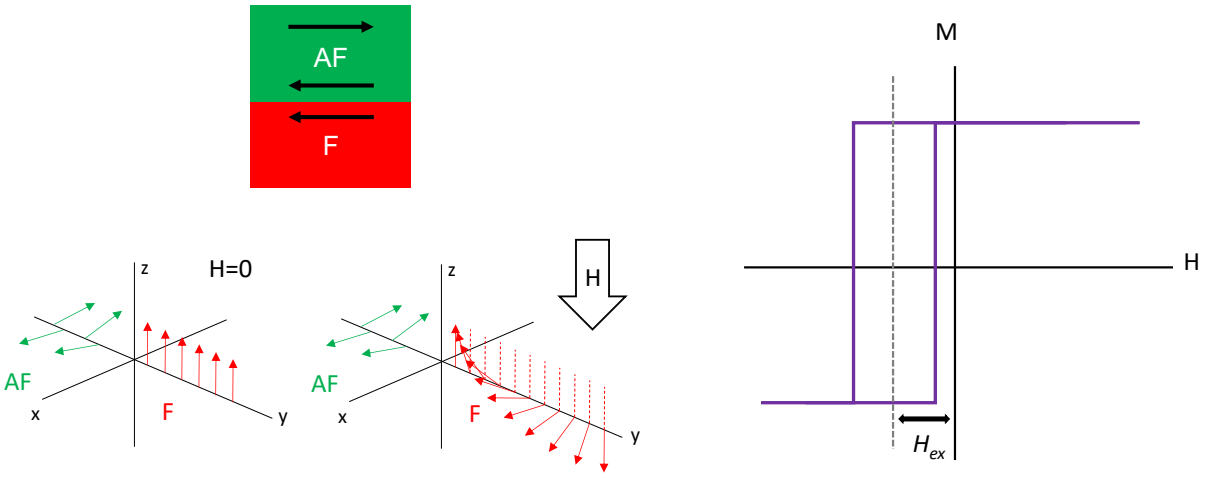

Figure 4.1 **Exchange bias.** A visual interpretation of the exchange bias effect on the left, adapted from O'Handley [82], and an idealized hysteresis curve on the right showing the characteristic shift indicating a preferential direction of the magnetization.

In an antiferromagnetic material, electron spins of neighboring atoms tend to align into layers with antiparallel orientation causing the material to have an overall net magnetization of zero. When such an antiferromagnetic material is placed next to a ferromagnetic material, this tendency results in an exchange coupling with the interfacial spins in the ferromagnetic layer which resists their reorientation. The cartoon in Figure 4.1 shows a representation of this adapted from O'Handley [82] and an idealized magnetic response plot (hysteresis curve) of this F/AF system. As shown by the horizontal shift, this 'exchange bias' effect imparts a preferred direction of the magnetization of the F-layer. This effect is used quite commonly in magnetoresistive random-access memory (MRAM) [83, 84, 85] which relies on tunneling magnetoresistance, which is similar to the giant magnetoresistance effect [86] whereby the *resistance* of a two-layer ferromagnetic system changes based on the relative orientations of the magnetizations of the layers.

Another important characteristic to determine when considering applications of AF materials is their so-called 'blocking temperature'. This is the temperature below which the exchange bias is maintained. In MRAM application, the layers are thick enough that this temperature is above room temperature, so the materials must be heated above, then cooled through this critical temperature whilst a magnetic field is applied to impart the exchange bias. In an F/AF system, the blocking

temperature can be determined by establishing the exchange bias, then warming in a small field in the opposite direction. At the blocking temperature, the magnetization will switch sign as the AF material 'lets go' of the ferromagnet and it is free to switch.

4.2 Past Work

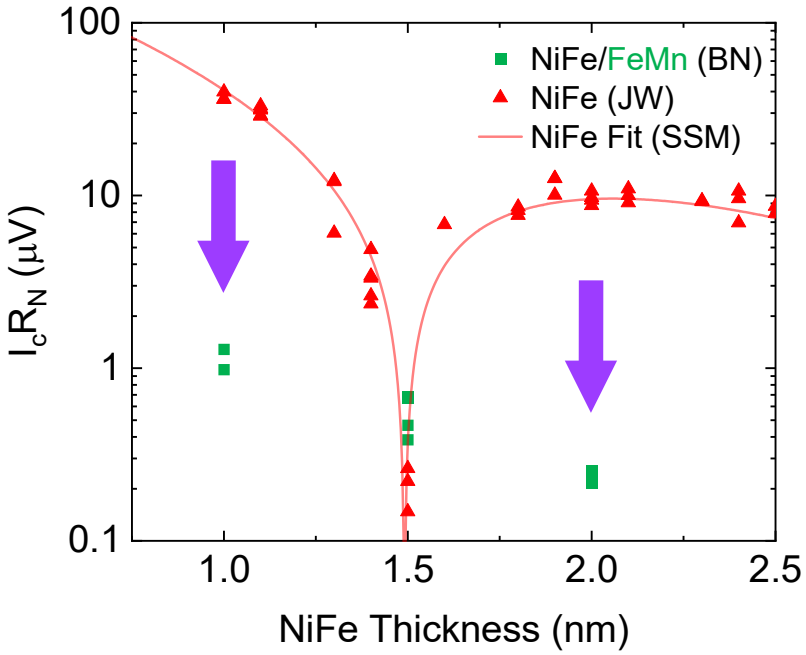

Figure 4.2 **FeMn/NiFe bilayer JJs.** A graph of the critical current times normal state resistance vs. thickness of FeMn/NiFe bilayers compared to NiFe alone showing a large suppression from the additional AF layer.

Previously in the group, AF materials have been investigated for this purpose, namely FeMn by Bethany Niedzielski [87] and IrMn during my time as an undergraduate [unpublished]. While these materials are characterized quite well for MRAM application, two critical questions remain when considering their usage in JMRAM: 'is the exchange bias effect present in very thin (on the order of nm) layers?', and 'is it possible to propagate supercurrent through the AF/F system?'. Both materials indeed demonstrated the exchange bias effect in thin magnetic layers, but fell short in the propagation of supercurrent, as seen in Figure 4.2, where there is a large suppression of the supercurrent observed from the addition of the AF layer and which combines data from Bethany Niedzielski [87], and Josh Willard and Swapna Sindhu Mishra [11]. Before abandoning this idea entirely, we decided to investigate Ni-Mn due to the increased supercurrent transmission of Ni in

comparison to Fe and Ir.

4.3 Magnetic Characterization

We began by fabricating sheet films for characterization in the Quantum Design MPMS3 SQUID VSM. Using sputtering deposition as described in Chapter 3, only without any patterning, thin films were deposited on Si substrates. The 0.5" chips, when quartered, are the ideal size for measurement in the VSM. Test samples were made both to calibrate the deposition rate and sample thicknesses with low angle X-ray diffraction and their composition with energy dispersive X-ray analysis. The analysis showed a composition of $Ni_{41}Mn_{59}$ as deposited. Samples were fabricated with the AF NiMn atop both NiFe with a structure (thicknesses given in nm) of $Ni_{81}Fe_{19}(d_F)/Ni_{41}Mn_{59}(d_{AF})$ with d_F = 2 and d_{AF} = 1.2, 1.8, 2.4 and pure Ni with a structure of $Ni(d_F)/Ni_{41}Mn_{59}(d_{AF})$ with d_F = 1.6, 2 and d_{AF} = 1.2, 1.8, 2.4. In all samples, the F/AF layers were sandwiched between a seed layer of Nb(5)/Cu(2) (for adhesion) and a symmetrical top cap of Cu(2)/Nb(5) to prevent oxidation.

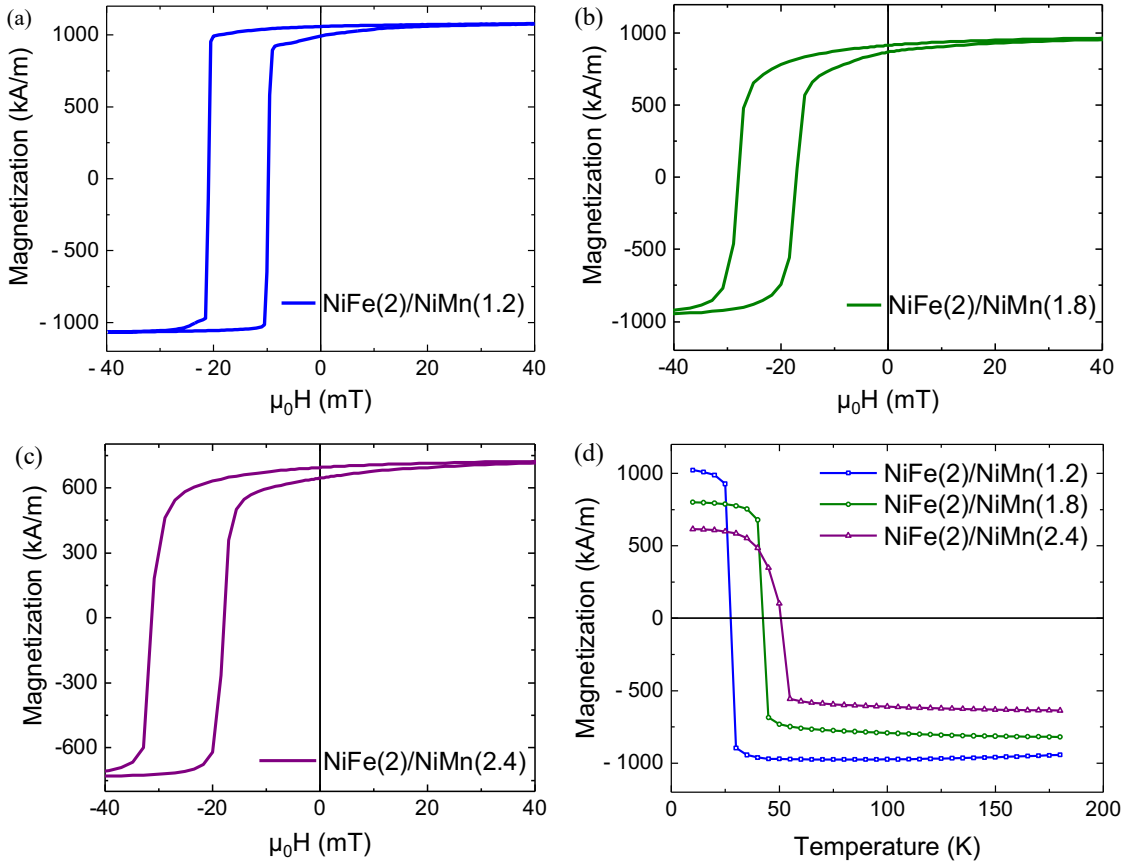

Figure 4.3 **NiFe/NiMn thin films.** Magnetic hysteresis curves (a)-(c) of NiFe/NiMn bilayer films of thicknesses as labeled (in nm). All samples show characteristic horizontal shift indicating expected pinning behavior of the AF layer placed adjacent to the F layer. The blocking temperature (d) was measured by establishing exchange bias in the positive direction, then warming the samples in a small negative applied field.

Fig. 4.3 shows the magnetization vs. magnetic field for the NiFe/NiMn bilayer samples, after cooling in a magnetic field of 0.1 T oriented in the positive direction. As expected from the exchange bias effect, the curves are shifted toward negative fields indicating a pinning behavior of the F/AF system. The magnitude of the exchange-bias shift increases with increasing NiMn thickness, but is substantial even with a NiMn thickness of only 1.2 nm. The blocking temperatures of the samples were measured by establishing exchange bias in the positive direction, then warming each in a small negative applied field and plotting the magnetization vs. temperature. All samples showed blocking temperatures below 50 K.

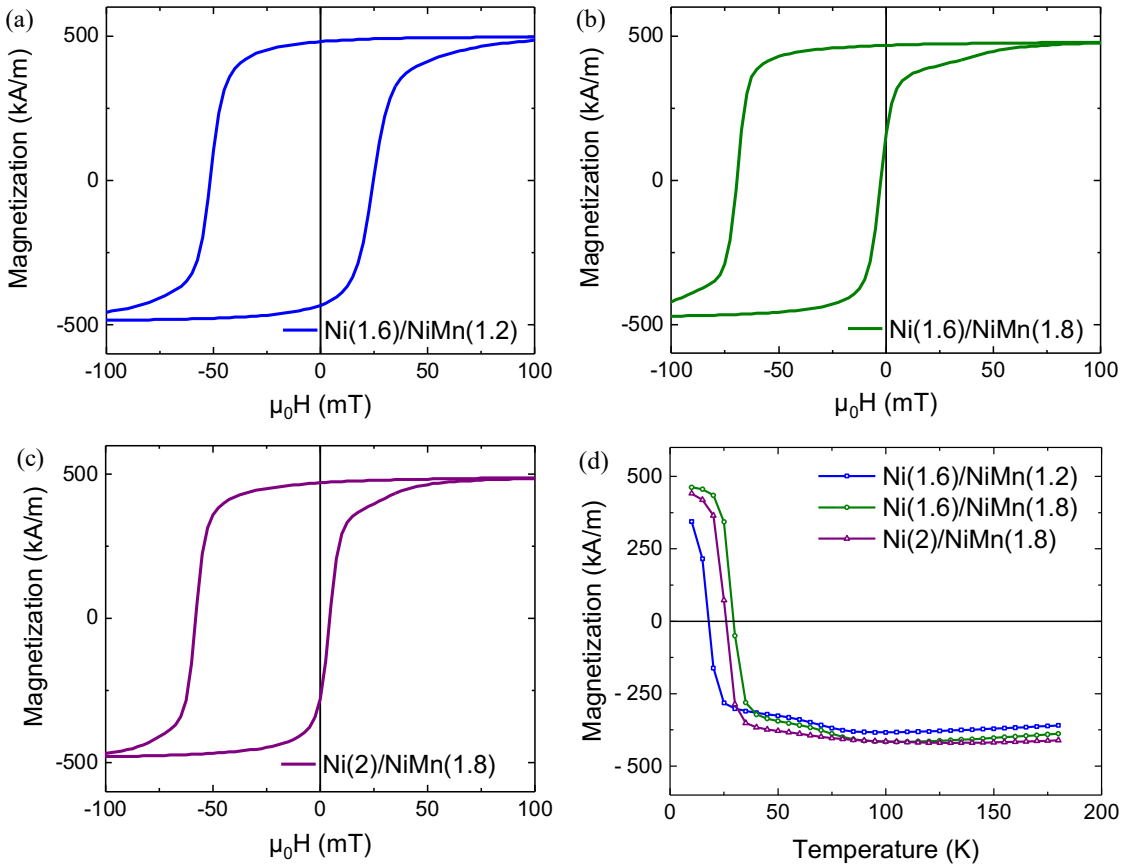

Figure 4.4 **Ni/NiMn thin films.** Magnetic hysteresis curves (a)-(c) of Ni/NiMn bilayer films of thicknesses as labeled. All samples show characteristic horizontal shift indicating expected pinning behavior of the AF layer placed adjacent to the F layer. Panel (d) again shows the blocking temperature measurement performed as described in Fig. 4.3.

Fig. 4.4 shows similar data for Ni/NiMn bilayers. The wide hysteresis loops are due to the high coercive fields of the thin Ni layers [88], but again there is a noticeable exchange bias with a NiMn layer of only 1.2 nm. An additional Ni sample was fabricated with a NiMn thickness of 0.6 nm, but it did not show exchange bias.

4.4 Josephson Junctions

Having demonstrated the desired exchange bias behavior with such thin Ni-Mn layers, we then proceeded to fabricate and measure Josephson junctions. While the proposed application in cryogenic memory would require an S/F/N/F/AF/N/S structure, our group's previous attempts to study such systems resulted in nearly immeasurably small critical currents. This informed the decisions both to begin with the simpler S/N/AF/N/S structure as well as using larger area

junctions than are typical in our recent research. The thought behind this was that this would allow extrapolation that would inform viability through critical current density J_C. Fabrication was similar to that described in Chapter 3, however junction patterning was done by photolithography in an 'image-reversal' process using negative AZ 5214-E photoresist, which gives an undercut profile for ease of lift-off.

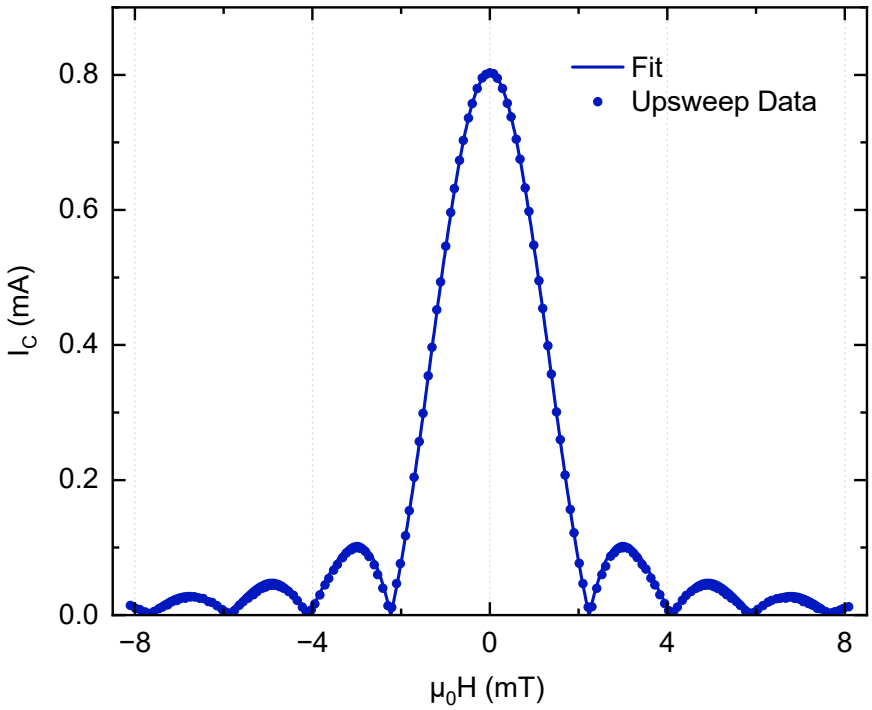

Figure 4.5 **NiMn Fraunhofer.** Magnetic field dependence of critical current for most ideal d_{NiMn} = 4.8 nm sample with a junction diameter of 6 μm. Upsweep data shown, with downsweep data indistiguishable, showing no hysteresis. The solid line is a fit to the data of an Airy function, which is appropriate for circular Josephson junctions [89].

Figure 4.5 shows the critical current plotted against magnetic field applied in-plane for a circular Josephson junction of diameter 6 μm containing a 4.8 nm NiMn layer. The data follow the characteristic interference pattern of a non-magnetic Josephson junction [89]. We note that junctions containing thinner NiMn layers ($d_{NiMn} \leq 3.6$ nm) produced less ideal interference patterns, possibly due to magnetic disorder. In contrast to ferromagnetic junctions, whose interference patterns are shifted and hysteretic due to the net magnetization of the interlayer, the AF samples in this study show symmetry about zero field and no such hysteresis.

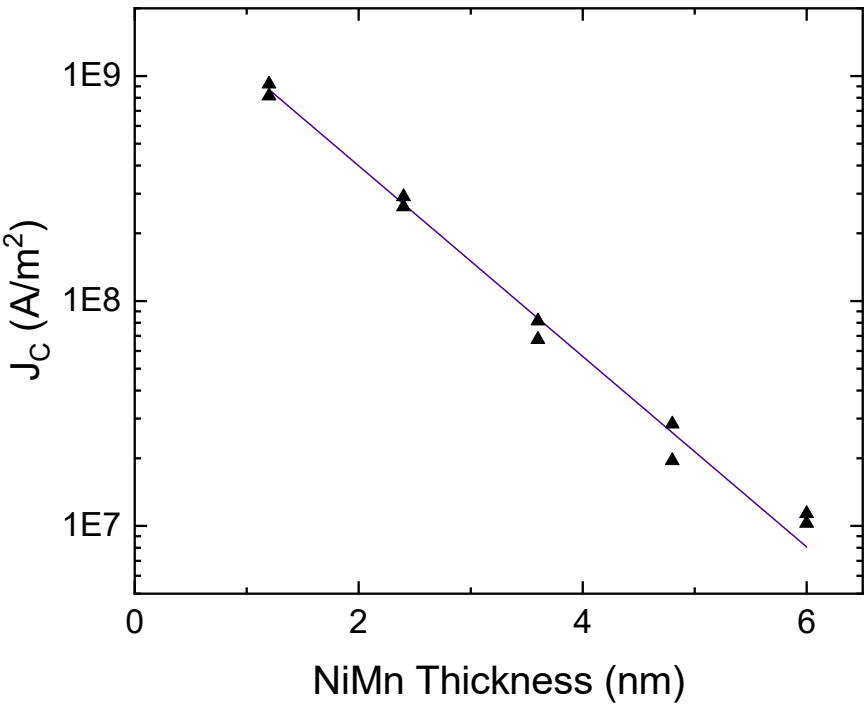

Figure 4.6 **NiMn J_C decay.** Peak critical current density vs NiMn layer thickness. The line is a least-squares fit to an exponential decay, and gives a decay length of ξ_{AF} = 1.03 ± 0.05 nm.

Fig. 4.6 compiles many such measurements and relates the peak, zero-field, critical current density to the NiMn AF layer thickness. The plot shows a steep decay and was used to determine a characteristic decay length, ξ_{AF}, within the material, expecting that $J_C \propto \exp(-d_{AF}/\xi_{AF})$. The shown fit gives us ξ_{AF} = 1.03 ± 0.05 nm. That short decay length is very close to the one measured by Bell *et al.* in junctions containing FeMn [90].

4.5 Discussion and Conclusion

The intended application of this work was to strengthen the fixed layer of an S/F/N/F'/S spin valve inside a Josephson junction used in a superconducting memory cell. Given the strong exchange bias exhibited in Figs. 4.3 and 4.4 for NiMn layers as thin as 1.2 nm, the steep decay of J_C shown in Fig. 4.6 would not be a problem if the J_C value of $\sim 10^9$ A/m^2 measured in the junctions containing 1.2 nm of NiMn is sufficient for the intended application. In considering the memory design discussed in [7], where the magnetic junction is placed in a SQUID loop that also contains two S/I/S junctions as shown in Figure 4.7, the magnetic junction acts as a passive phase shifter. This places a lower limit on the critical current of the spin valve to ensure that it is not

driven normal in the operation of the device. In the proposed device, this equates to a minimum I_C of about 200 μA. That corresponds to a J_C limit of order 2 x 10^8 A/m^2 given that the junction area must remain small (area ~ 1 μm^2) so that the free layer is magnetically single-domain and can provide clean switching.

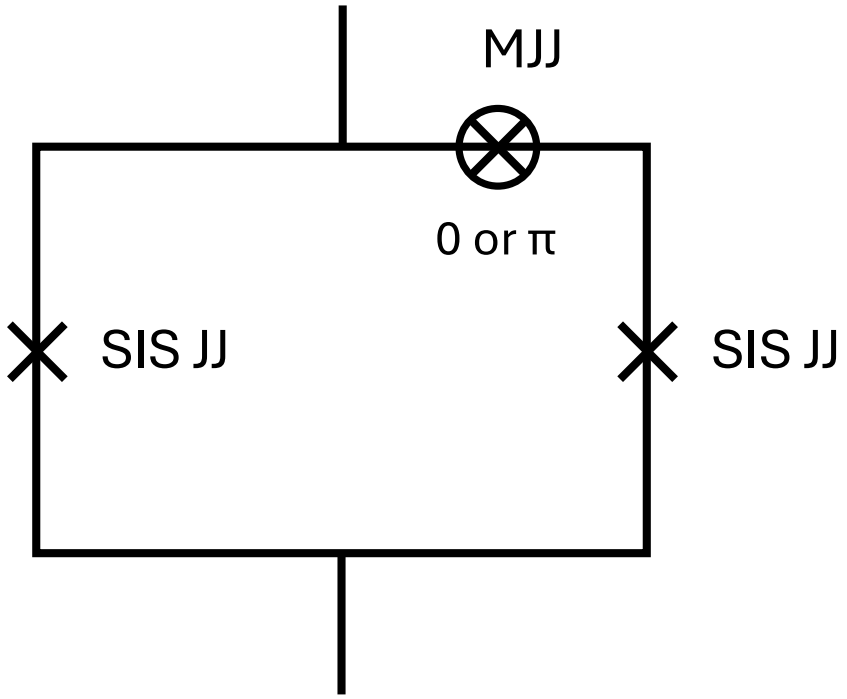

Figure 4.7 **Simplified JMRAM cell.** Schematic of a simplified JMRAM unit cell showing the two S/I/S junctions as X's and the magnetic junction as an encircled 'X' as envisioned in the IARPA C3 project, adapted from [7].

Baek observed values of the characteristic voltage $V_C = I_C R_N$ in junctions containing only Ni of about 100 μV, which corresponds to $J_C \sim 10^{10}$ A/m^2 using the approximate value for the area-resistance product, $AR_N \sim 10$ fΩm^2 [88]. Previous work in *our* group has shown that adding the NiFe free layer to this system reduces this characteristic voltage to ~ 5-10 μV [6, 9] which corresponds to a J_C of ~ 5 x 10^8 - 1 x 10^9 A/m^2, this is a reduction by a factor of 10-20. Now, more recent work has suggested that interface engineering can increase critical current transmission through the free layer by a factor of about four [11]. Had the IARPA C3 project continued, an obvious next step would have been to combine these findings in complete S/F/N/F/AF/S spin-valve junctions and determine if the reduction in critical current from the additional NiMn in the fixed

layer can be compensated by the increase in critical current from interface engineering in the free layer. Additionally, new work involving highly ordered AF materials [91] may have provided an alternative path forward as long-range supercurrents have now been observed in novel devices containing the chiral AF Mn_3Ge.

CHAPTER 5

PROGRESS TOWARD φ_0 PHASE-TUNABLE JJs

Long range propagation of spin-triplet supercurrent through ferromagnetic layers is the subject of intense study. Previous work involving trilayer magnetic systems with a central PMA layer has demonstrated the generation of spin-triplet supercurrent [20, 92, 10]. Interfacial Ni layers have been shown to enhance crtical current in permalloy ($Ni_{81}Fe_{19}$) Josephson junctions [11]. Here we present progress toward optimizing and combining these effects. As discussed in Section 2.3.9, the 'holy grail' for this line of research is the so-called φ_0-junction, predicted theoretically by many research groups [60, 23, 61, 62, 63, 64, 65, 66, 67, 68, 69, 24, 70, 71, 72], demonstrated in some exotic materials with very strong spin-orbit coupling [73, 74, 75, 76, 77, 78, 79, 80]. A design realizing this in traditional ferromagnetic materials using non-coplanar magnetizations was progressed toward perviously in this research group by Victor Aguilar [25], but has yet to be fully demonstrated. Some of the text in this chapter is adapted from our short paper in the 2024 IEEE International Magnetic Conference proceedings [93] . We begin here with a two-pronged investigation to both increase critical current (to enable easier detection) and increase magnetization coherence of the F-layers. As the device design requires non-coplanar magnetizations and spin-triplet supercurrent, the central propagation layer needs to have a perpendicular magnetic anisotropy (PMA). Previously in this research group, two main PMA systems have been investigated– $[Ni(0.4)/Co(0.2)]_n$ [20] and $[Pd(0.9)/Co(0.3)]_n$ [92, 10] multilayers. In the Ni/Co system, the propagation of critical current was strong, but the PMA effect of the magnetization was relatively weak. In the Pd/Co system, the PMA effect was shown to be stronger, but the critical current transmission weaker. We first present an attempt to bolster the PMA effect in the Ni/Co system. We then explore the magnetics of elliptical arrays of 'Ni dusting' permalloy samples as an attempt to increase critical current based on previous work in the group on such samples [11]. Josephson junctions of smaller area were also tested as the previous work has suggested that Ni layers of $0.5\mu m^2$ size are not single domain.

5.1 Methods

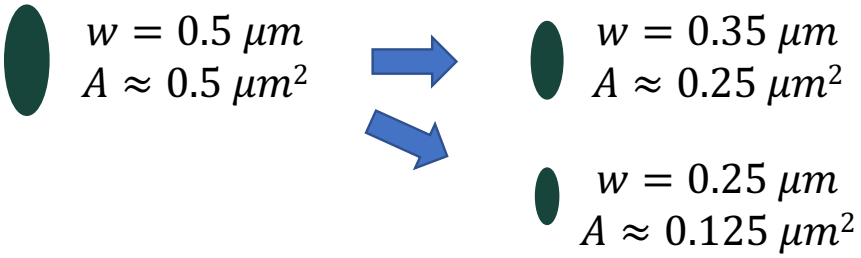

Figure 5.1 **Triplet JJ sizes.** Diagram showing the relative sizes of Josephson junctions fabricated, with the 0.5 μm^2 size on the left representing that used most commonly in the Birge group, and the smaller sizes investigated for better control of magnetic behavior.

Data from three distinctly fabricated sets of samples are shared in this chapter– sheet films of PMA Ni/Co multilayers, arrays of elliptical nanomagnets made from 'Ni dusting' Ni/NiFe/Ni trilayers (both for magnetic characterization), and spin-triplet Josephson junction samples for electron transport measurement. The basics of the fabrication follow those outlined in Chapter 3, with deviations as discussed below. Thin magnetic sheet films were sputter deposited without patterning for PMA characterization. Elliptical nanomagnets were patterned by electron beam lithography in arrays of about 8 million and defined by ion milling. Josephson junction samples were patterned by both photolithography (for top and bottom leads) and electron beam lithography and ion milling again for junction definition. Junctions had nominal areas of 0.125, 0.25, or 0.5 square microns, as shown in Figure 5.1. Junctions of different sizes were used to explore magnetic behavior of smaller areas in hopes of encouraging single domain behavior of the Ni layers in particular. Magnetic characterization measurements of moment vs. field were performed with the Quantum Design MPMS3 SQUID-VSM at a temperature of 10 K with the field applied in and out of the plane of the sample. Transport measurements were carried out using a probe with a built-in superconducting magnet inserted in a liquid helium dewar at 4.2 K. Current-voltage (I-V) curves were measured as a function of field, up to 10 mT in positive and negative directions applied along the long-axis of the elliptical junctions.

5.2 Ni/Co Multilayer Sheet Films

Fig. 5.2 shows the magnetic hysteresis loops for a $[Ni(0.4)/Co(0.2)]_6$ multilayer sample grown on a $[Nb(25)/Au(2.4)]_3/Nb(20)$ seed layer in both in-plane and out-of-plane orientations. (All thicknesses are in nm.) These data suggest a substantial preference of the magnetization to be oriented out-of-plane, with a near 100% remnance of the magnetization at zero field, and a high coercivity of 57 mT, compared to negligible remnance in-plane. Further, table 5.1 shows the coercive field, H_C, and the ratio of remnant magnetization measured in-plane to the remnant magetization measured out-of-plane (M_R) of $[Ni(0.4)/Co(0.2)]_n$ samples with n = 6, 10, 14 with and without a $[Nb(25)/Au(2.4)]_3/Nb(20)$ seed layer. These data are consistent with a very strong PMA effect in the Nb/Au seed layer samples, which compares favorably to the samples grown on Nb(5) seed layers in this study and on Nb(50) seed layer used previously in this group [20].

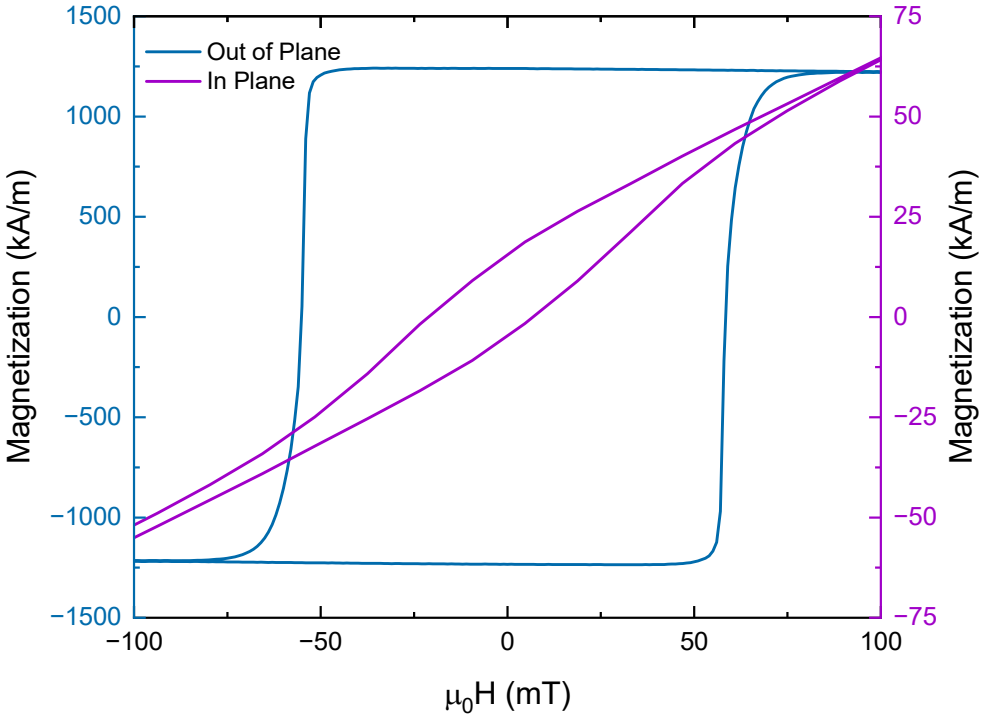

Figure 5.2 **Ni/Co n=6 thick base.** Magnetization as a function of applied field for a $[Ni(0.4)/Co(0.2)]_6$ multilayer film grown on a $[Nb(25)/Au(2.4)]_3/Nb(20)$ seed layer, measured both with the field in-plane and out-of-plane, demonstrating strong PMA.

Table 5.1 **Ni/Co magnetics summary.** Coercive field (H_C) and in-plane to out-of-plane remnant magnetization ratio (M_R Ratio) for thin Nb seed layer and Nb/Au seed layer $[Ni(0.4)/Co(0.2)]_n$ with n = 6, 10, 14.

Base	n (layers)	d_f (nm)	H_C (mT)	M_R Ratio (%)
Nb(5)	6	3.6	33.5	7.8
Nb(5)	10	6.0	45.5	12.
Nb(5)	14	8.4	30.8	6.0
$[Nb/Au]_3/Nb$	6	3.6	56.8	0.85
$[Nb/Au]_3/Nb$	10	6.0	55.0	5.4
$[Nb/Au]_3/Nb$	14	8.4	48.5	4.6

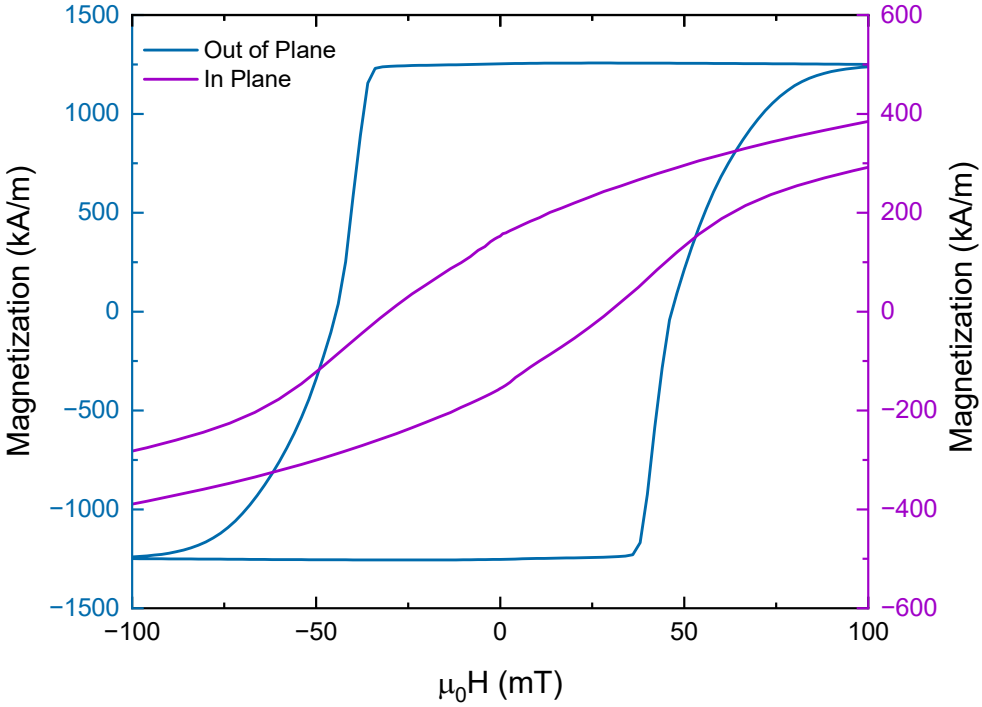

Figure 5.3 **Ni/Co n=10 thin base.** Magnetization as a function of applied field for a $[Ni(0.4)/Co(0.2)]_{10}$ multilayer film grown on a Nb(5) seed layer, measured both with the field in-plane and out-of-plane, demonstrating reasonably strong PMA.

Figure 5.3 shows the magnetic hysteresis loops for a $[Ni(0.4)/Co(0.2)]_{10}$ multilayer sample grown on a Nb(5) seed layer in both in-plane and out-of-plane orientations. Such a thin seed layer of only a couple of atomic layers should propagate the smoothness of the Si substrate, and was thought to be the ideal case for a base from a magnetics standpoint. As we see from comparison to the $[Ni(0.4)/Co(0.2)]_{10}$ grown on the $[Nb(25)/Au(2.4)]_3/Nb(20)$ seed layer shown in Figure 5.4,

this is clearly not the case. The out of plane loop is wider for the latter sample, indicating a higher coercivity, and the in plane remnant magnetization is much smaller, both of which indicate a more dramatic PMA effect.

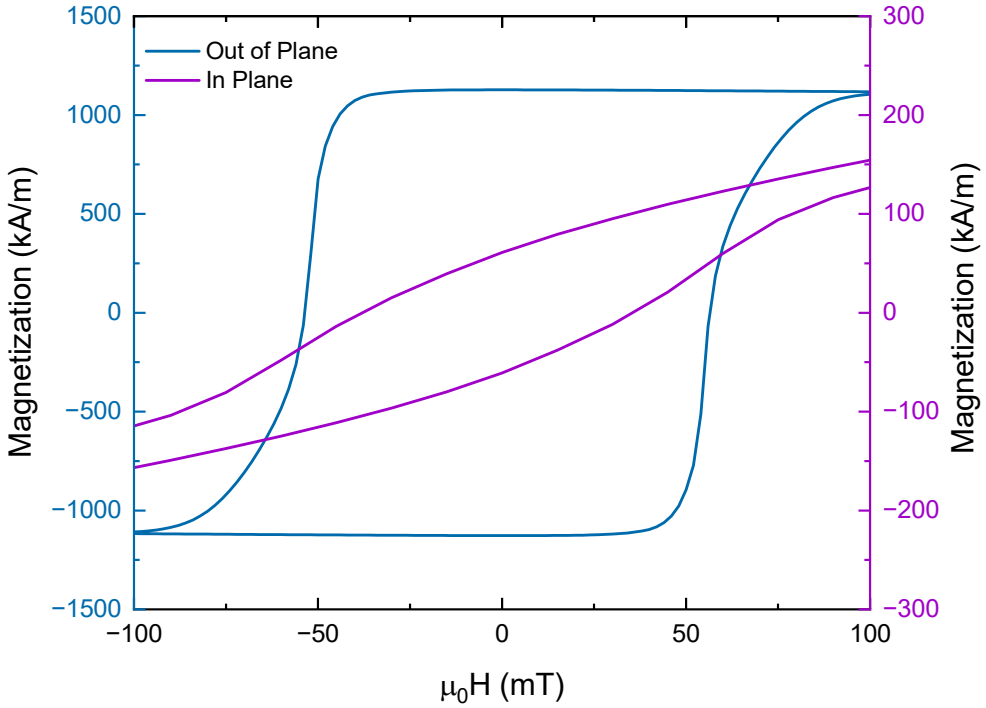

Figure 5.4 **Ni/Co n=10 thick base.** Magnetization as a function of applied field for a $[Ni(0.4)/Co(0.2)]_{10}$ multilayer film grown on a $[Nb(25)/Au(2.4)]_3/Nb(20)$ seed layer, measured both with the field in-plane and out-of-plane, demonstrating very strong PMA.

As the resilience of the PMA effect is crucial to the operation of the proposed device, the samples were also measured out to very high in-plane field to ensure that the out-of-plane characteristic would not be destroyed while initializing the in-plane Ni layer(s). Figure 5.5 shows one of these measurements out to a field of 4T. The diamagnetic background signal from the Si substrate has been subtracted from these data. Note that the PMA magnetization does not saturate until an in-plane field of over 1 Tesla (10,000 G) is applied, and that the remnant magnetization behavior (near zero field) is hardly altered from application of a field up to 4T. This means that the PMA layer is quite robust, and will likely not be destroyed during in-plane initialization.

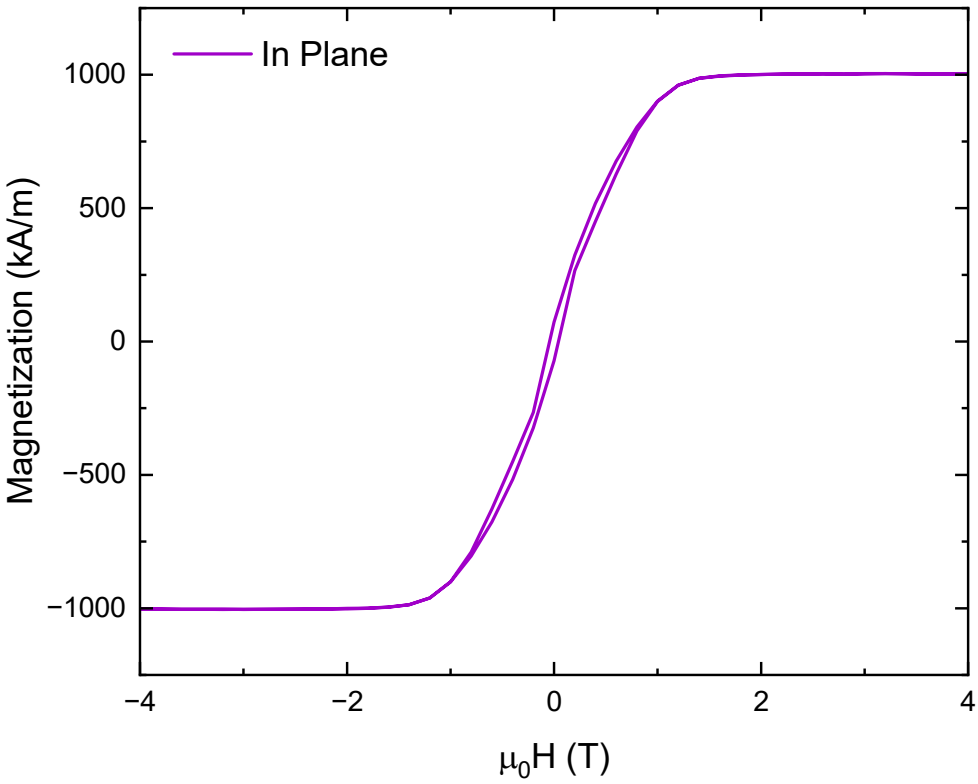

Figure 5.5 **High in-plane field data.** Magnetization as a function of applied field for a $[Ni(0.4)/Co(0.2)]_6$ multilayer film grown on a $[Nb(25)/Au(2.4)]_3/Nb(20)$ seed layer, measured with an in-plane field. Note that the diamagnetic signal from the Si substrate is very strong at such a high field and has been subtracted out.

5.3 Ni/NiFe/Ni Elliptical Arrays

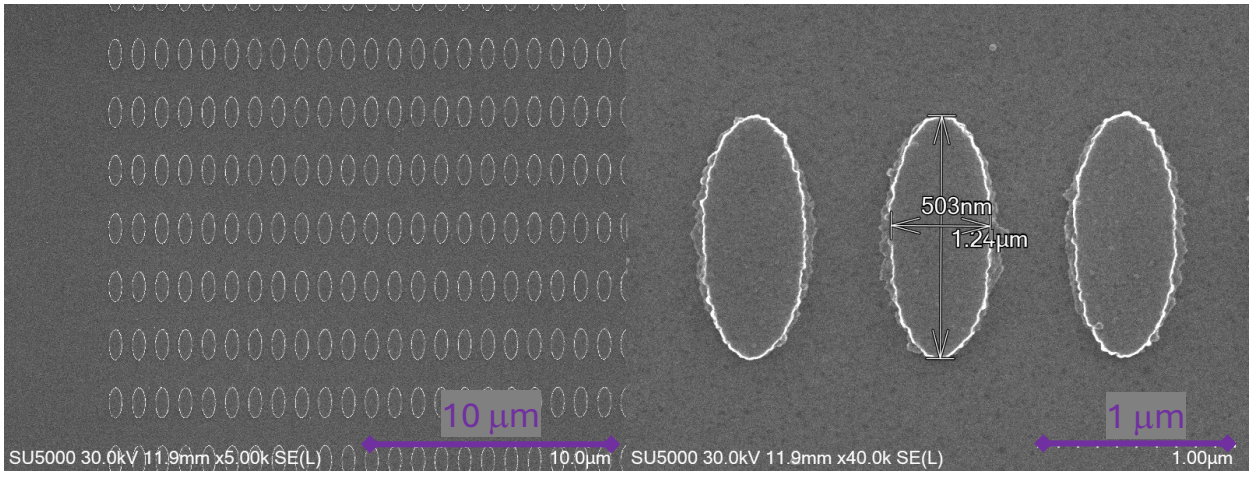

Figure 5.6 **Elliptical arrays.** SEM images of Ni/NiFe/Ni elliptical arrays at 5k and 40k magnification. The nominal size of each ellipse is 500 nm by 1.25 μm.

In a previous study on so-called 'Ni dusting' Ni/NiFe/Ni samples, the addition of very thin Ni layers of either 0.2 or 0.4 nm on either side showed increased supercurrent transmission through permalloy (NiFe) Josephson junctions [11]. Also in that study, magnetic characterization of sheet films was shown, but not for the very thin layers that would be required to be useful as a spin-mixing layer. Therefore, to characterize the magnetic behavior of elliptical pillars as would be used in JJ, very thin arrays of this system were investigated. Thin films were deposited as described in Chapter 3, then patterned with electron beam lithography in a very large array of approximately 8 million ellipses, each of size 500 nm by 1.25 μm (this mimics the size of the Josephson junctions). The process is similar to that for our Josephson junctions, but the pattern takes approximately 16 hours to write. The samples were then ion milled to define an array of magnetic pillars, as shown in Figure 5.6 and diced as described in Appendix B.3 for characterization in the SQUID magnetometer. Fig. 5.7 shows the magnetic hysteresis curves of a Ni(0.4)/NiFe(0.4)/Ni(0.4) sample measured parallel to and perpendicular to both the long axis of the ellipses and growth field. Note that, as discussed in Section 2.1.2 both the shape anisotropy of the ellipse and the magnetocrystaline anisotropy from the growth field should add to make the parallel axis the preferred axis of the magnetization. The opposite effect is observed in these data. So we conclude that the use of 'Ni dusting' permalloy as a short-range triplet generating layer does not appear to be promising, although our data showing the unexpected magnetization preferred-axis are notable in their own right.

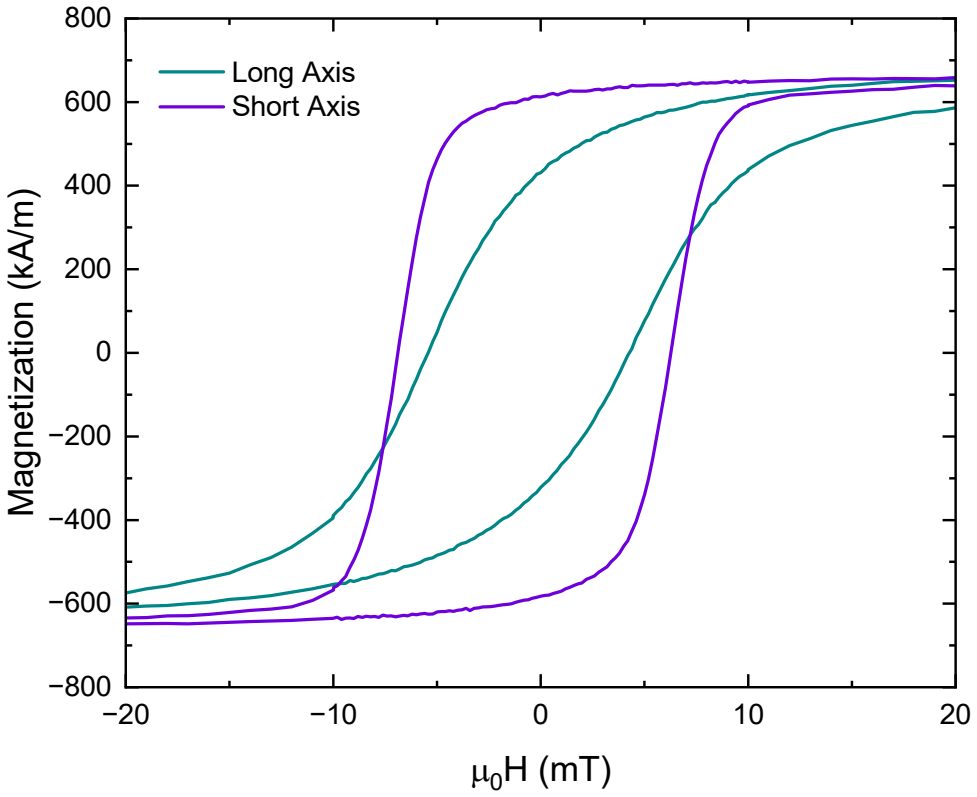

Figure 5.7 **Ni dusting magnetics.** Magnetization as a function of applied field for Ni(0.4)/NiFe(0.4)/Ni(0.4) array sample measured in parallel and perpendicular to the long axis and growth field of the ellipses. Surprisingly, the 'easy axis' preference of the magnetization is oriented along the short axis of the ellipse.

5.4 Spin-Triplet Josephson Junctions

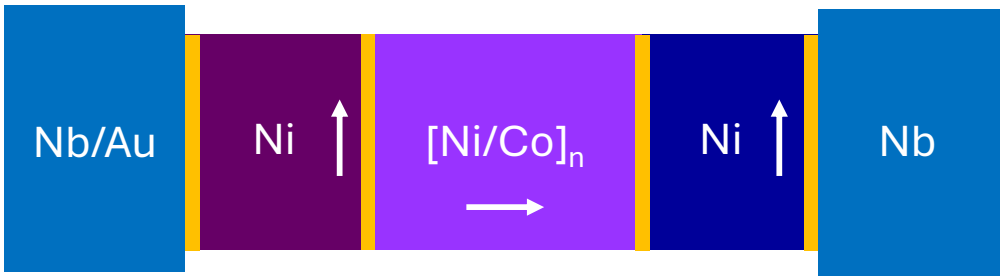

Figure 5.8 **Ni/Co triplet JJ.** Diagram of the trilayer spin-triplet Josephson junctions grown in this study, where the outer Ni layers serve as spin-mixers that generate the triplet supercurrent that is propagated through the central Ni/Co PMA layer.

As such a dramatic increase in the PMA effect was observed in sheet films of Ni/Co grown on Nb/Au base layers, we next probed the effect of such base layers on critical current transmission

in Josephson junctions. Samples of the structure S/N/F_1/N/F_2/N/F_3/S as shown in Figure 5.8 were measured with the central (F_2) layer comprised of $[Ni/Co]_n$ multilayers with and without a ruthenium coupling layer to create a synthetic antiferromagnet (SAF) [94]. Such SAF-containing samples were used in previous triplet work in order to cancel flux from the magnetizations of the PMA layers and were included for comparison.

Data from the transport measurements of the Josephson junctions grown on $[Nb(25)/Au(2.4)]_3$ base layers are shown in Figure 5.9. Peak critical current is plotted against central ferromagnet thickness. The very slow decay of the critical current with thickness for the non-SAF samples is the signature of long-range triplet supercurrent propagation. The SAF samples show a much steeper decay due to antiparallel magnetic layers having oppositely oriented majority spin bands therefore reducing the long-range triplet propagation. Additionally, when compared to previous results on Ni/Co junctions grown on Nb(150) base layers [20], there is a notable increase in the magnitude of the critical current, likely due to more robust PMA layer.

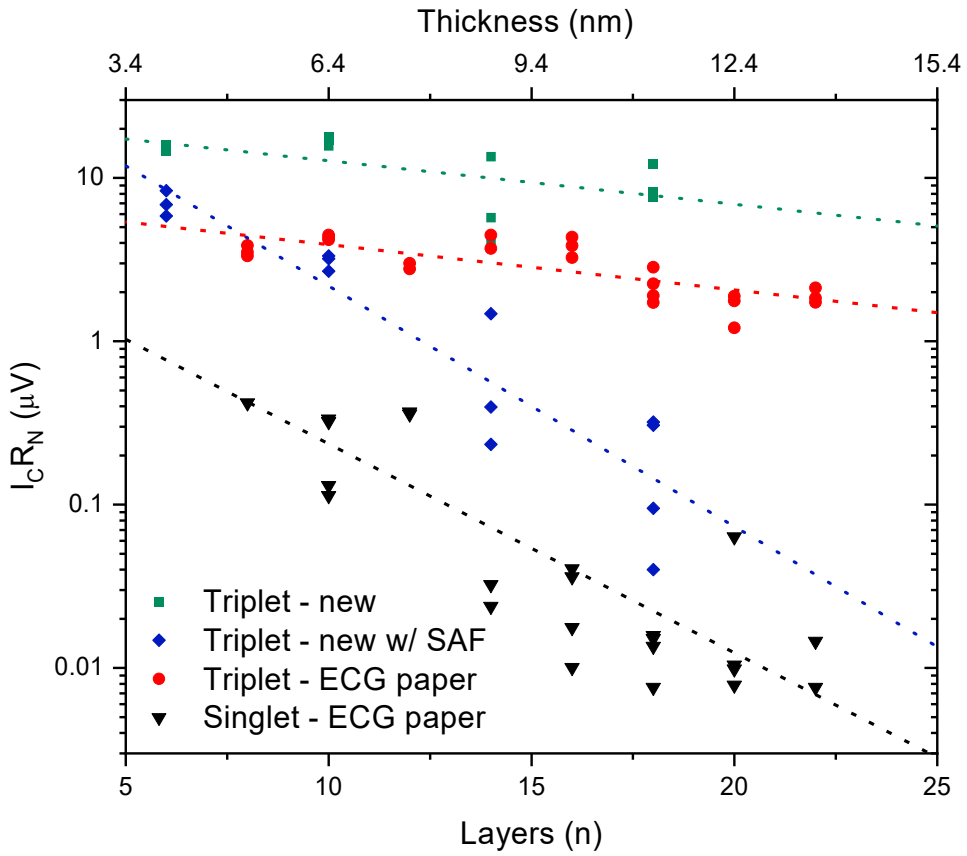

Figure 5.9 **Triplet critical current.** I_CR_N as a function of PMA $[Ni/Co]_n$ multilayer thickness with and without Ru coupling layer to create a SAF. The plot also compares new junctions containing $[Nb(25)/Au(2.4)]_3/Nb(20)$ base layers (green squares) to previously published [20] junctions containing Nb(150) base layers (red circles).

The observed increase in critical current and dramatically better PMA effect in Ni/Co samples grown on a Nb/Au multilayer base are notable and encouraging results toward the ultimate goal of a φ_0-junction device which relies on robust spin-triplet supercurrent propagation. Work carries forward in the following section using Nb/Au-seeded Ni/Co PMA central ferromagetic layers with alternate outer ferromagnetic layers.

5.5 Addition of Switchable Permalloy Layer

Figure 5.10 **Permalloy triplet JJ.** Diagram of the trilayer spin-triplet Josephson junctions as above, but with one of the Ni outer spin-mixers replaced with permalloy (NiFe), which is shown in red.

In order to characterize critical current transmission through a trilayer ferromagnetic stack that may actually provide phase-tunability, we next characterized junctions similar to those in the section above, but replacing either the top or bottom Ni layer with permalloy ($Ni_{81}Fe_{19}$), as shown in Figure 5.10. This is done because permalloy has a much lower coercivity than Ni (and PMA Ni/Co), therefore it can theoretically have its magnetization tuned without disturbing the magnetizations of the other layers, which is a key element of the proposed device. The previous assumption was that placing the permalloy layer on the bottom of a trilayer stack (instead of the top) would result in smoother deposition and therefore cleaner switching of its magnetization, but we decided to test the veracity of this as well. Junctions were fabricated in the same manner as above, again in three different junction areas per chip.

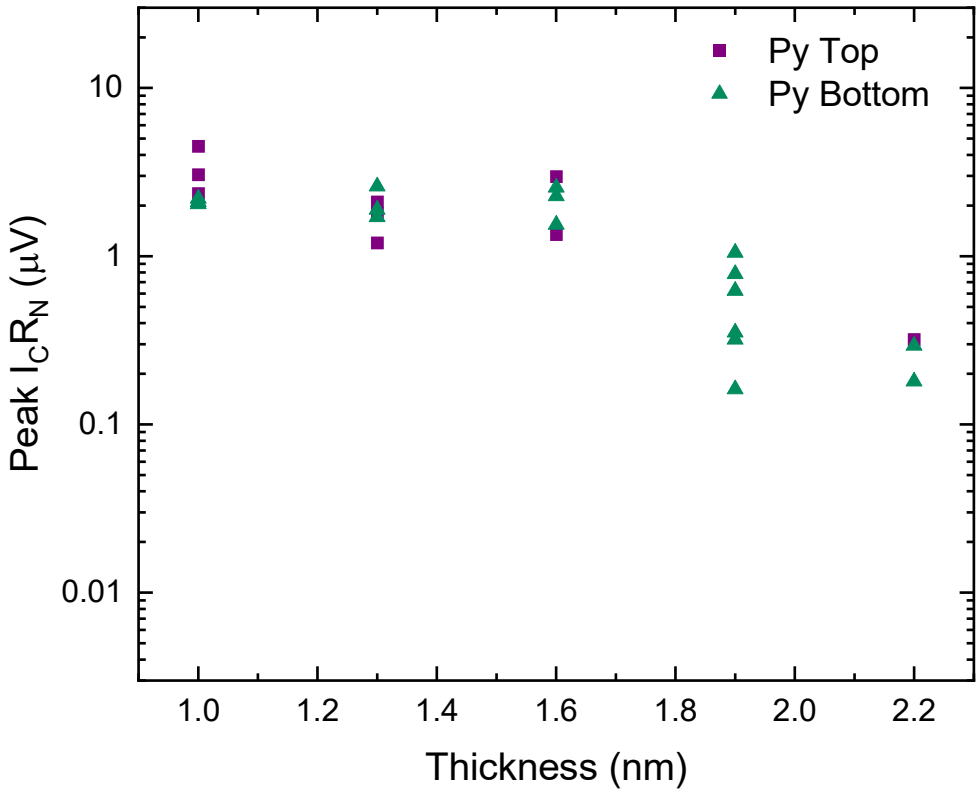

Figure 5.11 **Permalloy triplet $I_C R_N$.** Plot of peak critical current vs thickness of permalloy layer in nm.

Figure 5.11 shows the peak critical current plotted against the thickness of the permalloy layer. These data are consistent with previous results [18] and the prediction that the generation of short-range triplet is at a maximum at the same thickness when the singlet term goes to zero (the 0-π transition), which for permalloy is around 1.6 nm [11]. Note that the overall pair correlation function (with triplet and singlet components) decreases rapidly with thickness, which explains why the samples with very thin permalloy may have similar critical current as the sample at the 0-π transition, rather than demonstrating a clear peak at such thickness. There is also no discernible difference between samples with the permalloy on the top compared to those with permalloy on the bottom in terms of critical current transmission.

In order to further characterize these samples, some of them were not only measured with a varying magnetic field, but a varying initialization field, as shown in Figures 5.12-5.14. The magnetic field dependence of the critical current was taken from -500 to 500 Oe after initializing at

a negative field of 0, 1000, 1500, 2000, 2500, 3000, 3500, and 4000 Oe as displayed on the Z-axis (going into the page). This was done in order to determine the minimum field to properly train the (in-plane magnetization) Ni layers while not disturbing the central Ni/Co PMA layers. In the 'medium area' ($0.25\mu m^2$) sample shown in Figure 5.12, it appears that an initialization of 2000 Oe results in a decent Fraunhofer pattern, which begins to degrade with an initialization above 3000 Oe, likely from interfering with the perpendicular magnetization layer.

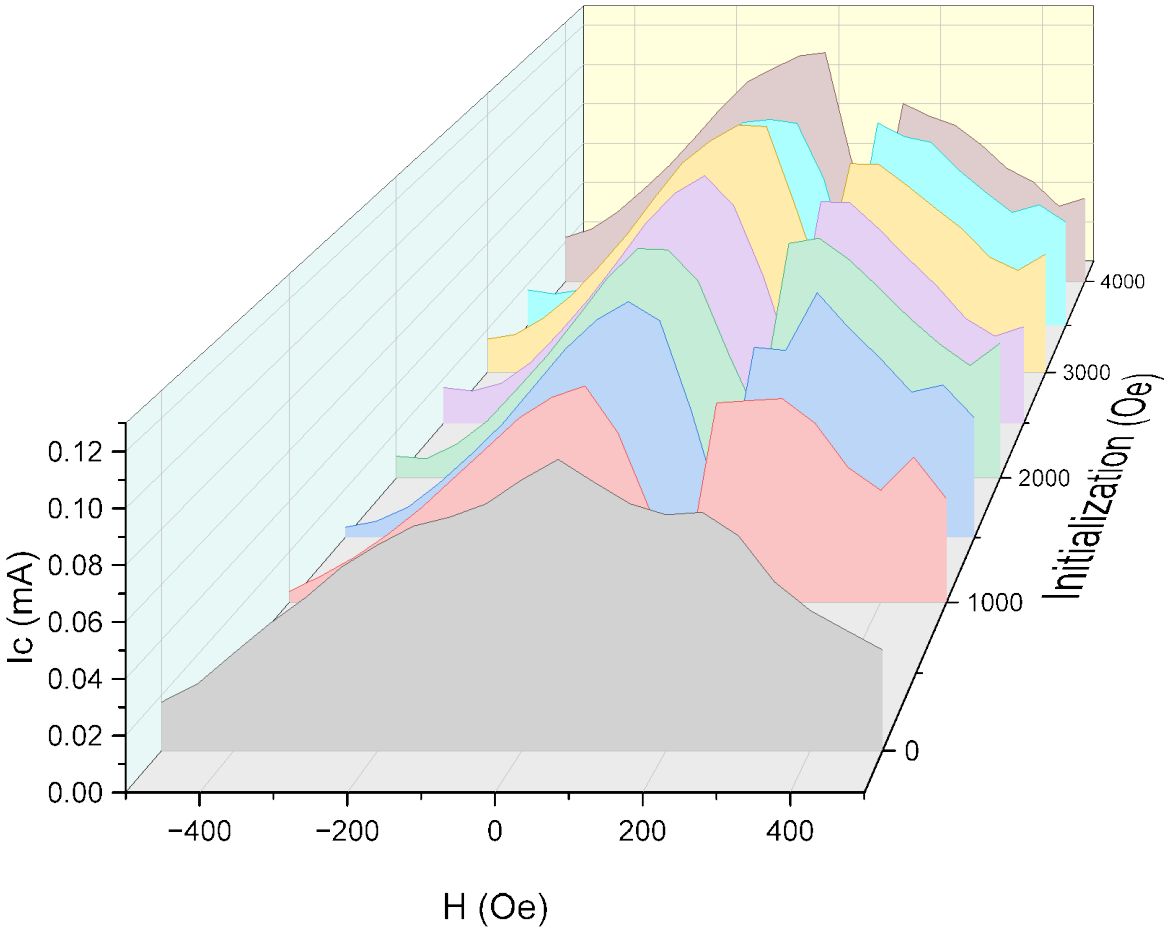

Figure 5.12 **Permalloy triplet initialization, medium area JJ.** Waterfall plot showing the field dependence of the critical current vs. the magnitude of the initialization field in Oe for the $0.25\mu m^2$ area sample. Note that the Fraunhofers improve up to about 2000 Oe, after which point there is no improvement by increasing the field.

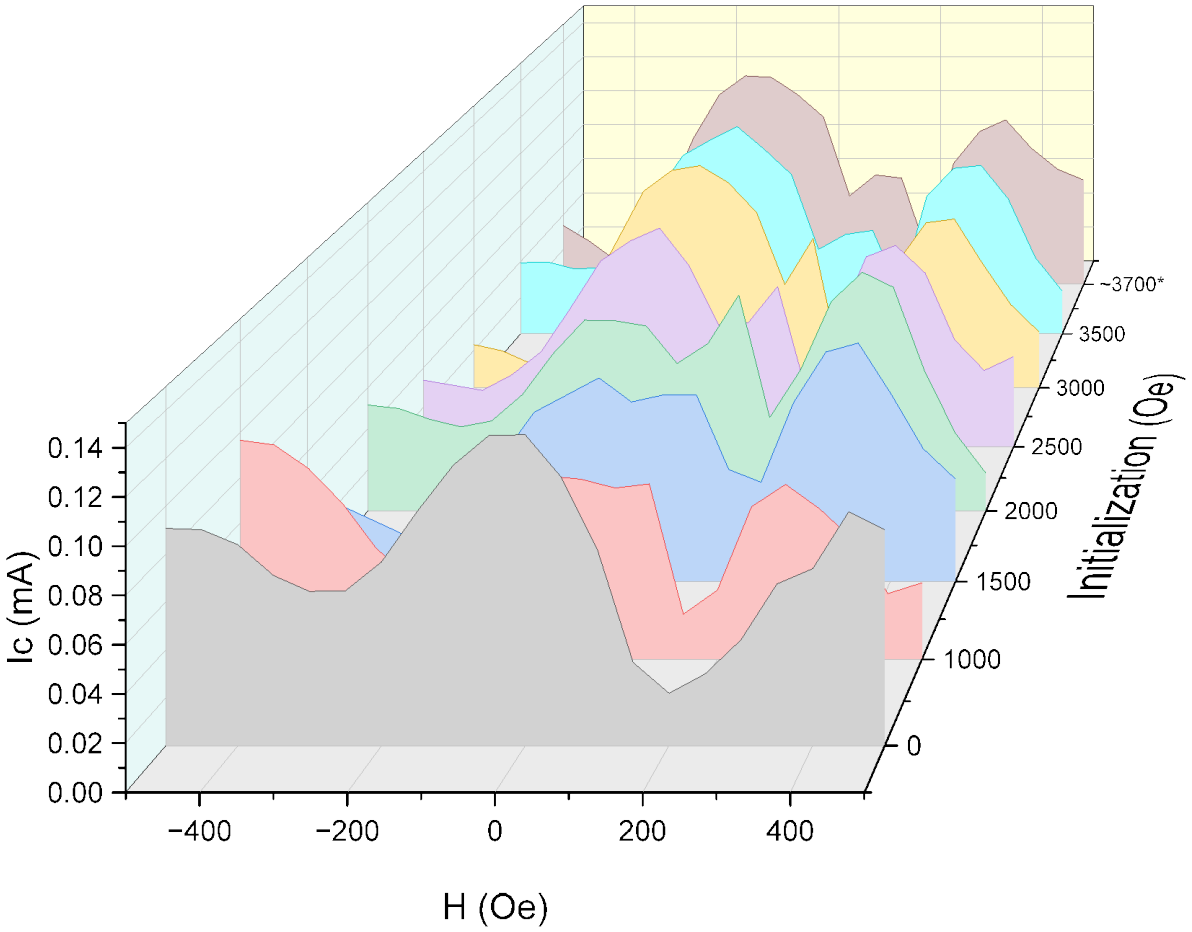

Figure 5.13 **Permalloy triplet initialization, large area JJ.** Waterfall plot showing the field dependence of the critical current vs. the magnitude of the initialization field in Oe for the $0.5\mu m^2$ area sample. Note that the Fraunhofers improve up to about 2500 Oe, after which point there is no improvement by increasing the field.

The data from the 'large area' ($0.5\mu m^2$) sample shown in Figure 5.13 and the 'small area' ($0.125\mu m^2$) sample shown in Figure 5.14 follow a similar trend, only with the Fraunhofer patterns improving in quality up to an initialization field of between 2500 and 3000 Oe. This may indicate that the intermediate junction size is in a sort of 'Goldilocks' zone exhibiting better switching behavior and Fraunhofer patterns than either the larger sample or the smaller sample. This intermediate size may be explored in future SQUID work.

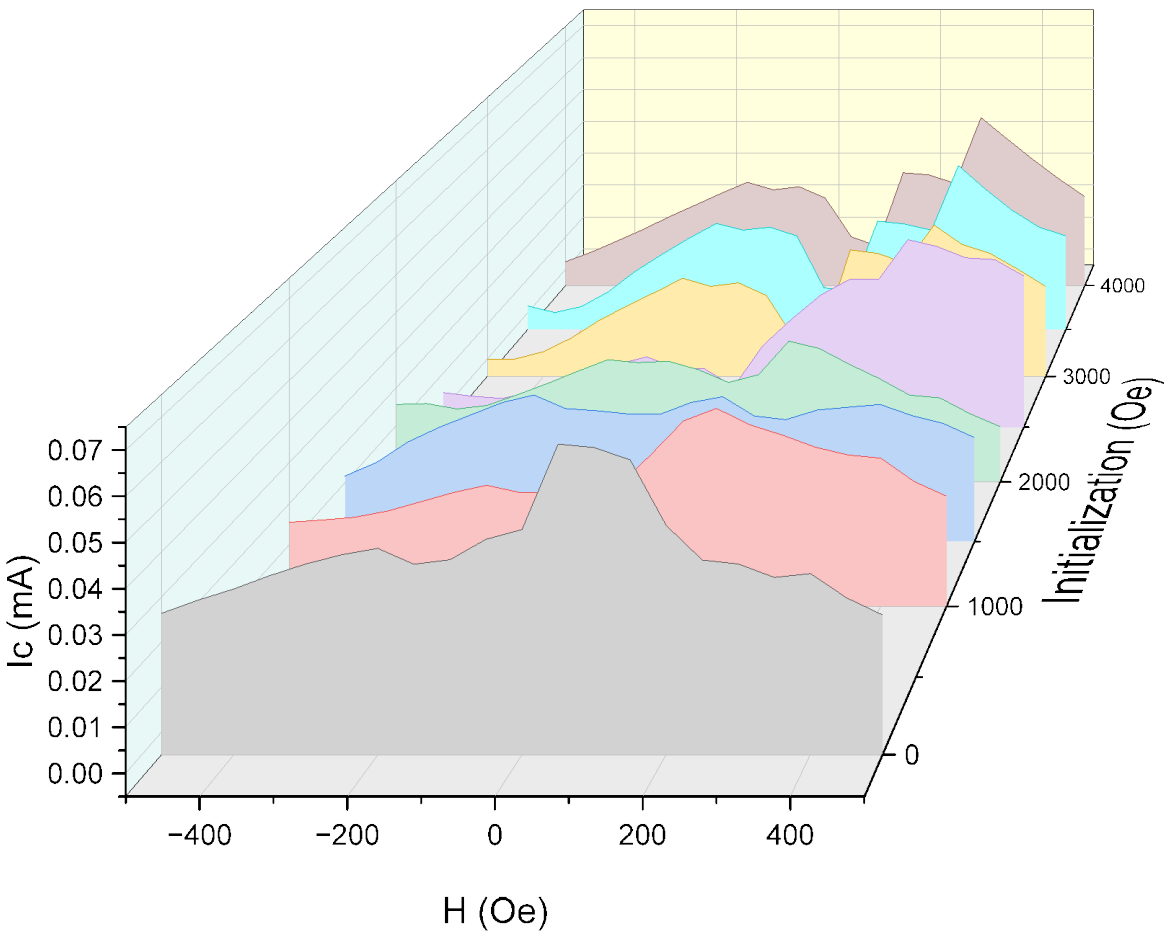

Figure 5.14 **Permalloy triplet initialization, small area JJ.** Waterfall plot showing the field dependence of the critical current vs. the magnitude of the initialization field in Oe for the $0.125\mu m^2$ area sample. Note that the Fraunhofers improve up to about 3000 Oe, after which point there is no improvement by increasing the field.

5.6 Ni/[Ni/Co]/NiFe SQUIDs

Informed by the data from the previous sections, a set of SQUID samples with an identical structure as shown in Figure 5.10 is being fabricated. The fabrication process is much the same as described in Chapter 3, only each step is a bit more finicky, and a different photolithography mask is used which allows for two EBL-defined junctions to be located in the same measurement loop, for phase-sensitive measurement. Figure 5.15 shows an optical microscope image of the bottom lead pattern used. In light of Alex Madden's SQUID study [9] comparing the SQUID design used in the original demonstration of phase control [6] to a new design intended to minimize inductance,

which showed it allows for more straight-forward fabrication and data analysis, we decided to use this ultra-low inductance SQUID design. A total of eight Josephson junctions comprising four SQUID devices can be fabricated per chip.

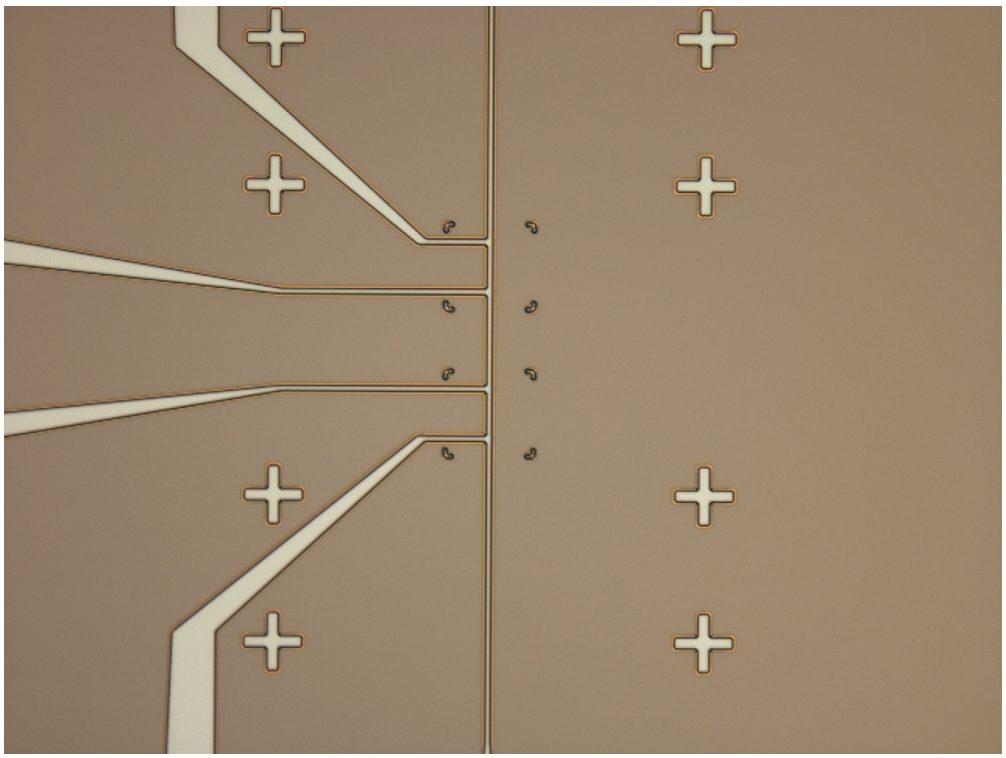

Figure 5.15 **SQUID bottom lead pattern.** Optical microscope image of the bottom lead photolithography pattern for the SQUID device samples.

This fabrication run will first test 0-π switching of these devices utilizing ellipses with different aspect ratios as in the studies referenced above. And, if successful, will next include samples with both a circular junction which can theoretically impart the mythical arbitrary phase drop in accordance with the magnetization direction with the application of a small field, and an elliptical junction that should maintain its magnetization direction along its long axis. As the testing of such a device requires a rotating magnetic field (or a rotating sample), these samples may be measured in a different system, such as that of Prof. Satchell's group at Texas State University. The data will not be taken in time to be included in this thesis, but may result in a future publication.

CHAPTER 6

CONCLUSIONS AND OUTLOOK

Bolstered by previous work in the group, the early work presented in this thesis is driven toward a direct industrial application of ferromagnetic Josephson junctions in the form of a JMRAM memory cell. I presented work investigating a method to make the fixed layer of the proposed device more robust by pinning its magnetization with an adjactent AF layer. We found that the AF material studied, NiMn, does indeed act as a pinning layer through the exchange bias effect in the very thin layers that would be needed in JMRAM application. However, the reduction of critical current from the addition of a NiMn layer observed in the data presented would seem to outweigh its benefit.

As the funding from the IARPA program ended shortly after this study, work evolved toward pursuit of other potential collaborations. Highlighted in Appendix A.3, I will show work toward the use of chiral molecules as the generators of spin-triplet supercurrent in ferromagnetic junctions. This work was done in collaboration with the Hebrew University of Jerusalem. Another project involving the investigation of intrinsic spin-triplet superconducting material NbRe was done in collaboration with the University of Salerno, which is not covered in this thesis. Appendix A also discusses a couple of side projects including preparing a study on NiFeCr for publication and optimizing the fabrication process.

Not finding a source of funding during my time as a graduate student ultimately allowed for flexibility in the direction of my thesis project. I chose to focus on the φ_0-junction discussed in Chapter 5, because, despite being quite ambitious for a research group with a single graduate student, it offered the most interesting work, and work well-suited for the strengths of our fabrication and measurement equipment. I discuss in this thesis my strides toward realization of this device, including methods to increase the detectable critical current and shore up the PMA magnetization of the propagation layer. I will also leave the group having fabricated devices that could result in notable operation and future publication.

Now, insofar as the completion of a Ph.D. thesis is the culmination of a singular, cohesive contribution to furthering the understanding and collective works of the human species, the efforts

contained herein could be seen as a failure. After all, where is the evidence of the namesake of this work, the fabled φ_0 junction? And it is true, I do not claim nor present such evidence.

However, in this thesis, I have presented several unique and interesting results, and gently nudged the boundary of known science, laying the groundwork for the next generation of researchers in the boutique field of superconductor/ferromagnet systems. As this thesis has demonstrated, during my time I fostered collaborations with many different research groups from around the world and built a skill set with applications far beyond the confines of the Biomedical and Physical Sciences building. These opportunities were thanks to the privilege of working at a phenomenal research institution with such deep intellectual and unique equipment resources. Therefore, my time in the graduate program at Michigan State University has been an unqualified success.

REFERENCES

[1] A. Buzdin, L. Bulaevskii, and S. Panyukov, "Critical-current oscillations as a function of the exchange field and thickness of the ferromagnetic metal (f) in an s-f-s Josephson junction," *Pis'Ma Zh. Eksp. Teor. Fiz.*, vol. 35, pp. 147–148, jan 1982.

[2] T. Kontos, M. Aprili, J. Lesueur, and X. Grison, "Inhomogeneous superconductivity induced in a ferromagnet by proximity effect," *Phys Rev Lett*, vol. 86, pp. 304–307, jan 2001.

[3] V. V. Ryazanov, V. A. Oboznov, A. Y. Rusanov, A. V. Veretennikov, A. A. Golubov, and J. Aarts, "Coupling of two superconductors through a ferromagnet: evidence for a π junction," *Phys Rev Lett*, vol. 86, pp. 2427–2430, mar 2001.

[4] T. Kontos, M. Aprili, J. Lesueur, F. GenÃłt, B. Stephanidis, and R. Boursier, "Josephson junction through a thin ferromagnetic layer: negative coupling," *Phys Rev Lett*, vol. 89, p. 137007, sep 2002.

[5] A. Y. Herr, Q. P. Herr, and O. Naaman, "Phase hysteretic magnetic Josephson junction memory cell," *US Patent*, pp. US 9,208,861 B2, dec 2015.

[6] E. C. Gingrich, B. M. Niedzielski, J. A. Glick, Y. Wang, D. L. Miller, R. Loloee, W. P. Pratt Jr, and N. O. Birge, "Controllable 0–π Josephson junctions containing a ferromagnetic spin valve," *Nat Phys*, vol. 12, pp. 564–567, mar 2016.

[7] I. M. Dayton, T. Sage, E. C. Gingrich, M. G. Loving, T. F. Ambrose, N. P. Siwak, S. Keebaugh, C. Kirby, D. L. Miller, A. Y. Herr, Q. P. Herr, and O. Naaman, "Experimental demonstration of a Josephson magnetic memory cell with a programmable π-junction," *IEEE Magn. Lett.*, vol. 9, pp. 1–5, 2018.

[8] J. A. Glick, V. Aguilar, A. B. Gougam, B. M. Niedzielski, E. C. Gingrich, R. Loloee, W. P. Pratt, and N. O. Birge, "Phase control in a spin-triplet SQUID," *Sci Adv*, vol. 4, p. eaat9457, jul 2018.

[9] A. E. Madden, J. C. Willard, R. Loloee, and N. O. Birge, "Phase controllable Josephson junctions for cryogenic memory," *Supercond. Sci. Technol.*, vol. 32, p. 015001, jan 2019.

[10] V. Aguilar, D. Korucu, J. A. Glick, R. Loloee, W. P. Pratt, and N. O. Birge, "Spin-polarized triplet supercurrent in Josephson junctions with perpendicular ferromagnetic layers," *Phys. Rev. B*, vol. 102, p. 024518, jul 2020.

[11] S. S. Mishra, R. M. Klaes, J. Willard, R. Loloee, and N. O. Birge, "Enhancement of supercurrent through ferromagnetic materials by interface engineering," *Phys. Rev. B*, vol. 106, p. 014519, jul 2022.

[12] S. S. Mishra, R. Loloee, and N. O. Birge, "Effect of interfaces on supercurrent through ferromagnetic materials," *IEEE Trans. Appl. Supercond.*, pp. 1–7, 2023.

[13] F. S. Bergeret, A. F. Volkov, and K. B. Efetov, "Long-range proximity effects in superconductor-ferromagnet structures," *Phys Rev Lett*, vol. 86, pp. 4096–4099, apr 2001.

[14] F. S. Bergeret, A. F. Volkov, and K. B. Efetov, "Manifestation of triplet superconductivity in superconductor-ferromagnet structures," *Phys. Rev. B*, vol. 68, p. 064513, aug 2003.

[15] T. S. Khaire, M. A. Khasawneh, W. P. Pratt, and N. O. Birge, "Observation of spin-triplet superconductivity in Co-based Josephson junctions," *Phys Rev Lett*, vol. 104, p. 137002, apr 2010.

[16] M. Houzet and A. I. Buzdin, "Long range triplet Josephson effect through a ferromagnetic trilayer," *Phys. Rev. B*, vol. 76, p. 060504, aug 2007.

[17] M. Eschrig, "Spin-polarized supercurrents for spintronics," *Phys Today*, vol. 64, no. 1, p. 43, 2011.

[18] M. A. Khasawneh, T. S. Khaire, C. Klose, W. P. Pratt Jr, and N. O. Birge, "Spin-triplet supercurrent in Co-based Josephson junctions," *Supercond. Sci. Technol.*, vol. 24, p. 024005, feb 2011.

[19] C. Klose, T. S. Khaire, Y. Wang, W. P. Pratt, N. O. Birge, B. J. McMorran, T. P. Ginley, J. A. Borchers, B. J. Kirby, B. B. Maranville, and J. Unguris, "Optimization of spin-triplet supercurrent in ferromagnetic Josephson junctions," *Phys Rev Lett*, vol. 108, p. 127002, mar 2012.

[20] E. C. Gingrich, P. Quarterman, Y. Wang, R. Loloee, W. P. Pratt, and N. O. Birge, "Spin-triplet supercurrent in Co/Ni multilayer Josephson junctions with perpendicular anisotropy," *Phys. Rev. B*, vol. 86, p. 224506, dec 2012.

[21] N. Satchell and N. O. Birge, "Supercurrent in ferromagnetic Josephson junctions with heavy metal interlayers," *Phys. Rev. B*, vol. 97, p. 214509, jun 2018.

[22] N. Satchell, R. Loloee, and N. O. Birge, "Supercurrent in ferromagnetic josephson junctions with heavy-metal interlayers. II. canted magnetization," *Phys. Rev. B*, vol. 99, p. 174519, may 2019.

[23] A. Buzdin, "Direct coupling between magnetism and superconducting current in the Josephson φ_0 junction," *Phys Rev Lett*, vol. 101, p. 107005, sep 2008.

[24] M. A. Silaev, I. V. Tokatly, and F. S. Bergeret, "Anomalous current in diffusive ferromagnetic Josephson junctions," *Phys. Rev. B*, vol. 95, p. 184508, may 2017.

[25] V. Aguilar, *Ferromagnetic Josephson Junctions with Both In and Out of Plane Anisotropy*. Doctoral Thesis, Michigan State University, 2021.

[26] R. M. Klaes, R. Loloee, and N. O. Birge, "Critical current decay in Josephson junctions containing antiferromagnetic NiMn," *IEEE Trans. Appl. Supercond.*, 2023.

[27] J. M. D. Coey and S. S. Parkin, eds., *History of magnetism and basic concepts*. Cham, Switzerland: Springer International Publishing, 2021.

[28] F. Hund, "Linienspektren und periodisches system der elemente," *Nature*, vol. 120, pp. 580–580, oct 1927.

[29] E. C. Stoner, "Collective electron ferromagnetism," *Proc. R. Soc. Lond. A*, vol. 165, pp. 372–414, apr 1938.

[30] N. A. Spaldin, *Magnetic materials: fundamentals and applications*. Cambridge, UK: University Printing House, 2nd ed., 2011.

[31] D. C. Jiles, *Introduction to Magnetism and Magnetic Materials, Second Edition*. CRC Press, 2, revised ed., 1998.

[32] H. K. Onnes, "The superconductivity of mercury," *Comm. Phys. Lab. Univ., Leiden*, pp. 122–124, 1911.

[33] W. Meissner and R. Ochsenfeld, "Ein neuer effekt bei eintritt der supraleitfähigkeit," *Naturwissenschaften*, vol. 21, no. 44, pp. 787–788, 1933.

[34] F. London and H. London, "The electromagnetic equations of the supraconductor," *Proc. R. Soc. Lond. A*, vol. 149, no. 866, pp. 71–88, 1935.

[35] V. L. Ginzburg and L. D. Landau, "On the theory of superconductivity," *Zh. Eksp. Teor. Fiz.*, vol. 20, pp. 1064–1082, 1950.

[36] J. Bardeen, L. N. Cooper, and J. R. Schrieffer, "Theory of superconductivity," *Phys. Rev.*, vol. 108, pp. 1175–1204, dec 1957.

[37] J. Bardeen, L. N. Cooper, and J. R. Schrieffer, "Microscopic theory of superconductivity," *Phys. Rev.*, vol. 106, pp. 162–164, apr 1957.

[38] B. Josephson, "Possible new effects in superconductive tunnelling," *Physics Letters*, vol. 1, pp. 251–253, jul 1962.

[39] W. C. Stewart, "Current-voltage characteristics of Josephson junctions," *App. Phys. Lett.*, vol. 12, no. 8, pp. 277–280, 1968.

[40] D. E. McCumber, "Effect of ac impedance on dc voltage-current characteristics of superconductor weak-link junctions," *J. App. Phys.*, vol. 39, no. 7, pp. 3113–3118, 1968.

[41] J. R. Kirtley, *Magnetic field effects in Josephson junctions*, vol. 286 of *Springer series in materials science*. Cham: Springer International Publishing, 2019.

[42] H. Lüth, *Collective Phenomena at Interfaces: Superconductivity and Ferromagnetism*. Springer, 2015.

[43] A. F. Andreev, "The thermal conductivity of the intermediate state in superconductors," *Sov. Phys. JETP.*, vol. 46, no. 5, pp. 1823–1828, 1964.

[44] L. Bulaevskii, V. Kuzii, and A. Sobyanin, "On possibility of the spontaneous magnetic flux in a Josephson junction containing magnetic impurities," *Solid State Commun*, vol. 25, pp. 1053–1057, mar 1978.

[45] N. O. Birge and N. Satchell, "Ferromagnetic materials for Josephson π junctions," *APL Mater*, vol. 12, apr 2024.

[46] J. A. Glick, *Ferromagnetic Josephson Junctions Carrying Spin-Triplet Supercurrent For Cryogenic Memory*. Doctoral Thesis, Michigan State University, 2017.

[47] R. C. Jaklevic, J. Lambe, A. H. Silver, and J. E. Mercereau, "Quantum interference effects in josephson tunneling," *Phys Rev Lett*, vol. 12, pp. 159–160, feb 1964.

[48] B. S. Deaver and W. M. Fairbank, "Experimental evidence for quantized flux in superconducting cylinders," *Phys. Rev. Lett*, vol. 7, pp. 43–46, jul 1961.

[49] R. Doll and M. Näbauer, "Experimental proof of magnetic flux quantization in a superconducting ring," *Phys. Rev. Lett*, vol. 7, pp. 51–52, jul 1961.

[50] F. S. Bergeret, A. F. Volkov, and K. B. Efetov, "Josephson current in superconductor-ferromagnet structures with a nonhomogeneous magnetization," *Phys. Rev. B*, vol. 64, p. 134506, sep 2001.

[51] N. O. Birge, "Spin-triplet supercurrents in Josephson junctions containing strong ferromagnetic materials," *Philos Transact A Math Phys Eng Sci*, vol. 376, aug 2018.

[52] A. Buzdin and A. E. Koshelev, "Periodic alternating 0- and π-junction structures as realization of φ Josephson junctions," *Phys. Rev. B*, vol. 67, p. 220504, jun 2003.

[53] E. Goldobin, D. Koelle, R. Kleiner, and A. Buzdin, "Josephson junctions with second harmonic in the current-phase relation: Properties of φ junctions," *Physical Review B - Condensed Matter and Materials Physics*, vol. 76, p. 224523, dec 2007.

[54] N. G. Pugach, E. Goldobin, R. Kleiner, and D. Koelle, "Method for reliable realization of a φ Josephson junction," *Physical Review B - Condensed Matter and Materials Physics*, vol. 81, p. 104513, mar 2010.

[55] H. Sickinger, A. Lipman, M. Weides, R. G. Mints, H. Kohlstedt, D. Koelle, R. Kleiner, and E. Goldobin, "Experimental evidence of a φ Josephson junction," *Phys Rev Lett*, vol. 109, p. 107002, sep 2012.

[56] S. V. Bakurskiy, N. V. Klenov, T. Y. Karminskaya, M. Y. Kupriyanov, and A. A. Golubov, "Josephson φ-junctions based on structures with complex normal/ferromagnet bilayer," *Supercond. Sci. Technol.*, vol. 26, p. 015005, jan 2013.

[57] J. Xu, J. Miller, and C. Ting, "π-vortex state in a long 0-π Josephson junction," *Phys Rev, B Condens Matter*, vol. 51, pp. 11958–11961, may 1995.

[58] R. G. Mints, "Self-generated flux in Josephson junctions with alternating critical current density," *Phys. Rev. B*, vol. 57, pp. R3221–R3224, feb 1998.

[59] E. Goldobin, D. Koelle, and R. Kleiner, "Semifluxons in long Josephson-junctions," *Phys. Rev. B*, vol. 66, p. 100508, sep 2002.

[60] V. Braude and Y. V. Nazarov, "Fully developed triplet proximity effect," *Phys Rev Lett*, vol. 98, p. 077003, feb 2007.

[61] A. V. Galaktionov, M. S. Kalenkov, and A. D. Zaikin, "Josephson current and andreev states in superconductor-half metal-superconductor heterostructures," *Phys. Rev. B*, vol. 77, p. 094520, mar 2008.

[62] R. Grein, M. Eschrig, G. Metalidis, and G. Schön, "Spin-dependent Cooper pair phase and pure spin supercurrents in strongly polarized ferromagnets," *Phys Rev Lett*, vol. 102, p. 227005, jun 2009.

[63] I. Margaris, V. Paltoglou, and N. Flytzanis, "Zero phase difference supercurrent in ferromagnetic Josephson junctions," *J Phys Condens Matter*, vol. 22, p. 445701, nov 2010.

[64] J.-F. Liu and K. S. Chan, "Anomalous Josephson current through a ferromagnetic trilayer junction," *Phys. Rev. B*, vol. 82, p. 184533, nov 2010.

[65] M. Alidoust and J. Linder, "φ-state and inverted Fraunhofer pattern in nonaligned Josephson junctions," *Phys. Rev. B*, vol. 87, p. 060503, feb 2013.

[66] I. Kulagina and J. Linder, "Spin supercurrent, magnetization dynamics, and φ-state in spin-textured Josephson junctions," *Physical Review B - Condensed Matter and Materials Physics*, vol. 90, p. 054504, aug 2014.

[67] A. Lipman, R. G. Mints, R. Kleiner, D. Koelle, and E. Goldobin, "Josephson junctions with tunable current-phase relation," *Physical Review B - Condensed Matter and Materials Physics*, vol. 90, p. 184502, nov 2014.

[68] F. Konschelle, I. V. Tokatly, and F. S. Bergeret, "Theory of the spin-galvanic effect and the anomalous phase shift in superconductors and Josephson junctions with intrinsic spin-orbit coupling," *Phys. Rev. B*, vol. 92, p. 125443, sep 2015.

[69] S. V. Bakurskiy, V. I. Filippov, V. I. Ruzhickiy, N. V. Klenov, I. I. Soloviev, M. Y. Kupriyanov, and A. A. Golubov, "Current-phase relations in SIsFS junctions in the vicinity of 0- π transition," *Physical Review B*, vol. 95, p. 094522, mar 2017.

[70] S. Pal and C. Benjamin, "Quantized Josephson phase battery," *EPL*, vol. 126, p. 57002, jul 2019.

[71] Y. M. Shukrinov, "Anomalous Josephson effect," *Phys.-Usp.*, vol. 65, pp. 317–354, apr 2022.

[72] I. V. Bobkova, A. M. Bobkov, and M. A. Silaev, "Magnetoelectric effects in Josephson junctions," *J Phys Condens Matter*, vol. 34, jun 2022.

[73] D. B. Szombati, S. Nadj-Perge, D. Car, S. R. Plissard, E. P. A. M. Bakkers, and L. P. Kouwenhoven, "Josephson φ_0-junction in nanowire quantum dots," *Nat Phys*, vol. 12, pp. 568–572, may 2016.

[74] A. Murani, A. Kasumov, S. Sengupta, Y. A. Kasumov, V. T. Volkov, I. I. Khodos, F. Brisset, R. Delagrange, A. Chepelianskii, R. Deblock, H. Bouchiat, and S. Guéron, "Ballistic edge states in bismuth nanowires revealed by SQUID interferometry," *Nat Commun*, vol. 8, p. 15941, jul 2017.

[75] A. Assouline, C. Feuillet-Palma, N. Bergeal, T. Zhang, A. Mottaghizadeh, A. Zimmers, E. Lhuillier, M. Eddrie, P. Atkinson, M. Aprili, and H. Aubin, "Spin-orbit induced phase-shift in Bi_2Se_3 Josephson junctions," *Nat Commun*, vol. 10, p. 126, jan 2019.

[76] H. Ren, F. Pientka, S. Hart, A. T. Pierce, M. Kosowsky, L. Lunczer, R. Schlereth, B. Scharf, E. M. Hankiewicz, L. W. Molenkamp, B. I. Halperin, and A. Yacoby, "Topological superconductivity in a phase-controlled Josephson junction," *Nature*, vol. 569, pp. 93–98, may 2019.

[77] W. Mayer, M. C. Dartiailh, J. Yuan, K. S. Wickramasinghe, E. Rossi, and J. Shabani, "Gate controlled anomalous phase shift in Al/InAs Josephson junctions," *Nat Commun*, vol. 11, p. 212, jan 2020.

[78] E. Strambini, A. Iorio, O. Durante, R. Citro, C. Sanz-Fernández, C. Guarcello, I. V. Tokatly, A. Braggio, M. Rocci, N. Ligato, V. Zannier, L. Sorba, F. S. Bergeret, and F. Giazotto, "A Josephson phase battery," *Nat Nanotechnol*, vol. 15, pp. 656–660, aug 2020.

[79] H. Idzuchi, F. Pientka, K.-F. Huang, K. Harada, Ö. Gül, Y. J. Shin, L. T. Nguyen, N. H. Jo, D. Shindo, R. J. Cava, P. C. Canfield, and P. Kim, "Unconventional supercurrent phase in Ising superconductor Josephson junction with atomically thin magnetic insulator," *Nat Commun*, vol. 12, p. 5332, sep 2021.

[80] C. Baumgartner, L. Fuchs, A. Costa, J. Picó-Cortés, S. Reinhardt, S. Gronin, G. C. Gardner, T. Lindemann, M. J. Manfra, P. E. Faria Junior, D. Kochan, J. Fabian, N. Paradiso, and C. Strunk, "Effect of Rashba and Dresselhaus spin-orbit coupling on supercurrent rectification and magnetochiral anisotropy of ballistic Josephson junctions," *J Phys Condens Matter*, vol. 34, feb 2022.

[81] D. L. Edmunds, W. P. Pratt, and J. A. Rowlands, "0.1 ppm four-terminal resistance bridge for use with a dilution refrigerator," *Rev. Sci. Instrum.*, vol. 51, pp. 1516–1522, nov 1980.

[82] R. C. O'Handley, *Modern magnetic materials: principles and applications*. Wiley, 2000.

[83] L. Savtchenko, B. N. Engel, N. D. Rizzo, M. F. Deherrera, and J. A. Janesky, "Method of writing to scalable magnetoresistance random access memory element," *US Patent*, pp. US 6,545,906 B1, apr 2003.

[84] J. Slaughter, "Materials for magnetoresistive random access memory," *Annu Rev Mater Res*, vol. 39, pp. 277–296, aug 2009.

[85] D. Apalkov, B. Dieny, and J. M. Slaughter, "Magnetoresistive random access memory," *Proc. IEEE*, vol. 104, pp. 1796–1830, oct 2016.

[86] M. Baibich, J. Broto, A. Fert, F. Nguyen Van Dau, F. Petroff, P. Etienne, G. Creuzet, A. Friederich, and J. Chazelas, "Giant magnetoresistance of (001)Fe/(001)Cr magnetic superlattices," *Phys Rev Lett*, vol. 61, pp. 2472–2475, nov 1988.

[87] B. M. Niedzielski, *Phase Sensative Measurements of Ferromagnetic Josephson Junctions for Cryogenic Memory Applications*. Doctoral Thesis, Michigan State University, jul 2017.

[88] B. Baek, M. L. Schneider, M. R. Pufall, and W. H. Rippard, "Anomalous supercurrent modulation in Josephson junctions with Ni-based barriers," *IEEE Trans. Appl. Supercond.*, vol. 28, pp. 1–5, oct 2018.

[89] A. Barone and G. Paternò, *Physics and applications of the Josephson effect*. Wiley, jul 1982.

[90] C. Bell, E. J. Tarte, G. Burnell, C. W. Leung, D.-J. Kang, and M. G. Blamire, "Proximity and Josephson effects in superconductor/antiferromagnetic heterostructures," *Phys. Rev. B*, vol. 68, p. 144517, oct 2003.

[91] K.-R. Jeon, B. K. Hazra, K. Cho, A. Chakraborty, J.-C. Jeon, H. Han, H. L. Meyerheim, T. Kontos, and S. S. P. Parkin, "Long-range supercurrents through a chiral non-collinear antiferromagnet in lateral Josephson junctions," *Nat Mater*, vol. 20, pp. 1358–1363, oct 2021.

[92] J. A. Glick, S. Edwards, D. Korucu, V. Aguilar, B. M. Niedzielski, R. Loloee, W. P. Pratt, N. O. Birge, P. G. Kotula, and N. Missert, "Spin-triplet supercurrent in Josephson junctions containing a synthetic antiferromagnet with perpendicular magnetic anisotropy," *Phys. Rev. B*, vol. 96, p. 224515, dec 2017.

[93] R. M. Klaes and N. O. Birge, "Spin-triplet supercurrent optimization in ferromagnetic Josephson junctions," *2024 IEEE International Magnetic Conference - Short papers*, pp. 1–2, 2024.

[94] S. S. P. Parkin, N. More, and K. P. Roche, "Oscillations in exchange coupling and magnetoresistance in metallic superlattice structures: Co/Ru, Co/Cr, and Fe/Cr," *Phys Rev Lett*, vol. 64, pp. 2304–2307, may 1990.

[95] B. M. Niedzielski, S. G. Diesch, E. C. Gingrich, Y. Wang, R. Loloee, W. P. Pratt, and N. O. Birge, "Use of Pd-Fe and Ni-Fe-Nb as soft magnetic layers in ferromagnetic Josephson junctions for nonvolatile cryogenic memory," *IEEE Trans. Appl. Supercond.*, vol. 24, pp. 1–7, aug 2014.

[96] B. M. Niedzielski, E. C. Gingrich, R. Loloee, W. P. Pratt, and N. O. Birge, "S/F/S Josephson junctions with single-domain ferromagnets for memory applications," *Supercond. Sci. Technol.*, vol. 28, p. 085012, aug 2015.

[97] J. A. Glick, M. A. Khasawneh, B. M. Niedzielski, R. Loloee, W. P. Pratt, N. O. Birge, E. C. Gingrich, P. G. Kotula, and N. Missert, "Critical current oscillations of elliptical Josephson junctions with single-domain ferromagnetic layers," *J Appl Phys*, vol. 122, p. 133906, oct 2017.

[98] Z. Niu, "A spin triplet supercurrent in half metal ferromagnet/superconductor junctions with the interfacial Rashba spin-orbit coupling," *Appl. Phys. Lett*, vol. 101, p. 062601, aug 2012.

[99] F. S. Bergeret and I. V. Tokatly, "Singlet-triplet conversion and the long-range proximity effect in superconductor-ferromagnet structures with generic spin dependent fields," *Phys Rev Lett*, vol. 110, p. 117003, mar 2013.

[100] F. S. Bergeret and I. V. Tokatly, "Spin-orbit coupling as a source of long-range triplet proximity effect in superconductor-ferromagnet hybrid structures," *Phys. Rev. B*, vol. 89, p. 134517, apr 2014.

[101] F. Konschelle, "Transport equations for superconductors in the presence of spin interaction," *Eur. Phys. J. B*, vol. 87, p. 119, may 2014.

[102] S. H. Jacobsen, J. A. Ouassou, and J. Linder, "Critical temperature and tunneling spectroscopy of superconductor-ferromagnet hybrids with intrinsic Rashba-Dresselhaus spin-orbit coupling," *Phys. Rev. B*, vol. 92, p. 024510, jul 2015.

[103] M. Alidoust and K. Halterman, "Spontaneous edge accumulation of spin currents in finite-size two-dimensional diffusive spin-orbit coupled SFS heterostructures," *New J Phys*, vol. 17, p. 033001, mar 2015.

[104] M. Alidoust and K. Halterman, "Long-range spin-triplet correlations and edge spin currents in diffusive spin-orbit coupled SNS hybrids with a single spin-active interface," *J Phys Condens Matter*, vol. 27, p. 235301, jun 2015.

[105] S. H. Jacobsen, I. Kulagina, and J. Linder, "Controlling superconducting spin flow with spin-flip immunity using a single homogeneous ferromagnet," *Sci Rep*, vol. 6, p. 23926, apr 2016.

[106] R. Naaman and D. H. Waldeck, "Chiral-induced spin selectivity effect," *J Phys Chem Lett*, vol. 3, pp. 2178–2187, aug 2012.

[107] R. Naaman, Y. Paltiel, and D. H. Waldeck, "Chiral molecules and the electron spin," *Nat Rev Chem*, vol. 3, pp. 250–260, apr 2019.

[108] R. Naaman, Y. Paltiel, and D. H. Waldeck, "Chiral molecules and the spin selectivity effect," *J Phys Chem Lett*, vol. 11, pp. 3660–3666, may 2020.

[109] R. Naaman, Y. Paltiel, and D. H. Waldeck, "Chiral induced spin selectivity gives a new twist on spin-control in chemistry," *Acc Chem Res*, oct 2020.

[110] B. P. Bloom, Y. Paltiel, R. Naaman, and D. H. Waldeck, "Chiral induced spin selectivity," *Chem Rev*, vol. 124, pp. 1950–1991, feb 2024.

[111] A. K. Chauhan, P. Jha, D. K. Aswal, and J. V. Yakhmi, "Organic devices: fabrication, applications, and challenges," *Journal of Elec Materi*, vol. 51, pp. 447–485, feb 2022.

[112] H. Al-Bustami, S. Khaldi, O. Shoseyov, S. Yochelis, K. Killi, I. Berg, E. Gross, Y. Paltiel, and R. Yerushalmi, "Atomic and molecular layer deposition of chiral thin films showing up to 99% spin selective transport," *Nano Lett*, vol. 22, pp. 5022–5028, jun 2022.

APPENDIX A

ADDITIONAL WORK

A.1 NiFeCr Study

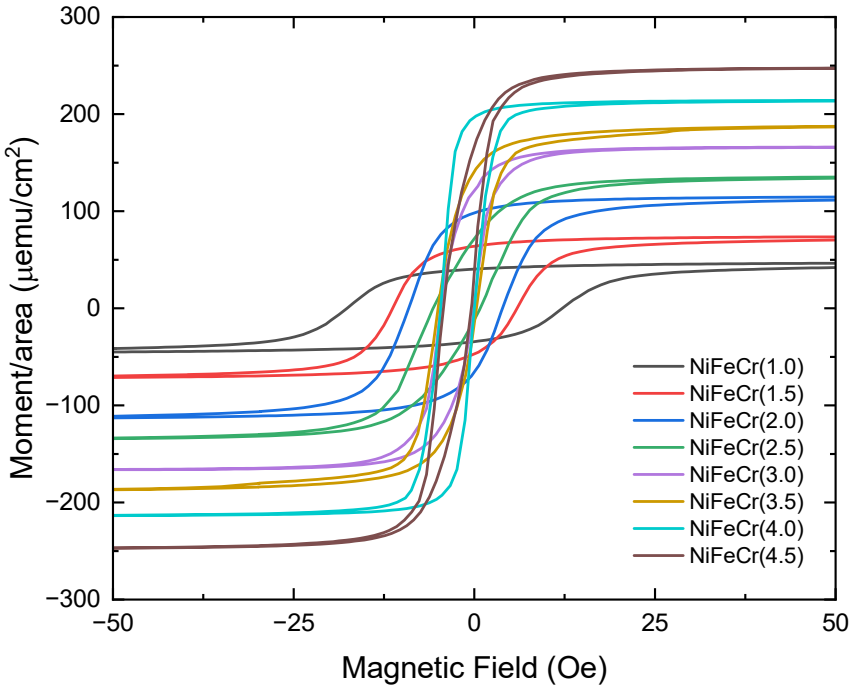

Figure A.1 **NiFeCr magnetics.** Magnetic hysteresis curves of $Ni_{73}Fe_{18}Cr_9$ films of thicknesses in nm as labeled.

Relating back to the superconducting memory cell project mentioned in Chapter 4, many other materials were investigated for use in the free layer by Norman's group such as Pd-Fe [95], Ni-Fe-Mo [96], and Ni-Fe-Co [97]. Adding to this list, another particular material was an alloy of nickel, iron, and chromium referred to as 'chrome-doped permalloy'. The idea was to lower the switching energy by reducing the magnetization, as permalloy ($Ni_{80}Fe_{20}$) has a rather large magnetization of about 900 emu/cm^3 [82]. Josephson junctions containing this material were characterized by my former colleague Josh Willard, and the bulk of the data will appear in an upcoming publication in the Journal of Applied Physics on which I am a coauthor. But I will mention a small study I performed here to characterize sheet films of the material.

Samples of the structure Nb(5)/Cu(2)/$Ni_{73}Fe_{18}Cr_9$(x)/Cu(2)/Nb(5) were fabricated on Si sub-

strates by sputtering deposition as described in Section 3.4 with x from 1.0 to 4.5 nm in steps of 0.5 nm. The samples were then quartered for measurement in the SQUID-VSM magnetometer. The results are shown in Figure A.1. As the moments have been normalized by the areas of the chips as measured by an optical microscope, the differences in saturation moment/area (as read by the y-intercepts) are due to the increasing thicknesses of the samples. The coercivity (as read by the x-intercepts) have an inverse relation to thickness as thinner samples are more resistive to reorientation.

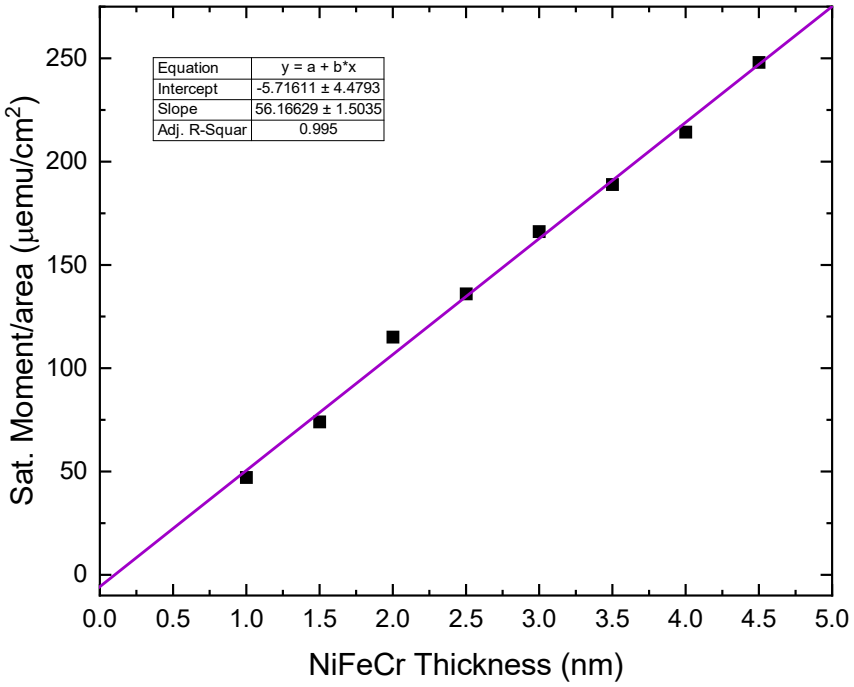

Figure A.2 **Saturation magnetization.** Saturation moment/area vs. thickness of $Ni_{73}Fe_{18}Cr_9$ films.

The saturation magnetization of $Ni_{73}Fe_{18}Cr_9$ can be read off of the linear fit to the saturation moment/area vs. thickness shown in Figure A.2. The slope is in μemu/(cm^2*nm) which translates with a factor of ten to emu/cm^3 which gives a saturation magnetization of 560 ± 15 emu/cm^2 at 10K. This is notably lower than permalloy's by about a third.

Also as a part of this study and in preparation for publication, the resistivities of permalloy and chrome-doped permalloy were measured, as well as CoGd for another upcoming publciation. Samples were sputter deposited in duplicate in thicknesses of 200 nm on Si substrates through

Table A.1 **NiFeCr resistivity.** Resistivity measurements of 200nm NiFe, NiFeCr, and CoGd films. Figures reported are the averages and standard deviations of two measurements per material.

Material	300K Resistivity ($\mu\Omega$-cm)	4K Resistivity ($\mu\Omega$-cm)
$Ni_{81}Fe_{19}$	22. ± 2	13. ± 2
$Ni_{73}Fe_{18}Cr_9$	81. ± 4	88. ± 1
$Co_{70}Gd_{30}$	337. ± 8	364. ± 7

mechanical masks of known geometries in a contact pattern optimized for resistivity measurement. The samples were then measured by four-terminal measurement at room temperature and 4.2K and the resulting I-V curves were fit to determine the resistance (slope). The samples were then imaged and measured using an optical microscope to determine length and width, and divided out to give resistivity. The results are shown in Table A.1.

A.2 Niobium Top Cap Study

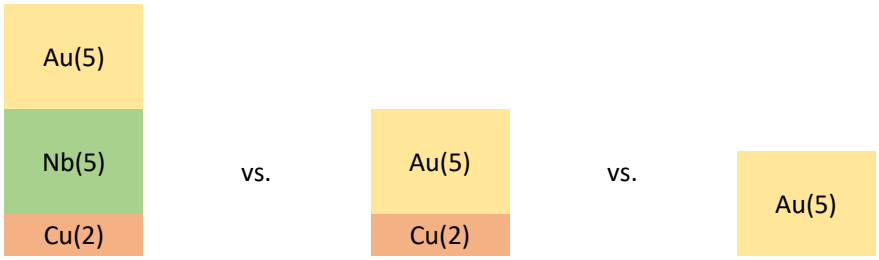

Figure A.3 **Nb top cap.** Graphic showing the three types of top caps investigated: Cu(2)/Nb(5)/Au(5), Cu(2)/Au(5), and Au(5).

For some time, sputtering of the bottom lead electrodes in the Birge group included a 20 nm cap of Nb atop the ferromagnetic interlayers. This was because, as the superconducting coherence length in Nb is about 14 nm, a layer of that thickness should be superconducting on its own. This would ensure that an S/F/S Josephson junction is complete upon deposition of the top leads. But, because Nb has such a high k-factor and ion mills very slowly, this means that milling through this Nb layer takes a very long time. Ion milling for such a long time heats up the sample and resist, which can make lift-off of the e-beam resist difficult. Therefore some time ago, it was decided to reduce this layer to 5 nm. As lift-off becomes even more difficult for the very small area junctions studied for the φ_0 junction project in Chapter 5, we investigated removing this superconducting layer entirely and either capping our junctions with Cu and Au or just Au, as shown in Figure A.3.

As part of this study, we also tested the bilayer e-beam resist scheme devised by Reza Loloee and Demet Korucu. In this elegant solution, they simply spun and baked our standard ma-N 2401 resist twice before writing with the SEM. While they had seen a dramatic improvement in lift-off success anecdotally, we decided to test this more rigorously and perform a full characterization to convince ourselves that other parameters of the junctions such as size and magnetization behavior were unaffected.

As the critical current transmission of Josephson junctions containing permalloy has been studied extensively in the Birge group, we fabricated a set of junctions nominally at the peak of the π state at a thickness of 2.2 nm. This meant that minor deviations from this thickness would

not meaningfully affect the critical current and cloud our results. The wealth of previous data also meant that overall parameters like $I_C R_N$ and switching field are known and easily compared. Junctions were fabricated in 500 nm by 1.25 μm ellipsoid sizes with either the single layer or bilayer e-beam resist and with each of the three top caps as described above.

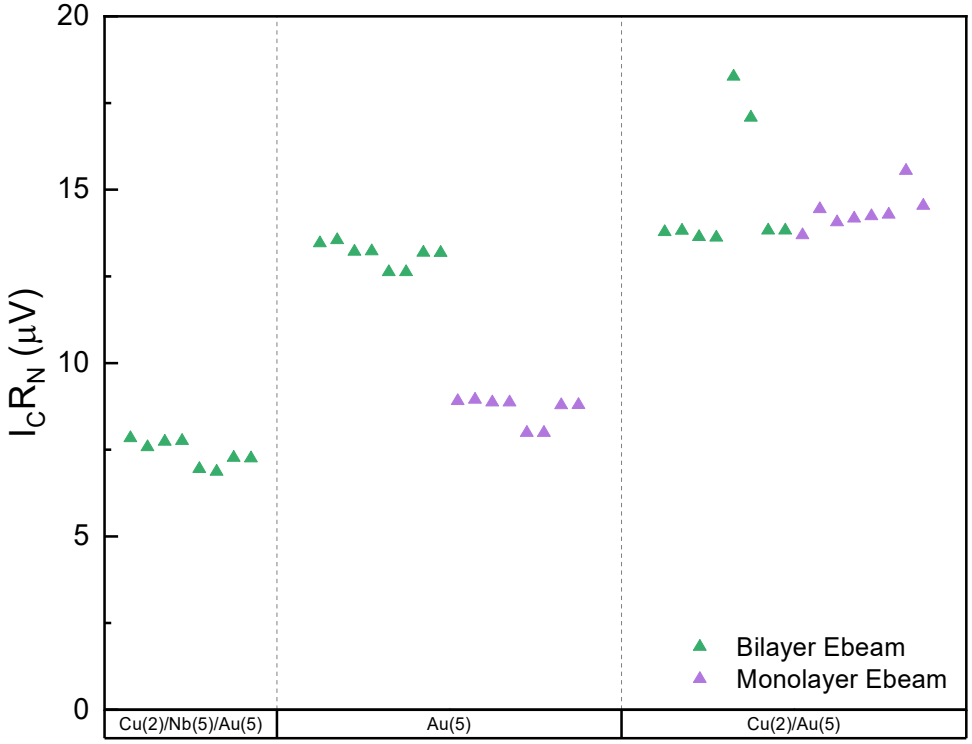

Figure A.4 **Top cap $I_C R_N$.** Plot of critical current vs. type for the junctions measured. Note that the monolayer Au alone samples had an anomaly in bottom lead deposition that explains their higher resistance. Some of the other characteristics should be unaffected by this anomaly, so the data are included here.

The main data are shown in Figure A.4. There was a significant *reduction* of the resistance and an even more significant *increase* in critical current from removing the Nb layer. The result is an $I_C R_N$ product that is increased by a factor of nearly two, as shown in Figure A.4. This is likely because the non-superconducting Nb(5) layer acts as an insulating barrier, increasing the resistance and decreasing the critical current.

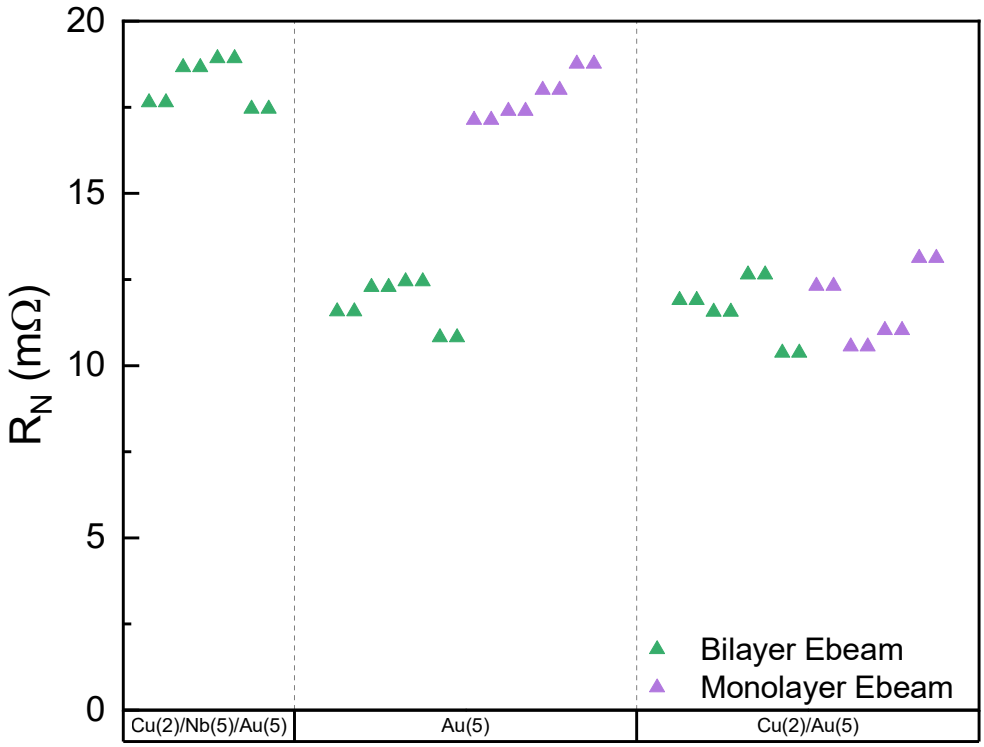

Figure A.5 **Top cap R_N.** Plot of normal state resistance vs. type for the junctions measured. Note again that the monolayer Au alone samples had an anomaly in bottom lead deposition that explains their higher resistance.

Figure A.5 shows the normal state resistance of the junctions measured, again with the monolayer Au(5) samples having a known anomaly during deposition of the bottom leads causing an erroneously higher resistance. The overall trend, however, clearly shows that samples without the Nb(5) top cap have a considerably lower normal state resistance, and there is consistency across monolayer and bilayer ebeam samples.

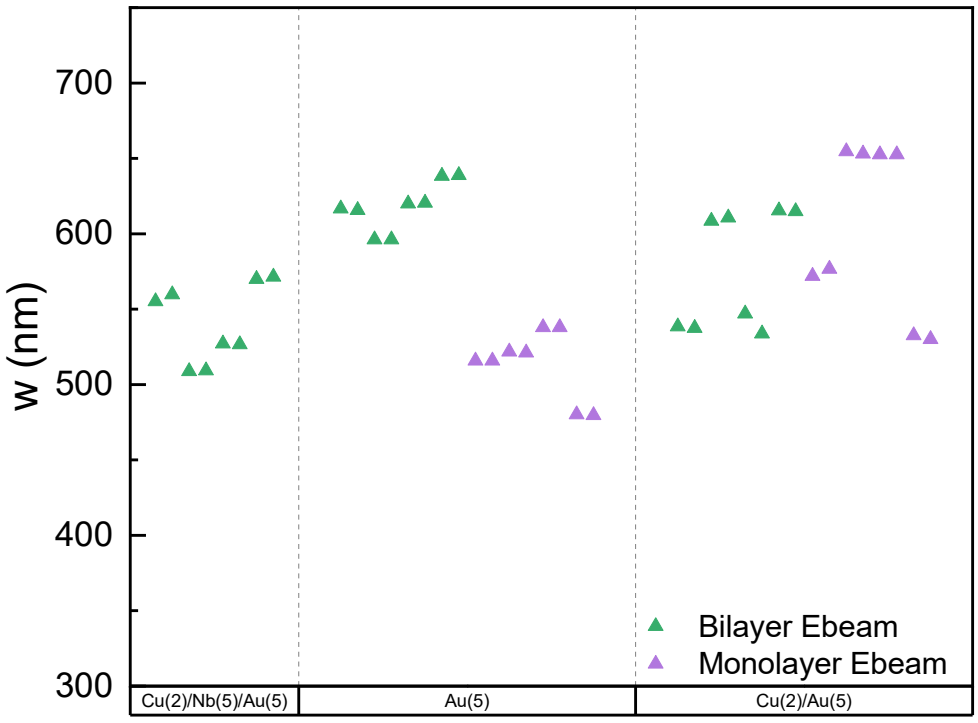

Figure A.6 **Top cap width.** Plot of junction width vs. type for the junctions measured. Junction width is determined by an Airy function fit to the magnetic field dependence of the critical current and extrapolation from known effective London penetration depth.

The data were further analyzed as discussed in Section 2.3.3 by fit to an Airy function, and extrapolation using the effective London penetration depth from previous studies [11] and the relation $\Phi = \mu_0 H w(2\lambda_{eff} + d_N + d_F) + \mu_0 M w d_F$. From this analysis, junction width, w, and field shift, H_{shift}, were determined and are shown in Figures A.6 and A.7 respectively. While there is some scatter in the width data, this is consistent with previous results and is likely due to variations in the SiO_x deposition thickness during the fabrication process as discussed in [11].

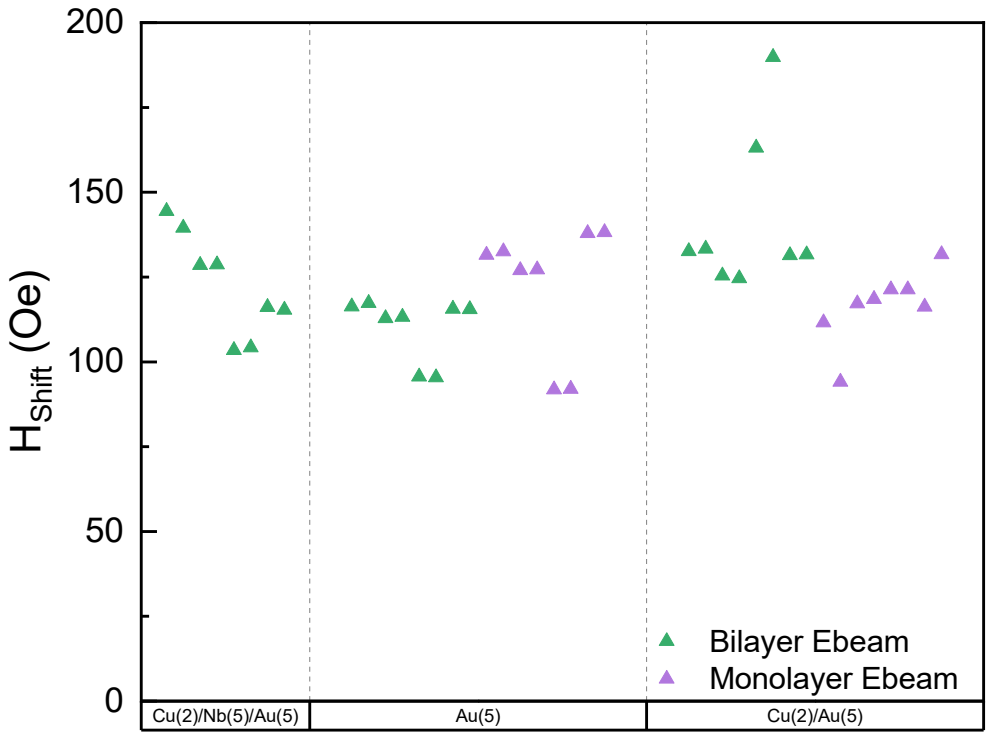

Figure A.7 **Top cap H_{shift}.** Plot of H_{shift} vs. type for the junctions measured. H_{shift} is determined by an Airy function fit to the magnetic field dependence of the critical current and extrapolation from known effective London penetration depth.

Our conclusions from all of this analysis is that the top cap of Nb is not necessary in future fabrication runs, and the evidence shows its inclusion has a deleterious effect on critical current transmission. Therefore, going forward, we plan to omit this layer. Further, the 'bi-layer' E-beam procedure devised by Reza Loloee and Demet Korucu was found to increase lift-off yield (to 100% from 93% in my testing) with no discernible negative impact on critical current, magnetic behavior, junction width, or resistance.

A.3 Chiral Molecules Study

A project we embarked upon with collaborators at Hebrew University of Jerusalem (HUJI) was motivated by the goal of inducing spin-triplet superconductivity, as discussed in Section 2.3.8, but using organic chiral molecules as the outer layers, instead of ferromagnets. This capability stems from spin-orbit coupling. The use of spin-orbit coupling to impart long-range triplet supercurrent has been suggested for some time [98, 99, 100, 101, 102, 103, 104, 105, 21]. The fact that organic chiral molecules can impart a spin selectivity has also been known for some time, in an effect called *chiral-induced spin selectivity (CISS)* [106, 107, 108, 109, 110]. Combining these effects, one would expect a mixing layer of an organic chiral molecule such as alanine, shown in Figure A.8 a), to also impart this long-range spin-triplet supercurrent.

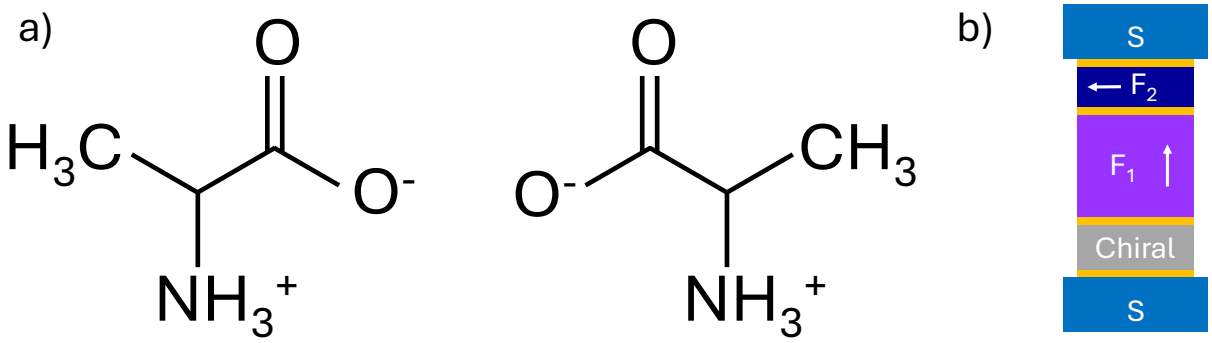

Figure A.8 **Chiral molecules.** a) L-Alanine (left) and D-Alanine (right) chiral molecules. b) Representation of proposed Josephson junction stack containing a layer of chiral molecules (Chiral), a PMA propogation layer (F_1), and a ferromagnetic spin-mixing layer (F_2) sandwiched between two superconducting layers (S).

The full triplet device would of course need to include a central ferromagnetic layer for propagation of the triplet supercurrent, as represented in Figure A.8 b). However, to begin to characterize the transmission of supercurrent through this chiral layer, samples were fabricated first as junctions containing only these chiral molecules and a thin protective Al_2O_3 layer as the barrier. Ultimately three batches of these samples were fabricated using different methods informed by the data, with the following results.

A.3.1 Batch I

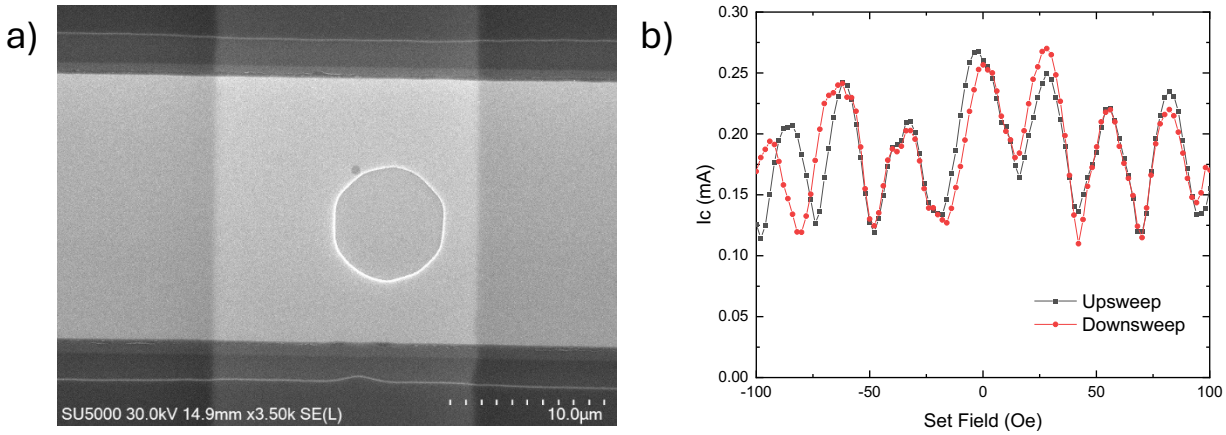

Figure A.9 **Batch I data.** a) SEM image of 2556-2B Pillar 6 after measurement. b) Magnetic field dependence of the critical current of sample 2556-2B Pillar 6.

The first batch of samples was sputtered in October of 2021 (Run no. 2556) and was fabricated in the traditional manner described in Chapter 3 by junction patterning and ion milling after deposition of the chiral molecule layer. This involved patterning and deposition of the bottom lead electrodes via sputtering at MSU, then shipping to Israel for deposition of the chiral molecule layer by wet chemical process and atomic layer deposition (ALD) of the insulating Al_2O_3 barrier. Back at MSU, the junctions were patterned by image reversal photolithography in 6 and 12 μm diameter circular shapes, ion milled, protected with SiO_x, lifted-off and capped with top leads. Upon measurement, the critical current vs field (I_C vs B) plots displayed vertically shifted oscillation patterns suggesting underlying shorting. One junction (2B-6, shown in Figure A.9) that had initially shown something resembling a Fraunhofer pattern was remeasured out to a higher magnetic field and shows a SQUID-like oscillation pattern similar to the other samples, see Section A.3.4.3 for a more in-depth explanation of this effect and its implications. [Fabrication at MSU was carried out by Josh Willard and Swapna Sindhu Mishra and original measurement by Josh Willard. The remeasure and the preponderance of fabrication and measurement of batches II and III were performed by myself. Deposition at HUJI was carried out by Nir Sukenik with supervision from Oded Millo, Yossi Paltiel, and Shira Yochelis.]

A.3.2 Batch II

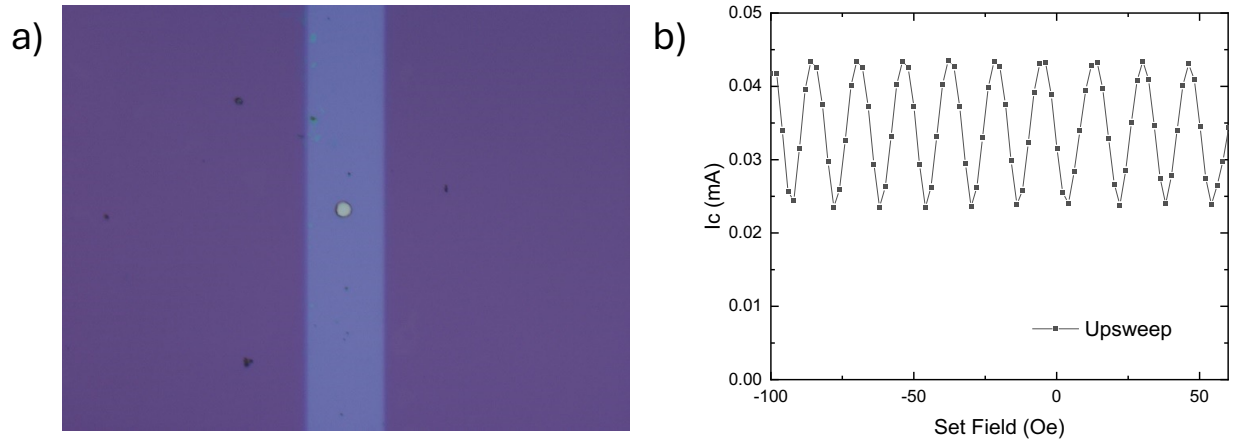

Figure A.10 **Batch II data.** a) Optical microscope image of sample 2564-2B Pillar 2, of diameter 6 Îijm, taken after return from Israel. b) Magnetic field dependence of critical current for sample 2564-2B Pillar 2, note that the period appears smaller than the 27 Oe that would correlate to shorts spaced by the junction width, indicating a *greater* distance between the shorts.

Given the indications of shorting, the second batch of samples (Run no. 2564), which was sputtered in April of 2022, was patterned before deposition of the chiral molecule layer. This was done by depositing SiO over the junction photolithography then performing lift-off of the resist, leaving holes in the SiO layer to define the pillars in 3 and 6 μm diameter sizes prior to shipping to Israel. During the fabrication for these samples we realized that two steps in the deposition of top leads on the first batch of samples might have damaged the chiral molecule layer- the oxygen plasma etch and the baking of the lift-off resist (LOR 5B) at 180 C. With the second batch, those steps were bypassed by using chlorobenzene with S1813-G2 resist to provide an undercut profile, or, on one sample (2B), using a mechanical mask instead of photolithography and foregoing the plasma etch altogether. Some of the top leads showed poor adhesion (possibly from skipping the plasma etch, see Section A.3.4), but many junctions were measurable. Again, there was evidence of shorting on most pillars (Figure A.10), but one small-area pillar (2B-1) showed a reasonable resistance but an unmeasurably small critical current. The conclusion from this data was that larger area junctions were needed to provide measurable supercurrent.

A.3.3 Batch III

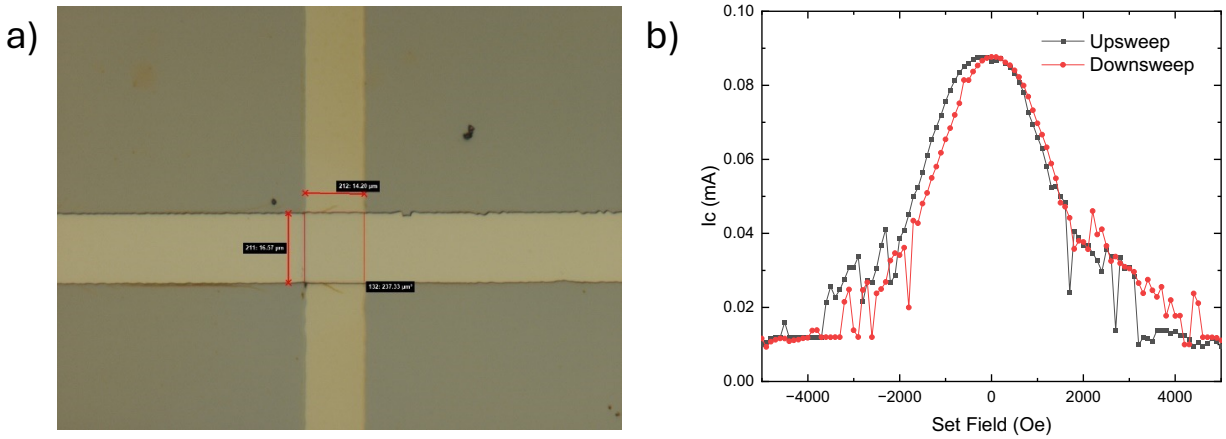

Figure A.11 **Batch III data.** a) Optical microscope image of sample 2570-2B Junction 4 taken after top lead deposition. b) Magnetic field dependence of critical current on sample 2570-2B Junction 4.

The third batch of samples, which was sputtered in June of 2022 (Run no. 2570) skipped the SiO layer entirely because we interpreted the previous Fraunhofer (SQUID-like) patterns as being due to shorts at the edges of the junctions, so this set relied only on the overlap of the top and bottom leads to define the Josephson junctions. To provide a wide range of areas in these samples, four different geometries using a combination of photolithography and mechanical masks were grown. This defined junction overlap areas ranging from 140 to nearly 80,000 μm^2. Upon measurement of these junctions, we found relatively large values of critical current that could only be suppressed by going to very high magnetic fields (Figure A.11). This likely indicates that the critical current is again dominated by shorts, but likely more than just 2 shorts, as there is no discernible SQUID oscillation pattern. This is not surprising given the much larger junction areas. A spreadsheet summarizing the data from all junctions is included below in Table A.2.

A.3.4 Anomalies

Several anomalies arose during the fabrication and measurement of these samples, which are enumerated below. Organic molecules are notoriously finicky to work with, so in that sense it is not surprising to encounter many issues.

A.3.4.1 'Crinkling' of the Top Leads

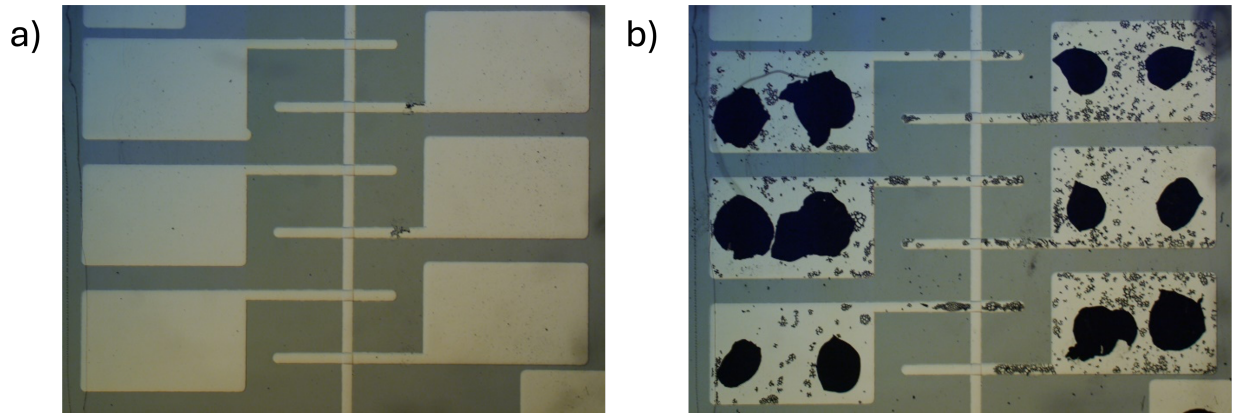

Figure A.12 **Crinkling.** a) Optical microscope image of sample 2570-6B taken after top lead deposition at 1.25x magnification showing only minor crinkling. b) Optical microscope image of sample 2570-6B taken after measurement at 4.2K. The large dark nearly-circular blobs are pressed Indium pads used for attaching wires to the sample.

Most samples from each batch showed a 'crinkling' effect of the top leads, as shown in Figures A.12 and A.13. To eliminate the possibility that this is a thermal effect from sputtering the top leads at -30 C, one sample (6B) was sputtered at room temperature and did not display this crinkling effect initially. However, after dipping in liquid He for measurement, this sample also displayed crinkling of the top leads.

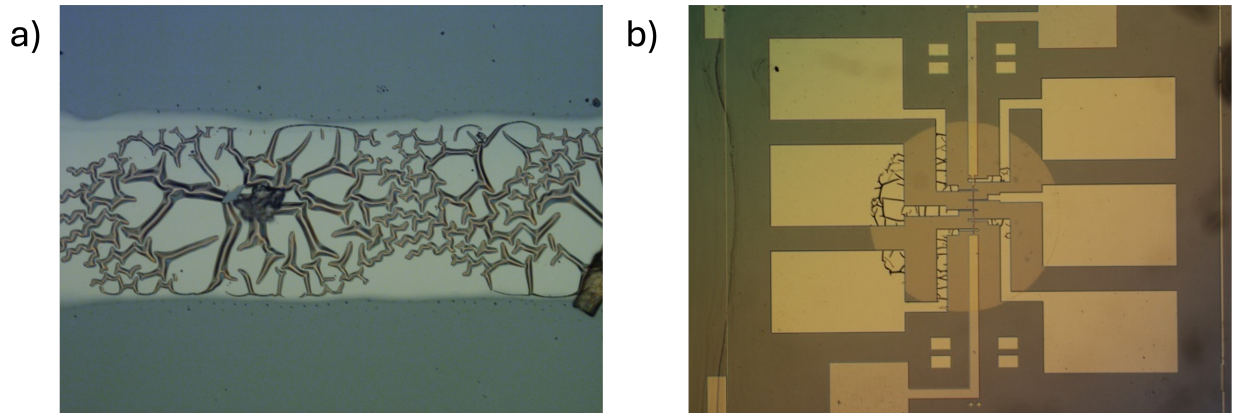

Figure A.13 **More crinkling.** a) Optical microscope image of sample 2570-6B at 20x magnification. b) Optical microscope image of sample 2570-1B taken after top lead deposition at 1.25x magnification. Note that the crinkling is confined to the circular area, which defines the Au deposition carried out at HUJI.

A.3.4.2 Contamination Within Chiral Molecule Layer

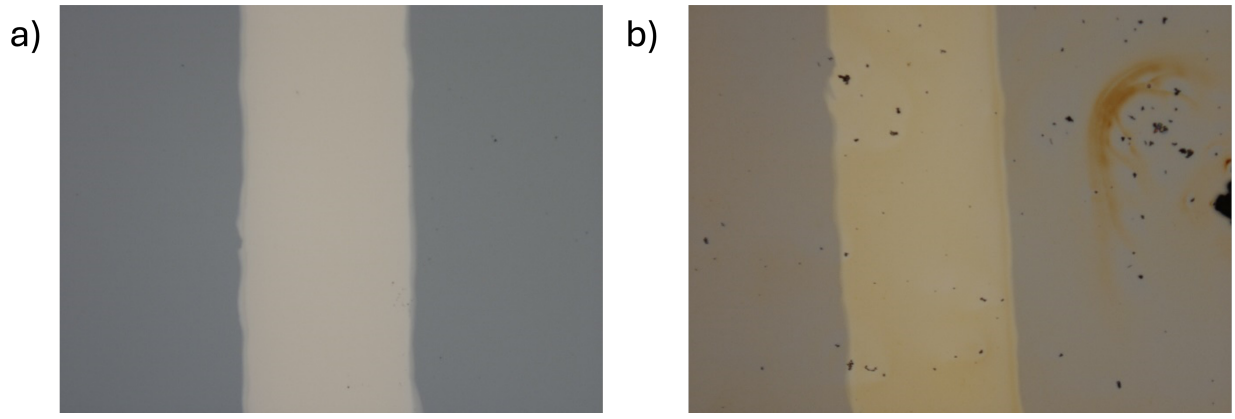

Figure A.14 **Contamination.** a) Optical image of sample 2570-7A (AlO only) taken after receiving from Israel at 20x magnification. b) Optical image of sample 2570-4B taken after receiving from Israel at 20x magnification.

The sample where only a layer of AlO was deposited (7A, Figure A.14 a) was visibly much cleaner than the other samples (for example 4B, Figure A.14 b). This contamination did not wash away in the acetone, IPA, DI water cleaning process, so our conclusion is that it must be embedded in the chiral molecule layer.

A.3.4.3 Deviations from a Standard Fraunhofer Pattern

As discussed in Section 2.3.3, if the supercurrent density is uniform, then plotting the magnetic field dependence of a rectangular Josephson junction's critical current produces an interference pattern analogous to that of single slit diffraction (with circular junctions producing visually similar Airy patterns). The oscillation period of the pattern is related to the London penetration depth of the superconducting layers and the diameter of the junction and corresponds to the magnetic flux quantum by the following formula:

$$\Phi_0 = B_\omega d(2\lambda_L + t) \tag{A.1}$$

where Φ_0 is the magnetic flux quantum, B_ω is the oscillation period, d is the diameter of the junction, λ_L is the effective London penetration depth, and t is the thickness of non-superconducting layers inside the junction. In our junctions, the quantity $2\lambda_L$ is close to 110 nm, and the thicknesses of the

various Au layers, chiral molecules and oxide add up to about 10 - 15 nm. This predicts a period of about 27 Gauss for a typical 6 μm diameter junction. (Recall that $B = H$ in cgs units.) When the critical current is dominated by two shorts, the pattern resembles that of a SQUID oscillation without decay with a period related by the same formula above, only now the d relates to the distance between the shorts, which is how we interpret the data in Figures A.9 and A.10.

A.3.5 Conclusions

There are two things to consider when interpreting the data from this project: the fabrication difficulties and the underlying science. It is important to parse those out in order to draw meaningful conclusions. On one hand, there were clearly many challenges with fabricating devices containing organic molecules, some of which are perhaps inherent [111], and some of which may be alleviated by alternate deposition methods [112]. If we focus on the data of the few samples fabricated as intended, with no apparent crinkling, shorting, or contamination, we find somewhat discouraging results. For example, our best JJ, pillar 2564-2B-1, showed a very high normal state resistance of 48 ohms, and a immeasurably small critical current density (less than 1.4 x 10^{-4} mA/μm^2). The data from the larger area junctions, which should exhibit measurable critical current, always showed evidence of shorting. In other words, we either find very small critical current or shorting through the chiral layer, with nothing in between. This indicates to us that the chiral organic molecule alanine may not be practical in Josephson junctions as a generator of triplet supercurrent.

Table A.2 **Chiral molecules JJ data.** Summary table of Josephson junctions measured for Chiral Molecules Project.

Pillar	Peak I_C (mA)	R_N (Ohm)	$I_C R_N$ (mV)	J_C (mA/μm^2)	Area (μm^2)
Run 2556 Sputtered 10/25/21 Measured March 2022					
2B-1	8	-	-	7.07E-02	113
2B-2	5.8	0.15	0.87	5.13E-02	113
2B-5	0.29	1.5	0.435	1.03E-02	28
2B-6	0.47	1.1	0.517	1.66E-02	28
Run 2564 Sputtered 4/13/22 Measured June 2022					
2B-0	0.31	1.25	0.3875	2.47E-02	1257
2B-5	0.244	1.2	0.2928	8.63E-03	28
2B-1	<0.001	48	-	1.41E-04	7
2B-2	0.045	5	0.225	1.59E-03	28
3A-6	1.3	1.7	2.21	4.60E-02	28
3A-5	>8	-	-	2.83E-01	28
3A-3	<2	-	-	2.83E-01	7
Run 2570 Sputtered 6/24/22 Measured August and September 2022					
1B-1	0.6	0.58	0.348	8.70E-04	690
1B-2	0.5	0.8	0.4	4.42E-04	1130
1B-3	(discont.)	-	-	-	255
1B-6	>5	-	-	1.53E-03	3270
2B-1	1	1.1	1.1	3.03E-04	3300
2B-2	0.175	1.9	0.3325	3.80E-04	460
2B-2R	0.07	6.7	0.469	1.52E-04	460
2B-3	0.01	63	0.63	6.99E-05	143
2B-4	0.09	4.8	0.432	3.75E-04	240
2B-5	0.006	34	0.204	5.31E-06	1130
2B-5R	0.003	120	0.36	2.65E-06	1130
2B-6	0.075	8.3	0.6225	1.14E-04	660
4B-2	19	0.02	0.38	7.60E-04	25000
4B-3	100	0.0014	0.14	4.00E-03	25000
4B-4	1.2	0.8	0.96	4.80E-05	25000
4B-4R	0.7	0.5	0.35	2.80E-05	25000
6B-1	16	0.019	0.304	4.00E-04	40000
6B-4	>100	-	-	2.50E-03	40000
6B-6	>100	5.30E-04	-	2.50E-03	40000
7A-3	>100	-	-	1.30E-03	77000
7A-4	>100	-	-	1.30E-03	77000
8A-1	>100	-	-	6.25E-03	16000
8A-2	>100	-	-	6.67E-03	15000
8A-3	80	-	-	4.71E-03	17000
8A-4	70	0.01	0.7	4.67E-03	15000
8A-5	>100	-	-	6.06E-03	16500
8A-6	75	-	-	4.69E-03	16000

APPENDIX B

LABORATORY NOTES

B.1 Triplet Supercurrent Calculation

Adapted from unpublished work by Norman O. Birge and William P. Pratt, Jr., this section provides a calculation for the propagation of supercurrent through a Josephson junction containing three ferromagnetic layers, with a central PMA layer. This system is represented in Figure B.1.

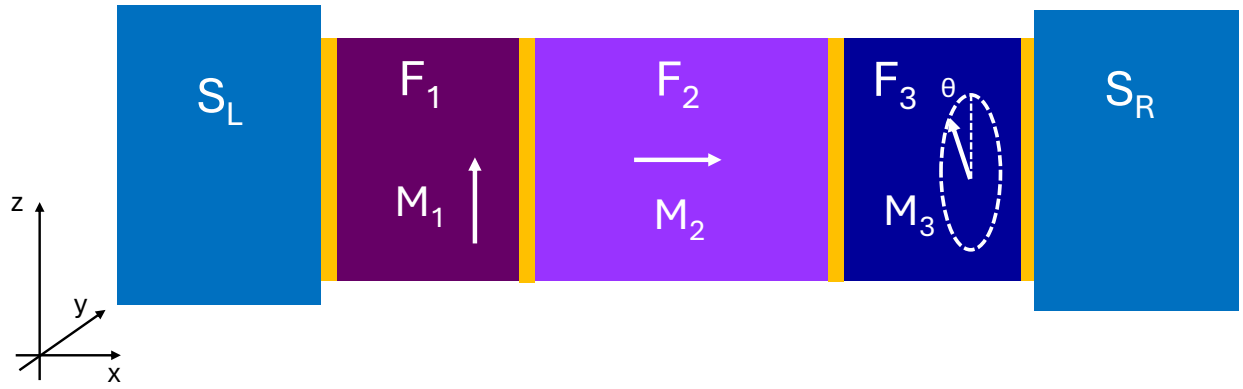

Figure B.1 **Triplet JJ.** Representation of a Josephson junction which propagates long-range spin-triplet supercurrent with three ferromagnetic layers– F_1, F_2, and F_3– whose magnetizations are indicated as M_1, M_2, and M_3, respectively.

Using the formalism developed by Matthias Eschrig [17], what is calculated here is the quantum-mechanical amplitude for a pair to propagate from S_L to S_R, remembering that the wave function must begin and end as a spin-singlet state. The Josephson coupling amplitude, which we call C_J, is proportional to this amplitude, and its starting formula is given by

$$C_J = \langle S_R | T_3 T_2 T_1 | S_L \rangle = \langle 0,0 | T_3 T_2 T_1 | 0,0 \rangle \tag{B.1}$$

where spin states are represented in the eigenstate basis of S^2 and S_z with **S** being the total spin of the pair S_z and its z-component. The ket $|0,0\rangle$ represents the singlet state and $|1,1\rangle$, $|1,0\rangle$, and $|1,-1\rangle$ represent the triplet states. The three T operators describe propagation of the state through the three ferromagnetic layers.

We know from Section 2.3.5 that as S_L propagates into F_1 acquire opposite center-of-mass momenta:

$$T_x|0,0\rangle = \frac{1}{\sqrt{2}}\left(|\uparrow\downarrow\rangle e^{iQx} - |\downarrow\uparrow\rangle e^{-iQx}\right) = |0,0\rangle\cos(Qx) - i|1,0\rangle_z \sin(Qx) \tag{B.2}$$

where $Q = k_F^{\uparrow} - k_F^{\downarrow}$ is the mismatch between majority and minority band Fermi wavevectors in F_1 and x is the center-of-mass coordinate of the electron pair. We also define the accumulated pair phase shifts in the F layers as $\varphi_1 = Q_1 d_{F1}$, $\varphi_2 = Q_2 d_{F2}$, and $\varphi_3 = Q_3 d_{F3}$ where the d_F's are the thicknesses of the F layers. We also add a prefactor s_1 to account for the decay of the short-range pair correlations in F_1. Putting this together, we write:

$$T_1|0,0\rangle = s_1\left(|0,0\rangle\cos(\varphi_1) - i|1,0\rangle_z \sin(\varphi_1)\right) \tag{B.3}$$

To calculate how this state propagates through F_2, we must write it in the eigenstate basis of S^2 and S_x, since the magnetization of F_2 points in the x direction. The singlet is rotationally invariant, so it does not change with the basis transformation. The result of the transformation is:

$$T_1|0,0\rangle = s_1\left[|0,0\rangle\cos(\varphi_1) - i\sin(\varphi_1)\frac{1}{\sqrt{2}}\left(|1,1\rangle_x - |1,-1\rangle_x\right)\right] \tag{B.4}$$

We next calculate how this state propagates through F_2, we already know that:

$$T_2|0,0\rangle = s_2\left(|0,0\rangle\cos(\varphi_2) - i|1,0\rangle_x \sin(\varphi_2)\right) \tag{B.5}$$

The triplet components $|1,1\rangle_x$ and $|1,-1\rangle_x$ do not acquire any phase shift, because they consist of two electrons in the same spin band, with nearly zero center-of-mass momentum[1]. Electrons propagating through a real ferromagnetic material are scattered at the interfaces and in the bulk. The degree of scattering can be very different for majority and minority spin bandsa. So we define transmission amplitudes $t_\uparrow$ and $t_\downarrow$ for the majority and minority electrons, respectively. Note that if we replace F_2 by a SAF, then we expect to have $t_\uparrow = t_\downarrow$ for the whole SAF, since electrons that are in the majority band in the first layer of the SAF will be in the minority band in the second layer, and vice versa. But for a single-layer F_2, we generally expect to find $t_\uparrow \neq t_\downarrow$. So we write:

$$T_2|1,1\rangle_x = t_\uparrow|1,1\rangle_x \text{ and } T_2|1,-1\rangle_x = t_\downarrow|1,-1\rangle_x \tag{B.6}$$

[1]We say 'nearly zero' because there is a very small momentum in the direction of the supercurrent.

Putting together B.4, B.5, and B.6 we get:

$$T_2T_1|0,0\rangle = s_1\left[s_2\cos(\varphi_1)\left(|0,0\rangle\cos(\varphi_2)+|1,0\rangle_x\sin(\varphi_2)\right)+i\sin(\varphi_1)\frac{1}{\sqrt{2}}\left(t_\uparrow|1,1\rangle_x - t_\downarrow|1,-1\rangle_x\right)\right] \tag{B.7}$$

To continue our calculation, it is convenient to express this result back in the z basis. The basis transformation takes the form:

$$\begin{aligned}
|1,1\rangle_x &= \frac{1}{2}\left(|1,1\rangle_z+\sqrt{2}|1,0\rangle_z+|1,-1\rangle_z\right)\\
|1,0\rangle_x &= \frac{1}{\sqrt{2}}\left(-|1,1\rangle_z+|1,-1\rangle_z\right)\\
|1,-1\rangle_x &= \frac{1}{2}\left(|1,1\rangle_z-\sqrt{2}|1,0\rangle_z+|1,-1\rangle_z\right)
\end{aligned} \tag{B.8}$$

Inserting those into B.7 gives:

$$\begin{aligned}
T_2T_1|0,0\rangle = {} & s_1s_2\cos(\varphi_1)\cos(\varphi_2)|0,0\rangle + s_1s_2\cos(\varphi_1)\sin(\varphi_2)\frac{1}{\sqrt{2}}(-|1,1\rangle_z+|1,-1\rangle_z)+\\
& s_1\frac{i\sin(\varphi_1)}{2}\left[(t_\uparrow-t_\downarrow)\frac{1}{\sqrt{2}}\left(|1,1\rangle_z+|1,-1\rangle_z\right)+(t_\uparrow+t_\downarrow)|1,0\rangle_z\right]
\end{aligned} \tag{B.9}$$

Rather than continue propagating this state to the right through F_3, it is easier to complete the calculation by propagating this state from S_L backward through F_3. The center-of-mass coordinate x will be negative in this case, which is equivalent to using the adjoint of the porpagation operator T_3. So we have:

$$T_3^+|S_R\rangle = T_3^+|0,0\rangle = s_3\left(|0,0\rangle\cos(\varphi_3)-i|1,0\rangle_\theta\sin(\varphi_3)\right) \tag{B.10}$$

Now transform that state back to the z basis:

$$\begin{aligned}
T_3^+|0,0\rangle &= s_3\left(|0,0\rangle\cos(\varphi_3)-i\sin(\varphi_3)\left(\frac{-i\sin(\theta)}{\sqrt{2}}|1,1\rangle_z+\cos(\theta)|1,0\rangle_z+\frac{-i\sin(\theta)}{\sqrt{2}}|1,-1\rangle_z\right)\right)\\
&= s_3\left(|0,0\rangle\cos(\varphi_3)-\sin(\varphi_3)\left(\frac{\sin(\theta)}{\sqrt{2}}\left(|1,1\rangle_z+|1,-1\rangle_z\right)+i\cos(\theta)|1,0\rangle_z\right)\right)
\end{aligned} \tag{B.11}$$

The adjoint of the previous expression is:

$$\langle 0,0|T_3 = s_3\left(\langle 0,0|\cos(\varphi_3)-\sin(\varphi_3)\left(\frac{\sin(\theta)}{\sqrt{2}}\left(\langle 1,1|_z+\langle 1,-1|_z\right)-i\cos(\theta)\langle 1,0|_z\right)\right) \tag{B.12}$$

Our final amplitude is just the scalar product of B.12 with B.9. Note that the second term in B.9 does not contribute because the combination of z states in that term is orthogonal to the combination in B.12.

$$C_J = s_1 s_2 s_3 \cos(\varphi_1)\cos(\varphi_2)\cos(\varphi_3) - \frac{1}{2} s_1 s_3 \sin(\varphi_1)\sin(\varphi_3)\left[(t_\uparrow + t_\downarrow)\cos(\theta) + i(t_\uparrow - t_\downarrow)\sin(\theta)\right] \tag{B.13}$$

Equation B.13 is our final result. If F_2 is thick, then we expect that $s_2 \ll t_\uparrow, t_\downarrow$, namely the Josephon coupling and supercurrent are entirely due to the long-range spin-triplet components in F_2. Furthermore, if $t_\uparrow \ll t_\downarrow$, then

$$C_J \approx -\frac{1}{2} s_1 s_3 \sin(\varphi_1)\sin(\varphi_3)\left[t_\uparrow \cos(\theta) + i t_\uparrow \sin(\theta)\right] = -\frac{1}{2} s_1 s_3 t_\uparrow \sin(\varphi_1)\sin(\varphi_3) e^{i\theta}. \tag{B.14}$$

This situation corresponds to a φ-junction with $\varphi = \theta + \pi$. For collinear alignments of the magnetizations M_1 and M_3, the P state produces a π-junction while the AP state produces a 0-junction. Intermediate angles produce intermediate phase couplings; the magnitude of the critical current does not vary with θ in this limit.

If F_2 consists of a SAF, however, the result is completely different. In that case we expect that $t_\uparrow = t_\downarrow$ so that the imaginary term in B.12 vanishes. In that case the Josephson coupling is purely real, meaning that one can only have a 0-junction or a π-junction. In that situation, $\theta = \pi/2$ produces zero coupling as the junction transitions from the π-state to the 0-state.

Finally, consider the case where F_2 is not very thick, which may be the case in Joseph Glick's study [8]. Then we cannot completely ignore the first term in B.13. That might explain why Joseph observes slightly different critical currents in the 0-state and the π-state.

B.2 Proper Documentation

As proper documentation is a critical part of scientific research, the following example is given to aid in the clearest, densest representation of information from a sputtering run. Figure B.2 shows the preferred format as it should be entered in the logbook. Things that should be clearly recorded include: run number, operator name(s), date, target materials and operating parameters, base pressure, cold pressure, sputtering pressure, exact structure by sample, deposition time, deposition temperature, deposition rate for each material (at every measurement), and ion mill settings (if used).

Sputtering Logbook Record Format

xxxx (Run #) [Student Name] xx/xx/xx (date)

A [Material Name] xxx/x.xx (V/I) 5 Cu xx W
B [Material Name] xxx/x.xx (V/I) 6 Ru xx W
C [Material Name] xxx/x.xx (V/I) 7 Au xx W
D [Material Name] xxx/x.xx (V/I) IM (settings below)

P_{base} = x.x x 10^{-8} Torr
P_{cool} = x.x x 10^{-8}
P_{sputt} = x.x x 10^{-3}

[Name of Study]

[Full stack #1 e.g. $[Nb(25)/Al(2.4)]_3/Nb(20)/Cu(2)/F_1(d_{F1})/Cu(2)/Au(10)$]

Deposition Rates (Å/s) *(record only when measured)*

Sample	d_{F1}(nm)	Time	Temp	[Mat A]	[Mat B]	[Mat C]	[Mat D]	Cu	Ru	Au	IM
1A	x.x	0:00	-xx (°C)	x.x	x.x	x.x	x.x	x.x	x.x	x.x	x.x
1B	x.x	0:00	-xx								
2A	x.x	0:00	-xx	x.x	x.x	x.x	x.x	x.x	x.x	x.x	x.x
2B	x.x	0:00	-xx								
3A	x.x	0:00	-xx								
3B	x.x	0:00	-xx								
4A	x.x	0:00	-xx	x.x	x.x	x.x	x.x	x.x	x.x	x.x	x.x
4B	x.x	0:00	-xx								

[Full stack #2 e.g. $[Nb(25)/Al(2.4)]_3/Nb(20)/Cu(2)/F_2(d_{F2})/Cu(2)/Au(10)$]

Deposition Rates (Å/s)

Sample	d_{F2}(nm)	Time	Temp	[Mat A]	[Mat B]	[Mat C]	[Mat D]	Cu	Ru	Au	IM
5A	x.x	0:00	-xx	x.x	x.x	x.x	x.x	x.x	x.x	x.x	x.x
5B	x.x	0:00	-xx								
6A	x.x	0:00	-xx	x.x	x.x	x.x	x.x	x.x	x.x	x.x	x.x
6B	x.x	0:00	-xx								
7A	x.x	0:00	-xx								
7B	x.x	0:00	-xx								
8A	x.x	0:00	-xx	x.x	x.x	x.x	x.x	x.x	x.x	x.x	x.x
8B	x.x	0:00	-xx								

NOTES:

[SPACE TO RECORD ANYTHING THAT GOES WRONG]

IM Settings: *(if used)*

I_B = x.x mA V_B = xxx V V_A = xx V V_D = xx V I_A = x.x mA
I_C = x.x A I_{NE} = x.x mA I_D x.xx A I_{NF} = x.x A

Figure B.2 **Sputtering logbook format.** Example of sputtering logbook documentation format for maximum information density and clarity.

B.3 Array Dicing Procedure

Here I provide a guide for dicing large EBL array samples for characterization in the SQUID magnetometer. This is necessary because the ion milling equipment requires larger samples than will fit in the magnetometer, so they must be diced after patterning and definition.

1. Spin S1813 photoresist on donor 3" wafer. Use approx. 1-1.5k RPM for ~30 seconds, and enough resist to cover the entire wafer. (You want the resist to be slightly goopy to adhere your sample.)

2. Quickly set array samples on 2 diagonal corners, in line such that the cut paths will not cross each other.

3. Drop resist over each sample, and spin very cautiously (~0.5k RPM) for 30 seconds, just enough to coat. (Too long or too fast here will send your sample flying!)

4. Bake resist and wafer as usual in oven at 95° C for 45 minutes.

5. Inspect wafer with optical microscope and place delicate scratches at the corners surrounding the array for location and orientation on the dicer.

6. Ensure dicer blade is non-ferrous. Warm up dicer. Select 'Josh half inch' dice program. Change cut depth to 13 mil (this nominally cuts through the sample and 2 mil into the wafer below). Load wafer into dicer.

7. Align (assuming Ebeam writing was aligned with edge of chip) using the auto align program, first to the right side of the bottom of the chip edge, then the right. Note that leftmost arrow buttons can be used to return to first alignment point as there is an automatic stage move purely in X. The last two alignment (on-wafer) steps can be skipped.

8. Note: The wafer is rotated 90° during the alignment process. It is now time to use the Y-offset feature to trick the dicer into doing our bidding.

9. (Assumes 4.5 mm square array.) First, find the edge of the array in the dicer image. Use the scratches to locate the area generally, then find the array itself. Note that the second leftmost arrow buttons control the focus. From the bottom edge of the array, zero the Y and move 0.875 mm down.

10. Under spindle controls, select 'Y-offset'. Perform a 'test cut', which will actually dice your sample. The software warns you that the test cut is within the wafer area, this is okay.

11. Once the cut is complete, don't forget to click 'Finish'. If the stage is moved vertically before you hit finish, this can misalign the cut target with the cut line; no bueno.

12. Next, move to the top cut target. The simplest way to do this is to re-zero the Y and move -6.25 mm up. Perform another test cut.

13. Rotate the stage by pressing 'A' near the second leftmost arrow buttons, then pressing the clockwise rotate button. Press 'A' again.

14. Find the array edge again, and repeat steps 10-12 to finish dicing the sample. Unload sample.

15. Repeat steps 7-14 for any other samples.

16. Gently rinse photoresist off of chips with acetone and place in sample holders. Note or create visual elements to discern easy and hard axis for ellipses and/or growth field.